Title

Engineering Electronic Properties of Novel Quantum Nanomaterials and Heterostructures

ISBN

9798189270765

Author

Cronin, Adam Daniel

Publication Date

2026-05-01

Peer reviewed|Thesis/dissertation

Engineering Electronic Properties of Novel Quantum Nanomaterials and Heterostructures

By

Adam D Cronin

A dissertation submitted in partial satisfaction of the

requirements for the degree of

Doctor of Philosophy

in

Chemistry

in the

Graduate Division

of the

University of California, Berkeley

Committee in charge:

Professor F. Fischer, Chair

Professor M. Crommie

Professor M. Zuerch

Spring 2026

Abstract

Engineering Electronic Properties of Novel Quantum Nanomaterials and Heterostructures

By Adam Cronin

Doctor of Philosophy in Chemistry

University of California, Berkeley

Professor Felix Fischer, Chair

The ability to control and predict the behavior of electrons in materials is highly sought after for the innovation of new technologies. Emergent localized electronic states and correlated phenomena in designer nanomaterials could provide an intriguing platform for the development of novel qubit architectures. Recent advancements have marked a new era in the engineering and design of such phases in nanomaterials through a variety of synthesis and fabrication techniques. Characterization methods such as scanning tunneling microscopy (STM) enable the precise structural visualization and local probing of electronic states. Using chemistry-based design concepts and materials fabrication and processing methods, this interdisciplinary research aims to isolate previously inaccessible structures and confirm their predicted electronic structure and behavior.

Herein I will present several strategies for the fabrication and isolation of novel nanomaterials and heterostructures and discuss the STM characterization of the resulting materials. Chapter 1 will detail the atomically precise synthesis of carbon nanomaterials from carefully designed chemical precursors. The vast repertoire of synthetic methods enables the design of materials with intriguing properties such as magnetic ground states or topological electronic states. Chapter 2 will focus on deposition and transfer techniques which allow the isolation of solution-synthesized polymeric precursors for carbon nanomaterials, as well as top-down synthesized nanomaterials such as phosphorene nanoribbons (PNRs). Finally, in Chapter 3 I will discuss a new strategy for the fabrication of Van der Waals heterostructures that could imbue new properties in 2D materials using molecular thin films to induce periodic strain or local magnetic moments. The realization of these relatively unexplored systems could break new ground in material design and technology development and further deepen our understanding of electrons in solids.

Contents

Engineering Electronic Properties of Novel Quantum Nanomaterials and Heterostructures 3

Introduction – Quantum Materials 1

0.1 Graphene 1

0.2 Graphene Nanoribbons 2

0.3 GNR Fabrication Methods 3

0.4 On-surface synthesis of atomically precise nanomaterials 4

0.5 Solution polymerization, polymer transfer and characterization 5

0.6 Heterostructures 6

0.7 Scanning Tunneling Microscopy 6

0.8 Tunneling theory 8

0.9 STM Imaging 9

0.10 Scanning tunneling spectroscopy (STS) 10

0.11 Common STS signatures: Flat bands, inelastic tunneling, quasiparticle gaps, and the Kondo effect 11

Chapter 1 – Atomically precise synthesis of graphitic nanomaterials 14

1.1 Magnetism in graphene nanomaterials 14

1.2 Triangulene 15

1.3 The Kagome Lattice 16

1.4 Antiferromagnetic [4]-triangulene covalent organic framework (COF) 18

1.5 Zigzag edge magnetism GNRs 25

1.6 Pinwheel and cove-type 6-N-ZGNR growth attempts 27

1.7 Topology in GNRs 31

1.8 9/7/9 Double quantum dot (DQD) 35

1.9 7/5/7 GNR heterojunction growth attempts 38

1.10 Outlook 38

Chapter 2 – Deposition and transfer techniques for polymers and other nanomaterials 39

2.1 MAD transfer 39

2.2 Length controlled polymerization of 9-AGNR precursors 40

2.3 MAD transfer of 9-AGNR polymer precursors 43

2.4 Solvent aerosol deposition 45

2.5 Phosphorene nanoribbons 47
2.6 Outlook 51
Chapter 3 – Novel Van der Waals heterostructures leveraging molecular templating 52
3.1 Molecular thin films 54
3.1.1 TOTA 54
3.1.2 Phthalocyanines 59
3.2 Properties of TMDs 64
3.3 TMD heterostructures and exfoliation procedures 65
3.4 In-vacuum transfer of monolayer TMDs 68
3.5 Heterostructure fabrication attempts 71
3.6 Outlook 74
References 75
Supporting Figures 84

Introduction – Quantum Materials

The deterministic control of exotic electronic states emerging from low-dimensional materials represents a scientific grand challenge. Rather than relying on scarce materials with intrinsic bulk properties, rational synthetic design gives rise to custom tailored electronic band structures in otherwise ordinary materials. The realization of this disruptive technology could incite new era of low-power high-frequency information processing as well as deepen our understanding of and ability to control electrons in solids

0.1 Graphene

Graphene is a two-dimensional (2D) atomically thin layered material composed of a honeycomb lattice of carbon atoms (Figure 0.1A) with an extended pi-electron network.[1,2] First isolated over twenty years ago via the "scotch-tape" method,[3] it has since been extensively studied and demonstrated to host charge carriers which act as massless Dirac fermions.[4] The band structure of graphene, shown in Figure 0.1B, contains two Van Hove singularities (VHS), corresponding to singular divergence of the density of states (DOS) at the M point. It also

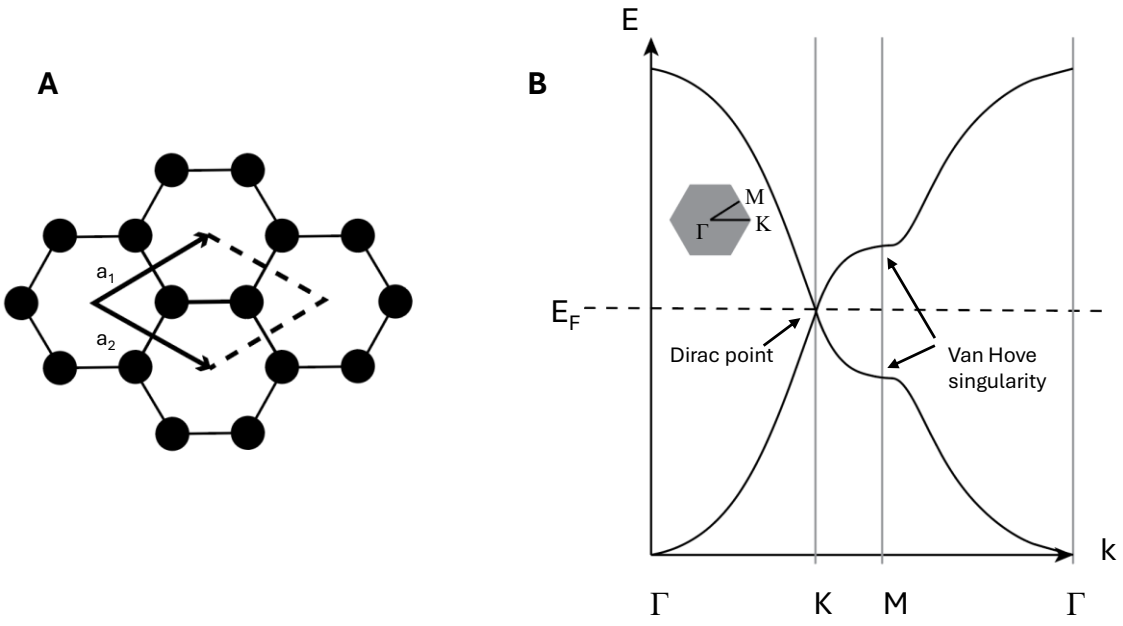

Figure 0.1 (A) Structural diagram of a small segment of graphene, black dots representing carbon atoms. The unit cell with unit vectors a_1 and a_2 is overlayed. **(B)** Sketch of the band structure of graphene, in which the valence and conduction bands meet at the Fermi energy where the density of states vanishes at $\vec{k}$ = K (Dirac point), and Van Hove singularities appear in each band at $\vec{k}$ = M. Inset shows the first Brillouin zone of the graphene lattice.

features conical conduction and valence bands which meet at the K and K' points (Dirac points) inducing semimetallic behavior.[2] Graphene has been demonstrated to have extremely high carrier mobility,[5,6] which is intriguing for integration into devices such as field effect transistors (FETs), but its semimetallic characteristics strictly limit its performance in the absence of environmental or chemical modifications.[7–10]

0.2 Graphene Nanoribbons

Graphene nanoribbons (GNRs) are quasi-one-dimensional strips of graphene which are defined by their width and edge structure and can exhibit a wide range of electronic properties. For example, in armchair GNRs (AGNRs), defined by the bulk edge (long edge) following the armchair direction of the graphene lattice, quantum confinement effects result in the emergence of a band gap,[11,12] while the GNRs retain the highly desirable transport properties of graphene. Within families of AGNRs categorized by their width in number of carbon atoms, the band gap decreases with increasing GNR width (Figure 0.2B)[12], suggesting certain wider AGNRs could host a smaller band gap than silicon, which would be highly advantageous for FET fabrication combined with high carrier mobility. Zigzag GNRs (ZGNRs) on the other hand host local edge magnetism resulting from the unique properties of parent graphene,[13–16] which will be discussed in Chapter 1. Other geometric classes of GNRs include chevron GNRs[17,18] and chiral GNRs,[19–21] while many proposed GNR structures do not fall into any of these categories. Carefully designing the specific edge structures[22–29] or incorporating heteroatom dopants[21,30–33] can give rise to a wide range of emergent properties. Accessing and characterizing these unique

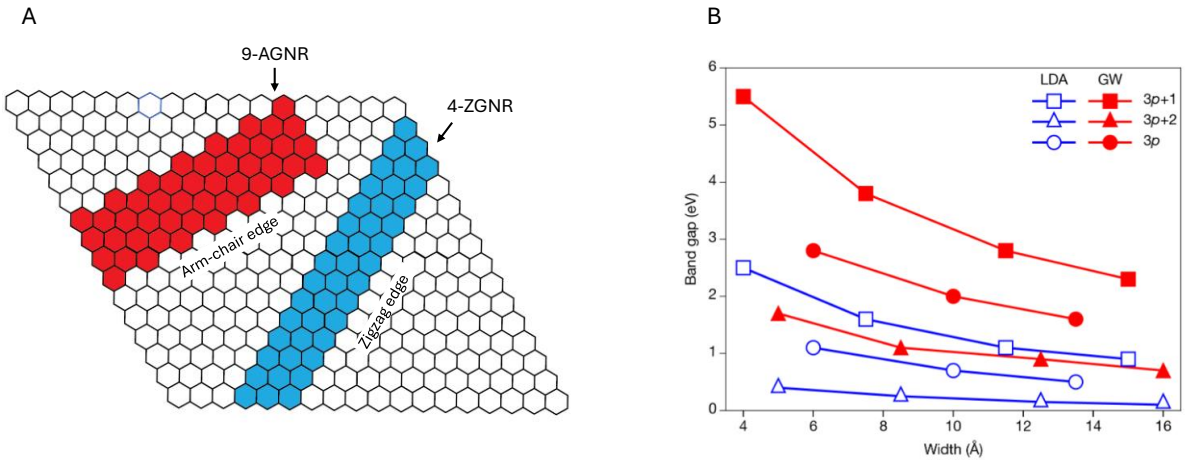

Figure 0.2 (A) GNR diagram, highlighting GNRs defined along the zigzag edge (ZGNRs) and armchair edge (AGNRs). GNRs are denoted by their width in number of carbon atoms. **(B)** Predicted band gaps for AGNRs of varying widths using both local density approximation (LDA) and the GW approximation. GNRs are grouped into three categories with width = 3*p*, 3*p*+1, and 3*p*+2 where *p* is an integer and the width represents the number of carbon atoms along the zigzag edge.

structures represents an important milestone in our understanding and control of electrons in nanomaterials.

0.3 GNR Fabrication Methods

Many top-down methods have been introduced for fabricating GNRs, such as nanoscale lithography of graphene[34] and chemical unzipping of carbon nanotubes (CNTs).[35] However, these techniques tend to result in GNRs with highly defective edge structures and little control over the electronic properties, yielding low-performance devices.

Bottom-up fabrication methods tend to produce less defective GNRs, however the control of the atomic structure varies depending on the method. For example, chemical vapor deposition (CVD) techniques have been widely studied,[36,37] including recent developments which showed that the growth orientation, GNR width, and edge structure could be partially controlled by constraining the CVD growth between stacked layers of hexagonal boron nitride (hBN).[38] This is achieved by carefully depositing metal nanoparticles along the hBN edge which act as a nucleation site for GNR growth, analogous to CNT growth techniques. The hBN constraint results in GNRs with the same edge type and low width dispersion contained in a device-compatible architecture which is highly advantageous for FET applications. However, while this technique allows some control over the resulting structure, only specific types of GNRs can be fabricated limiting the tunability of the electronic structure, and the widths cannot be perfectly controlled which inhibits device performance, although the resulting devices performed better than any previous experiments.[39] While the methods I will focus on herein provide much more control and optionality in the synthesis of GNRs, this transfer-free constrained CVD method is more likely to be the future of integrating GNRs into FETs and other devices due to the device compatibility of the growth substrate. Herein we will focus on band engineering in GNRs, 2D nanographenes, and layered heterostructures which could give rise to exotic quantum phenomena and deepen our understanding of electrons in solids.

0.4 On-surface synthesis of atomically precise nanomaterials

The bottom-up synthetic method on which I will focus relies on the rational design of molecular precursors and well-established surface chemistry to fabricate not just graphene nanoribbons, but a vast catalogue of zero, one, and two-dimensional carbon-based graphitic nanomaterials. The method provides total control of the overall atomic structure including edge topology and ability to dope the structure with heteroatoms. As a result, the electronic properties of the nanomaterials can be carefully tuned and the unique properties of the parent graphene, such as its bipartite lattice and exotic band structure, can be exploited to engineer metallicity, magnetism, topological phases, and other exotic quantum phenomena into its derivatives.

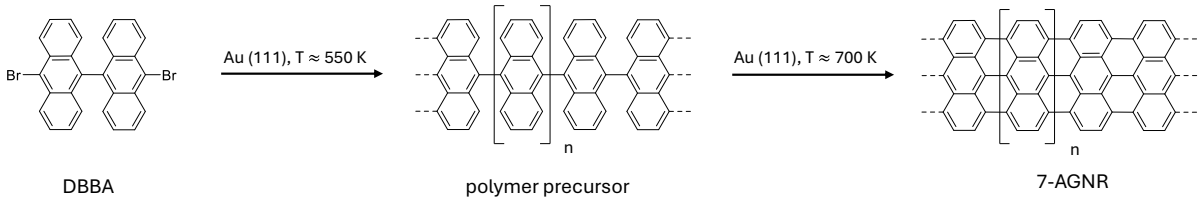

Figure 0.3 Schematic representation of the on-surface synthesis of 7-AGNRs from 10,10'-dibromo-9,9'-bianthracene (DBBA) via an Ullman-like coupling reaction. The bifunctional molecule is sublimed onto an Au(111) surface under UHV condition and subsequently annealed to induce dehalogenation followed by diffusion and polymerization. Further heating induces cyclodehydrogenation into the desired 7-AGNR.

In the first chapter, I will focus on graphitic nanomaterials synthesized from rationally designed molecular precursors using an on-surface Ullman-type coupling reaction.[40–42] A representative scheme for this synthetic method is shown in Figure 0.3 featuring the well-established synthesis of 7-AGNRs from 10,10'-dibromo-9,9'-bianthracene (DBBA).[40] This method relies on the catalytic surface Au(111) to stabilize reactive radicals on the precursors while allowing them to diffuse enough to polymerize with each other. These radicals are generated by the cleavage of a halogen atom (usually Br or I) which is installed on the molecule at the desired polymerization location. Careful surface annealing induces polymerization following halogen cleavage and radical formation. For quasi-1D systems, precursors with two halogens are used to form polymer chains on the surface, while for 2D systems, three or more halogen groups are installed to form carefully crosslinked polymers. Further surface annealing will then induce cyclodehydrogenation resulting in the fully graphitized nanomaterial which atomic structure defined exactly by the design of the molecular precursor.

0.5 Solution polymerization, polymer transfer and characterization

While surface-catalyzed fabrication method discussed above demonstrates remarkable control over the electronic and atomic structure of the resulting materials, there are some limitations. Notably, the molecular precursors must be symmetric to form homogeneous materials, which limits the variety of structures available. Additionally, the dispersity of the polymer chains for 1D systems and resulting lengths of the GNRs are impossible to control using this method. Solution-based polymerization techniques, however, exist which can overcome both drawbacks.[43,44] High molecular weight precursors and polymers generally cannot be sublimed onto the surface without degradation, requiring other deposition or transfer techniques to leverage these advantages of in-solution synthesis. Previous works have hinged on direct or dry contact transfer (DCT) to transfer isolated nanomaterials such as carbon nanotubes (CNTs)[45,46] and some molecules onto substrates for STM characterization. In this process, an applicator, generally made of fiberglass, is covered with the target nanomaterial or molecule in powdered form. The applicator is then brought into UHV where it is carefully brought in contact with a clean substrate which can then be subsequently annealed to facilitate diffusion of molecules and to remove substrate contamination. While this technique has been used successfully for some non-volatile molecular precursors, it has been unsuccessful for other molecules and especially for polymers, which tend to form aggregates and/or crosslink during cyclodehydrogenation yielding undesired structures. In the second chapter, I will detail two techniques which enable the deposition and surface characterization of polymers, high molecular weight compounds, and other bulk nanomaterials.

0.6 Heterostructures

Finally, in the third chapter I will discuss layered Van der Waals heterostructures, conventionally composed of stacked 2D nanomaterials which can induce hybridization of their electronic bands and exotic emergent phenomena.[47–50] I will introduce a new research direction which also leverages the variety of molecular properties accessible with synthetic chemistry to imbue desired properties in the resulting nanomaterials, but is not reliant on surface-assisted covalent bond formation, which tends to be low-yielding and defect-prone. Instead, thin films of molecules with desirable properties are grown using a self-assembly motif which results in large-scale monolayer molecular thin films. We propose heterostructures with template periodic strain in 2D materials interfaced with these molecular thin films, resulting in novel properties which could exotic electronic phenomena. I will discuss my attempts to fabricate these heterostructures and the molecular thin films I studied in the process, exfoliation and transfer procedures for layered 2D materials such as transition metal dichalcogenides (TMDs), as well as the implications for these types of heterostructures in the third chapter.

0.7 Scanning Tunneling Microscopy

Throughout this dissertation I will rely on scanning tunneling microscopy (STM) and spectroscopy (STS) to visualize and characterize novel nanomaterials and heterostructures. The technique relies on the establishment of a tunneling current between an atomically sharp metallic tip and flat metallic substrate (Figure 0.4A). This tunneling current is exponentially sensitive to the tip-sample distance which allows for high resolution imaging of surfaces with sub-nanometer resolution.[51] By changing the bias applied between the tip and the sample, electrons can either be tunneled from the tip into empty states in the sample or from occupied states in the sample to the tip (Figure 0.4B), allowing access to any energetic state within an energy window defined by the tip/sample bias. The convention is to refer to the bias of the sample with respect to the tip, V_s. The tip is mounted on high-precision piezoelectric motors which can reliably position the tip in three dimensions at the sub-Angstrom scale, allowing spatial mapping of the tunneling signal resulting in high-resolution STM images. The derivative of the tunneling current with respect to voltage (d*I*/d*V*) is also approximately proportional to the local density of states (LDOS) of the system. This enables both energetically (d*I*/d*V*) , differential conductance, or scanning tunneling spectroscopy (STS)) and spatially resolved (d*I*/d*V*, STS, or differential conductance mapping) characterization of the LDOS in 0-2D nanomaterials which provides important insight into their band structures.[51] The STM is held in an ultra-high vacuum (UHV) chamber and is thermally equilibrated with a cryostat held at 4.2 K using liquid helium, reducing signal noise and enabling quantitative interpretation of STS.

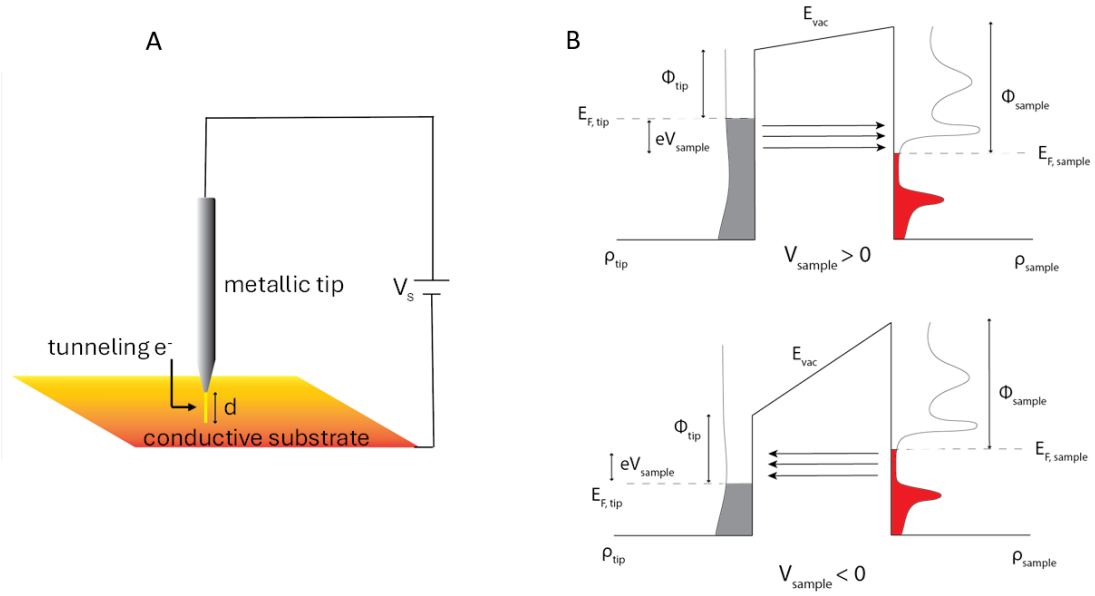

Figure 0.4 (A) Sketch of an STM set-up, where a tunneling current is established between a metallic tip and a conductive substrate by applying a bias voltage, which is conventionally referred to as the sample voltage, V_s. **(B)** Energy level diagram for a positive V_s (top) and negative V_s (bottom). Application of a bias voltage induces a chemical potential gradient between the tip and sample which allows tunneling electrons to travel from occupied states in the tip (sample) to unoccupied states in the sample (tip) for $V_s > 0$ ($V_s < 0$). ϕ_t and ϕ_s are the work functions for the tip and sample, respectively. ρ_t and ρ_s are representative density of states (DOS) for the tip and sample, respectively. E_{vac} is the vacuum energy and E_F is the Fermi energy.

0.8 Tunneling theory

In this section I will discuss the key principles which enable STM by relating the tunneling current to the LDOS of the sample using Bardeen's theory of tunneling[52] and the Tersoff-Hamman approximation.[53]

Bardeen applied Fermi's golden rule to tunneling between two systems, where electrons transition from an initial state in the tip to a final state in the sample. The rate for a particular transition is given by equation **0.1**, where $W_{i\to f}$ is the rate of transition from initial state ψ_i to final state ψ_f, H' is the Hamiltonian perturbed by the tunneling event, δ is the Dirac delta function which preserves elastic tunneling, and E_f and E_i are the energies of the final and initial state, respectively.

$$W_{i\to f} = \frac{2\pi}{\hbar}\left|\langle\psi_f|H'|\psi_i\rangle\right|^2\delta(E_f - E_i) \qquad \textbf{0.1}$$

The tunneling matrix element is defined as

$$M_{f,i} = \left|\langle\psi_f|H'|\psi_i\rangle\right| \qquad \textbf{0.2}$$

We will focus on the elastic tunneling regime, where the chemical potentials of the tip and sample align at E_F, allowing us to rewrite the rate of transition from a tip state to a sample state as

$$W_{t\to s} = \frac{2\pi}{\hbar}\left|M_{s,t}\right|^2\delta(E_F - E) \qquad \textbf{0.3}$$

To obtain the total tunneling rate of electrons from tip to sample we must integrate over all possible transitions from tip states to sample states. The number of available tip states is $\rho_t dE$ and the number of available sample states is $\rho_s dE$ where $\rho_t(\rho_s)$ is the density of states of the tip (sample). Assuming ρ_t is roughly constant, which is achieved by deliberate selection of the material for the tip, the rate of transitions from tip to sample states can be written as

$$W_{t\to s} = \frac{2\pi}{\hbar}\rho_t\int_{-\infty}^{\infty}\left|M_{s,t}\right|^2\delta(E_F - E)\rho_s dE \qquad \textbf{0.4}$$

This expression does not consider that an electron can only be tunneled from an occupied state into an unoccupied state, so it must be modified to reflect the probability of the initial (final) state being occupied (unoccupied). The probability that a state with energy *E* is occupied at temperature *T* is given by the Fermi-Dirac function:

$$f(E,\mu,T) = \frac{1}{e^{(E-\mu)/k_BT}+1} \qquad \textbf{0.5}$$

where μ is the chemical potential and k_B is the Boltzmann constant.

Weighting equation **0.4** by the probability of a tip (sample) state being occupied (unoccupied) gives

$$W_{t\to s} = \frac{2\pi}{\hbar}\rho_t \int_{-\infty}^{\infty} \left|M_{s,t}\right|^2 \delta(E_F - E)\big(1 - f(E)\big) f(E)\rho_s dE \quad \textbf{0.6}$$

For tunneling to occur, a bias V_s must be applied to the sample which shifts the occupied sample states away from the E_F by a quantity eV_s, which gives:

$$W_{t\to s} = \frac{2\pi}{\hbar}\rho_t \int_{-\infty}^{\infty} \left|M_{s,t}\right|^2 \delta(E - eV_s - E_F)\big(1 - f(E - eV_s)\big) f(E)\rho_s dE \quad \textbf{0.7}$$

The corresponding equation for electrons tunneling from the sample to the tip is:

$$W_{s\to t} = \frac{2\pi}{\hbar}\rho_t \int_{-\infty}^{\infty} \left|M_{s,t}\right|^2 \delta(E - eV_s - E_F)\big(1 - f(E)\big) f(E - eV_s)\rho_s dE \quad \textbf{0.8}$$

The net tunneling current is given by

$$I = -e(W_{t\to s} - W_{s\to t}) = \frac{2\pi e}{\hbar}\rho_t \int_{-\infty}^{\infty} \left|M_{s,t}\right|^2 \delta(E - eV_s - E_F)\big(f(E) - f(E - eV_s)\big)\rho_s dE \quad \textbf{0.9}$$

At temperatures approaching T = 0 K, the Fermi-Dirac distribution is a step function simplifying **0.9** to

$$I = \frac{2\pi e}{\hbar}\rho_t \int_0^{eV_s} \left|M_{s,t}\right|^2 \delta(E - eV_s - E_F)\rho_s dE \quad \textbf{0.10}$$

The Tersoff-Hamman approximation assumes a spherical s-orbital-like tip state with work function ϕ and tip-sample distance d, which gives

$$\left|M_{s,t}\right|^2 \propto e^{-2\kappa d}, \kappa = \sqrt{2m\phi}/\hbar \quad \textbf{0.11}$$

Finally, again assuming constant DOS in the tip and now having simplified the tunneling matrix elements to a constant **0.10** can be written as

$$I \propto e^{-2\kappa d} \int_0^{eV_s} \delta(E - eV_s - E_F)\rho_s(E_F + eV_s) dE \quad \textbf{0.12}$$

Finally, the derivative of the tunneling current with respect to sample voltage can be written as

$$\frac{dI}{dV_s} \propto \rho_s\big(E_f + eV_s\big)\delta(E - eV_s - E_F) \quad \textbf{0.13}$$

0.9 STM Imaging

The ability of STM to resolve nanoscopic features on surfaces hinges on equation **0.12**, which shows that the tunneling current decays exponentially with tip-sample distance d.[51] This means the signal is highly sensitive to small changes in the topography of the scanning substrate. Precise positioning of the STM probe is enabled by fine piezoelectric motors. Additionally, tunneling current between an atomically sharp tip (which can be approximately achieved) to a sample essentially occurs only at the atomic apex of the tip, which allows for spatial mapping of the tunneling current signal with Angstrom resolution. The tip-sample distance d is generally on the order of 1 nm for topographic imaging. There are two modes in which topographic imaging

of a substrate can be performed. The first and most common is constant-current mode, where a feedback loop is established between the *z*-piezo position and the tunneling current, which is fixed. As the *x*/*y* position of the tip evolves through a scan, the *z*-piezo position is constantly adjusted in reaction to instantaneous changes in the tunneling current, which keeps the tip-sample distance *d* the same at each point. The change in the *z*-piezo position to satisfy the constant current is recorded at each *x*,*y* position and an image is produced from the resulting data. The feedback loop prevents the tip from crashing into sample features taller than *d* and therefore is the ideal scanning method for most substrates and topographic image collection. The second technique, referred to as constant-height imaging, measures the change in current at each *x*,*y* position due to varying *d* with the feedback loop disabled. It is ideal only for atomically flat surfaces and smaller scales and is typically employed in bond resolved imaging (BRSTM) and d*I*/d*V* mapping (see Section 0.10).

BRSTM is a technique which can be used to verify the atomic structure in molecules and graphene nanomaterials.[54] The method relies on the functionalization of an STM probe with a single carbon monoxide (CO) molecule,[54–56] which can be easily adsorbed onto the substrate inside the cryostat by leaking CO into the UHV chamber at about 10^{-8} torr. The STM tip is then functionalized by applying small voltage pulses near a surface-adsorbed CO. When the CO terminated tip is brought into proximity with a material on the substrate, the frontier molecular orbitals of the CO begin to overlap with electrons in the material, which are localized in covalent bonds. When the CO orbitals directly overlap with high electron density covalent bonds, distinctively low signal/tunneling current is observed due to Pauli repulsion between tip and sample electrons as opposed to between non-covalently bound atoms (i.e. at the center of a 6-membered ring).[57,58] For graphene nanomaterials, this results in large bright imaging features associated with the 6-membered ring, surrounded by thin dark features representing atomic bonds, enabling atomically precise structural characterization. While this technique does not produce true atomically resolved images (hence "bond-resolved"), it is sufficient to confirm atomic structure in 2D and quasi-1D graphene nanomaterials and is much simpler than techniques like *q*-Plus atomic force microscopy.[59]

0.10 Scanning tunneling spectroscopy (STS)

We have shown from equation **0.13** that the derivative of the tunneling current with respect to applied sample bias, d*I*/dV_s, is proportional to the local density of states (LDOS) in the sample. Scanning tunneling spectroscopy (STS), also referred to as d*I*/d*V* or differential conductance spectroscopy, hinges on this principle to infer details about the electronic band structure. Simple numerical differentiation of an *I*(*V*) curve obtained by measuring the tunneling current at varying sample bias tends to yield noisy results which plague interpretation of the spectra. Instead, a lock-in technique is used to directly measure the derivative of the tunneling current with respect to applied voltage. A lock-in amplifier is used to modulate the sample bias with a small AC voltage V_M with frequency ω such that the tunneling current expression becomes

$$I = I(V_s + V_M cos\omega t) \qquad \textbf{0.14}$$

which can be written as a Taylor expansion:

$$I = \sum_{k=0}^{\infty} \frac{V_M^k}{k!} cos^k \omega t = I(V_s) + V_M \frac{dI(V_s)}{dV_s} cos\omega t + \frac{V_M^2}{2} \frac{d^2 I(V_s)}{dV_s^2} cos^2 \omega t + \cdots \quad \textbf{0.15}$$

Using trigonometric identities and ignoring higher order terms, **0.15** can be re-written as

$$I \approx I(V_s) + V_M cos\omega t \frac{dI(V_s)}{dV_s} + \frac{1}{4} V_M^2 cos2\omega t \frac{d^2 I(V_s)}{dV_s^2} + \cdots \quad \textbf{0.16}$$

From equation **0.16** it is apparent that the component of the tunneling current which oscillates at the modulation frequency ω, $V_M cos\omega t \frac{dI(V_s)}{dV_s}$, is proportional to the first derivative with respect to the sample bias. The lock-in amplifier then multiplies this output signal by a reference signal also oscillating at frequency ω, considering a possible phase shit, and subsequently time averages and feeds the result through a low-pass filter. The final output is the isolated component of the signal oscillating at frequency ω (proportional to d*I*/d*V*) with all other signals including noise removed due to orthogonality of sinusoidal functions. This can also be extended to higher order derivatives by using the nth multiple of ω for the reference signal frequency to analogously measure the nth derivative. This technique can be used in one of two modes for conventional STM. The first is d*I*/d*V* (STS) or differential conductance point spectroscopy, performed at a single spatial location while varying V_s. Peaks in STS spectra correspond to increased sample LDOS, revealing the energies and dispersiveness of electronic bands, and enabling experimental determination of semiconductor gaps. The second is d*I*/d*V* (STS) mapping or differential conductance mapping, performed at a fixed energy while imaging an area on the sample, measuring the derivative at every *x*/*y* location. STS mapping enables spatial visualization of the LDOS in the sample and generally exhibits distinct nodal patterns which are reminiscent of the distribution of electrons in the material associated with a particular band. It can also be used to verify if a peak in the point spectroscopy corresponds to increased sample LDOS or distinguish overlapping signals from different bands. STS point spectroscopy and mapping results are generally compared to DFT predicted band structures, DOS and LDOS projections to verify interpretation of the data as it relates to the electronic structure of the material.[51]

0.11 Common STS signatures: Flat bands, inelastic tunneling, quasiparticle gaps, and the Kondo effect

As previously mentioned, STS point spectroscopy can give insight into the dispersiveness of a band from the peak sharpness/breadth. The DOS, ρ_s, is inversely related to the first derivative of the band dispersion relation $E(k)$ with respect to the wavevector, k.[60] A flatter, less dispersive band corresponds to a sharp d*I*/d*V* signal while a dispersive band corresponds to a broad peak over a wider energy window. Flat bands are known to give rise to the ideal

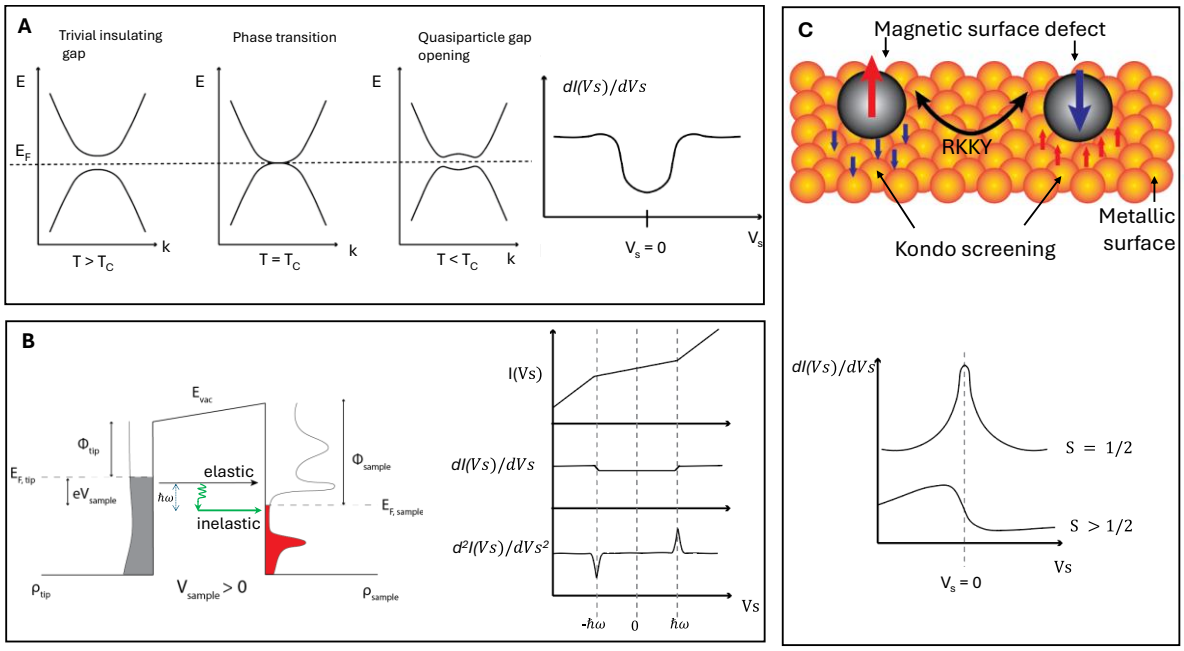

Figure 0.5 Origins and examples of common STS features. **(A)** Left, sketch of band diagrams for a representative system undergoing a phase transition where overlapping bands result in a quasiparticle gap opening. Right, sketch of representative *dI/dV* spectrum near zero-bias, featuring a distinctive dip in the signal associated with quasiparticle states. **(B)** Left, schematic of inelastic and elastic tunneling channels in STM. Right, sketches of representative I(V), d*I*/d*V*, and d^2*I*/dV^2 displaying signatures of inelastic tunneling at energy $\hbar\omega$. **(C)** Top, drawing of magnetic surface defects on a metallic surface, highlighting competing Kondo screening and RKKY driving antiferromagnetic interactions between defects in this example. Bottom, sketch of representative d*I*/d*V* curve for a Kondo screened magnetic defect. *S*=1/2 species exhibit sharp peak at zero bias and are fully screened. Higher spin species tend to exhibit more complex features at zero bias due to limited screening.

environments for strong electron correlations inducing exotic phases such as superconductivity,[49] and spin liquids.[61] This results from high effective mass of charge carriers which is inversely related to the band curvature, d^2E/dk^2.[60]

In systems with very high charge carrier mass under certain conditions, strong correlations (e.g. electron-electron, electron-hole, electron-phonon interactions) can drive exotic phase transitions (e.g. superconductivity, exciton formation) where quasiparticle condensation occurs leading to the emergence of a low-energy gap flanking the Fermi energy (V_s = 0 V), as shown in Figure 0.5A. For example, in conventional superconductors, Bardeen Cooper Schrieffer (BCS) condensation of bosonic Cooper pairs occurs at the Fermi energy, which induces the opening of a small superconducting gap in the electronic band structure.[62] This forbids tunneling of fermionic electrons into zero-bias states, resulting in a distinctive dip in the differential

conductance spectrum $V_s = 0$, where the gap width is on the order of a few meV, reflecting the energy required to remove an electron from the condensate (e.g. break a Cooper pair).

Inelastic tunneling is a phenomenon wherein a tunneling electron instantaneously excites a low-energy state such as a vibrational mode or spin state in the system (typically the sample) and loses a discrete amount of energy ΔE in the process. For $|V_s| > \Delta E/e$ corresponding to the energetic threshold for the excitation, a small increase in current is observed because electrons can tunnel through elastic and inelastic channels, as shown in Figure 0.5B. This manifests as symmetric shoulders in the STS point spectroscopy which flank $V_s = 0$, the inflection points of which occur at $V_s = \Delta E/e$. The second derivative d^2I/dV^2, which in turn displays sharp peaks at $V_s = \pm\Delta E/e$, is often measured to elucidate inelastic tunneling events. Signatures of inelastic tunneling due to spin excitations are important for determining magnetic ground states and investigating other magnetic behavior in materials.[51]

The Kondo effect is a phenomenon where the magnetic moment of a spin-bearing atom or molecule on a metallic substrate is screened by the substrate's conduction electrons below a critical temperature known as the Kondo temperature, T_{Kondo}.[63] For magnetic surface defects with S=1/2, the Kondo effect manifests as a sharp peak or Kondo resonance at zero-bias due to the local behavior of conduction electrons near the defect, reflecting complete screening of the magnetic moment. For higher spin systems, interactions between individual magnetic electrons in the defect compete with screening interactions from the conduction electrons, resulting in a less prominent Kondo resonance and more complex zero-bias spectroscopic features, as seen in Figure 0.5C.[64] The Kondo nature of a peak can be verified by variable temperature experiments wherein significant broadening of the feature with increasing temperature should be observed, followed by its complete disappearance above T_{Kondo}.[65] While a Kondo resonance indicates the presence of a local magnetic moment in a material, the interaction competes with desired magnetic exchange interactions that lead to ground-state magnetism, mediated through covalent bonds or the substrate itself. In covalently bound materials with adjacent spins, exchange interactions are often favorable enough to overcome Kondo screening, leading inelastic tunneling features in the STS with little or no Kondo resonance.[66,67] In weakly coupled systems such as self-assembled thin films of magnetic molecules, the magnetic moments can only couple and form magnetic ground states through scattering events in the conduction electrons, known as the Ruderman-Kittel-Kasuya-Yosida (RKKY) interaction, which can coexist with or be completely disabled by the Kondo interaction.[64] A Kondo lattice is a 2D array of periodic magnetic sites all forming a Kondo interaction with a metallic substrate. The local zero-modes contributions from each lattice site can be represented as a flat band at zero-bias, making hybridization of these states with electronic bands in other materials highly desirable.[50] This will be discussed further in Chapter 3.

Chapter 1 – Atomically precise synthesis of graphitic nanomaterials

1.1 Magnetism in graphene nanomaterials

Magnetism in bulk materials arises from the intrinsic magnetic moment, or spin, in electrons. In conventional magnetic solids, each atom in the lattice donates unpaired electron into a metallic band, and the neighboring magnetic moments couple through exchange interactions to minimize the overall energy, leading to long range magnetic order. Of particular interest are materials that exhibit ferromagnetism and have a strong spin alignment response to an external magnetic field, retaining long range alignment after the field is removed. Antiferromagnetic materials, on the other hand, contain unpaired electrons which align antiparallel to their nearest neighbors, resulting in a net zero magnetic moment of the material and no response to an external magnetic field. Many studies involving magnetism in solids have focused on materials containing *d* and *f* group metals where strong correlation between unpaired electron spin orbit coupling are present.[60]

Graphene is not intrinsically magnetic, nor does it contain *d* or *f* electrons, but magnetism in graphene derivatives can arise from its unique electronic and structural properties.[68] Notably, graphene has a bipartite lattice in which each unit cell contains two atoms which can be categorized into sublattices A and B, where atoms in A are only connected to atoms in B and vice versa. Lieb's theorem[69] applies the Hubbard model,[70] which uses tight-binding to consider exchange interactions between spins on neighboring lattice sites, to understand magnetism in a bipartite lattice. The Hubbard model Hamiltonian is given by equation 1.1 where *t* denotes the inter-lattice site hopping parameter, $c_{i\sigma}^{\dagger}(c_{j\sigma})$ is the creation (annihilation) operator for an electron with spin σ at site *i*(*j*), $\langle i, j \rangle$ restricts the sum to only nearest neighbor sites, and *U* is the repulsive interaction between electrons occupying the same site. [70]

$$H = -t \sum_{\langle i,j \rangle,\sigma} \left(c_{i\sigma}^{\dagger} c_{j\sigma} + c_{j\sigma}^{\dagger} c_{i\sigma} \right) + U \sum_i c_{i\uparrow}^{\dagger} c_{i\uparrow} c_{i\downarrow}^{\dagger} c_{i,\downarrow} \quad \textbf{1.1}$$

Liebs theorem shows that in a bipartite lattice with repulsive interactions between electrons ($U>0$), the total spin of the system is given by equation 1.2, where N_A and N_B are the number of sites in sublattices A and B, respectively.[68,69]

$$S = \frac{|N_A - N_B|}{2} \quad \textbf{1.2}$$

Ovchinnikov demonstrated that the same rule applies to graphene nanomaterials or alternate hydrocarbons using the Heisenberg model,[71] given by equation 1.3, assuming antiferromagnetic interactions between electrons ($J > 0$), where s_i denotes the spin operator at site *i*.

$$H = J \sum_{\langle i,j \rangle} s_i \cdot s_j \quad \textbf{1.3}$$

This simple yet powerful property provides a unique framework for designing atomically precise carbon nanomaterials with intrinsic magnetic properties. The ground state spin for an atomically precise nanographene or poly aromatic hydrocarbon (PAH) with an extended π-network can be easily determined using this rule.

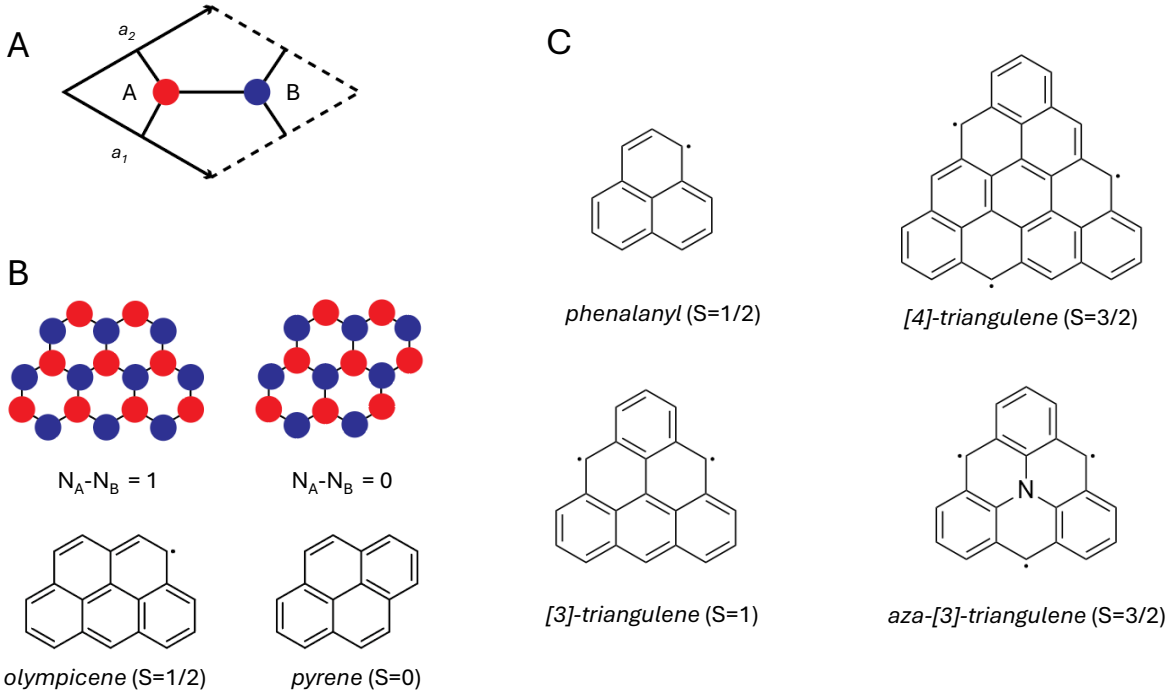

Figure 1.1 (A) Diagram of the unit cell in graphene, defined by unit vectors a_1 and a_2, featuring a bipartite lattice defined by alternating sublattices A and B, color-coded red and blue, respectively. **(B)** Schematic for determining sublattice imbalance in small molecules, olympicene and pyrene. **(C)** Structures of triangulene-type molecules with inherent sublattice

1.2 Triangulene

By applying Lieb and Ovchinnikov's rules to PAHs, several classes of molecules emerge as exciting candidates for synthesizing extended frameworks with inherent π-magnetism. For example, triangulenes are a group of PAHs with D_{3h} symmetry featuring zigzag edges along the molecule, as shown in Figure 1.1C. The are denoted by the number of carbons along the zig-zag edge, and exhibit sublattice imbalance and therefore ground state spin, which increases with the size of the molecule.

Triangulenes have been extensively studied on surface using STM. For example, phenalenyl has been characterized using STM on Au(111) and a distinct Kondo peak was observed associated with the singular unpaired electron in the system.[65] Additionally, both [3]- and [4]-triangulene have been characterized on Au(111) and their triplet and quartet magnetic ground states, respectively, have been confirmed. In both cases, signatures of singly occupied molecular orbitals were observed with spin-splitting.[66,72]

Phenalenyl[67] and [3]-triangulene[66] dimers have also been characterized using STM on Au(111) and signatures of spin excitations were observed in the STS spectra, indicating magnetic exchange interactions occurring between the two molecules through the π-network.

The demonstration of intermolecular coupling in covalently bound triangulene systems indicates that 1D and 2D networks composed of these molecules could exhibit unique magnetic properties driven by intrinsic π-magnetism at molecular lattice sites and exchange interactions. This behavior can be understood and predicted using an effective Heisenberg model.[71] However, synthesizing 2D frameworks of these molecules and characterizing their magnetic behavior remains a challenge.

1.3 The Kagome Lattice

An intriguing objective which could be accessed by surface synthesis techniques using properly functionalized triangluene precursors is the Kagome lattice, a 2D network which is composed of triangular sub-units (Figure 1.2A). The unit cell is analogous to graphene, defined by two triangular units instead of two carbon atoms, organized in a hexagonal bonding pattern. Kagome lattices are of particular interest in the solid-state physics community as they are predicted to host geometric frustration which preventing competing magnetic ground states from being realized, which can strongly correlated behavior and exotic ground states.[61] This is reflected in the band structure (Figure 1.2B), with the emergence of flat bands which correspond to highly localized electronic states. This type of electronic environment is a prerequisite for the formation of exotic behavior such as spin liquids[61,73] and topological insulators.[74]

Kagome-like structures composed of aza-[3]-triangulene, which has a spin of 3/2 and spin density localized at the center of each edge, have been synthesized on Au(111) and characterized with STM.[75] This framework was synthesized by connecting aza-[3]-triangulene at the edges rather than the corners using a cumulene linker. While the atomic lattice itself does not share the same arrangement or symmetry as the Kagome lattice, if the nodes of the wavefunction associated with the unpaired spins are treated as corners of the triangular superatom (Figure 1.2C), the system is analogous to a Kagome lattice and can be modeled

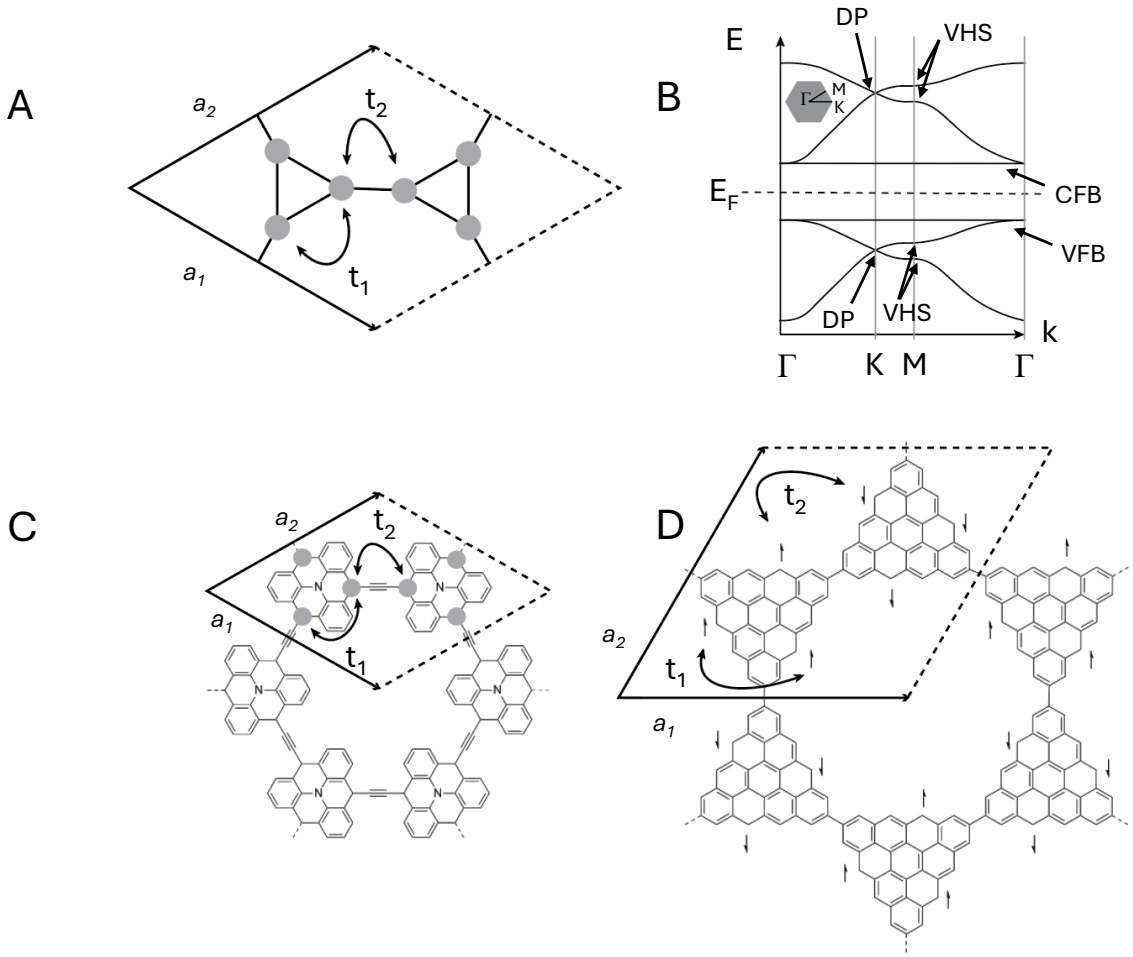

Figure 1.2 (A) Diagram of Kagome unit cell, featuring triangular sub-units joined at the corners. Unit cell vectors are labeled a_1 and a_2. Intra- and intercell hopping parameters are labeled t_1 and t_2, respectively. **(B)** Sketch of a typical band-structure for a Kagome lattice, closely resembling the predicted band structure for the Kagome lattice shown in **D**. Dirac points, Van Hove singularities, and valence/conduction flat bands are labeled DP, VHS, V/CFB, respectively. Inset sows the Kagome Brillouin zone with k-points Γ, K, and M labeled. **(C)** Structure of Kagome lattice formed by connecting aza-[3]-triangulene subunits with cumulene linkers at the molecular edges. Unit cell is drawn over the structure with gray circles representing the triangular Kagome subunits, and the intracell and intercell hopping amplitudes (t_1 and t_2) are labeled between edge sites where spin density localizes in the molecule. **(D)** Structure of Kagome latticed formed by connecting [4]-triangulene subunits at the corners. The structure is shown with ferromagnetic alignment between spins on the same molecule, with antiferromagnetic coupling between the magnetic moments on adjacent molecules. Unit cell is drawn over the structure with intracell and intercell hopping amplitudes (t_1 and t_2) labeled.

using this framework. Distinct spin excitation signatures were not observed in the system. Instead, the geometric phase frustration induced flat band formation which appear as sharp peaks in the STS spectra, consistent with DFT predictions.[75]

Another Kagome-like system composed of [4]-triangulene units connected at the corners (Figure 1.2D) has been widely studied in a theoretical context. The predictions range from second order topological properties[74] to excitonic ground states,[76] while another likely possibility is an antiferromagnetic ground state wherein complex spin excitations arising from the high spin molecular building block would be observed.[77] The strong interest from the theoretical community and variety of ground state predictions indicating exotic properties necessitate a strategy to fabricate the structure and characterize its ground state. I will detail our attempts to do so in the following section.

1.4 Antiferromagnetic [4]-triangulene covalent organic framework (COF)

In this section I will detail the synthesis and characterization of a Kagome-like [4]-triangulene COF ([4]TCOF). The design strategy focused on obtaining a molecular precursor to [4]-triangulene which can be efficiently converted with on-surface cyclodehydrogenation and is functionalized at the corners with a halogen allowing polymerization in the desired orientation. Initial efforts for the growth of [4]-TCOF were performed using precursor **1a**, shown in Figure 1.3, featuring brominated corners.

The precursor was evaporated onto a freshly cleaned Au(111) surface in UHV ($<10^{-9}$ torr base pressure) and the deposition parameters were optimized to produce the ideal density of sub-monolayer molecular thin films to facilitate polymerization. The substrate was then annealed at incremental temperatures until Br cleavage was induced, which occurred at approximately 250 °C. However, STM characterization of the resulting material revealed a highly disordered framework with only a small percentage of the molecules polymerization at the desired positions (see Figure S1). Additionally, most if not all molecules appeared to be fully cyclized, which indicates that debromination and cyclodehydrogenation occur simultaneously. We hypothesize that the temperature threshold for these two radical forming processes is very similar, causing polymerization at both corners and edges of the triangulene, wherever radicals form.

To circumvent this issue, we converted the bromines to iodines on the precursor resulting in precursor **1b**, shown in Figure 1.3. This was motivated by the significantly lower bond dissociation energy of the C–I bond as compared to the C–Br bond,[78] which should allow dehalogenation/polymerization to occur at a lower temperature.

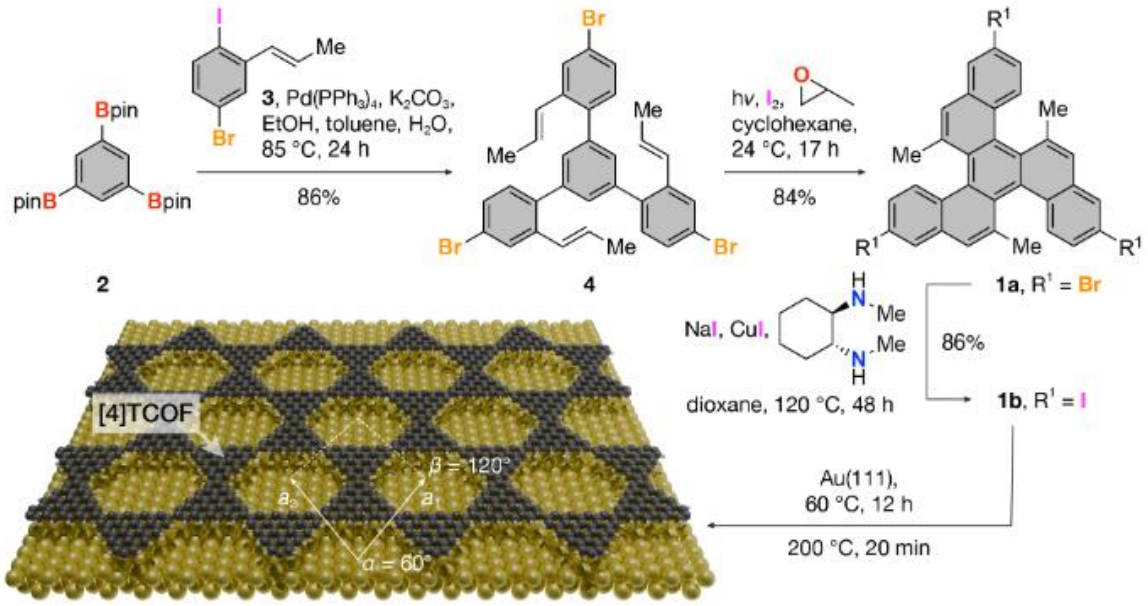

Figure 1.3 Synthetic route which was used to access precursors **1a** and **1b**, and schematic of on-surface growth of [4]TCOF Kagome lattice.

Precursor **1b** was evaporated onto Au(111) under similar conditions to precursor **1a**. Subsequently, the substrate was carefully annealed to just 60 °C to induce polymerization where it was held for 12 h, following which the temperature was slowly ramped to 250 °C to induce cyclodehydrogenation. As expected, the corner-to-corner bond formation fidelity in the resulting 2D nanostructure was much higher due to the low polymerization temperature, as shown in Figure 1.4. This surface chemistry technique is extremely defect prone and difficult to scale to 2D. As a result, the scale of pristine patches of [4]TCOF was very limited, and some undesired 5 and 7-membered rings as well as other defects occurred at relatively high density. However, some domains exhibited the desired Kagome lattice structure at large enough scale to investigate the magnetic behavior of the 2D system with STS.

The structure of [4]TCOF was first confirmed using BRSTM with a CO functionalized tip (Figure 1.4C), which revealed clear resolution of the desired intermolecular covalent bond formation and the distinct zig-zag edges of the [4]-triangulene. In addition to domains with the desired 6-member ring motif, areas with 5- and 7-member ring defects were observed, and a large number 1D [4]-triangulene chains ([4]T-chain) also formed on the surface. STS characterization of the [4]T-chain will be an important control experiment to provide insight into whether the extension of this system into two dimensions leads to emergent correlated phenomena.

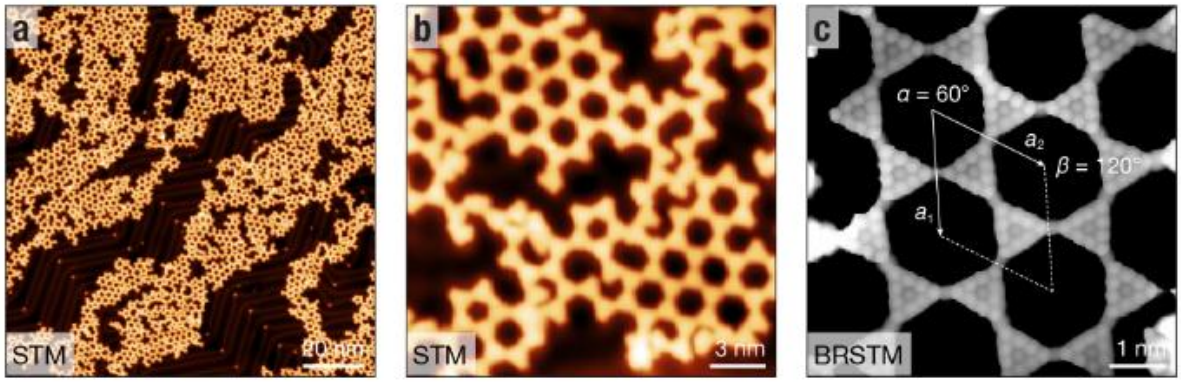

Figure 1.4 (A) Large-scale STM topographic image of [4]TCOF growth on Au(111). **(B)** STM topographic image featuring areas with pristine Kagome patches. **(C)** BRSTM image of pristine Kagome area confirming the desired structure, intermolecular linkages, and cyclodehydrogenation. All STM experiments were performed at T = 4.5 K.

STS was performed on the [4]T-chain at the molecular center, zigzag edge, and intermolecular junction, as shown in Figure 1.5. Spectra collected at the center of the [4]-triangulene units exhibited very few distinct features, appearing very similar to the Au(111) background. This aligns with expectations because the unpaired electrons should strongly influence the behavior near the Fermi energy and they localize along the zig-zag edges of the molecule. As expected, spectra collected at the zig-zag edges and intermolecular junctions of [4]T-chain revealed distinct peaks centered at V_s = –400 mV (peak 2), and 1200 mV (peak 1), associated with the valence (VB) and conduction band (CB), respectively. Based on the energy difference between the onset of these peaks, the experimental band gap is estimated to be $E_{exp} \approx$ 0.8 eV. Peaks associated with lower energy occupied states were also observed at V_s = –1200 mV and –1800mV. dI/dV mapping was also performed at energies associated with the peaks observed in the STS spectra, revealing the LDOS localizing at the intermolecular junctions for the CB and along the zig-zag edges for the VB.

Surprisingly, STS characterization of [4]TCOF yielded very similar results. Point spectra collected at the zig-zag edge and intermolecular junctions revealed distinct peaks at V_s = -500 mV (VB, peak 4) and 1100 mV (CB, peak 1), with a similar estimated gap of $E_{exp} \approx$ 0.8 eV, similar low energy occupied states at V_s = –1200 mV and –1900 mV, and dI/dV maps revealing LDOS localized at the junctions for the CB and the zig-zag edges for the VB.

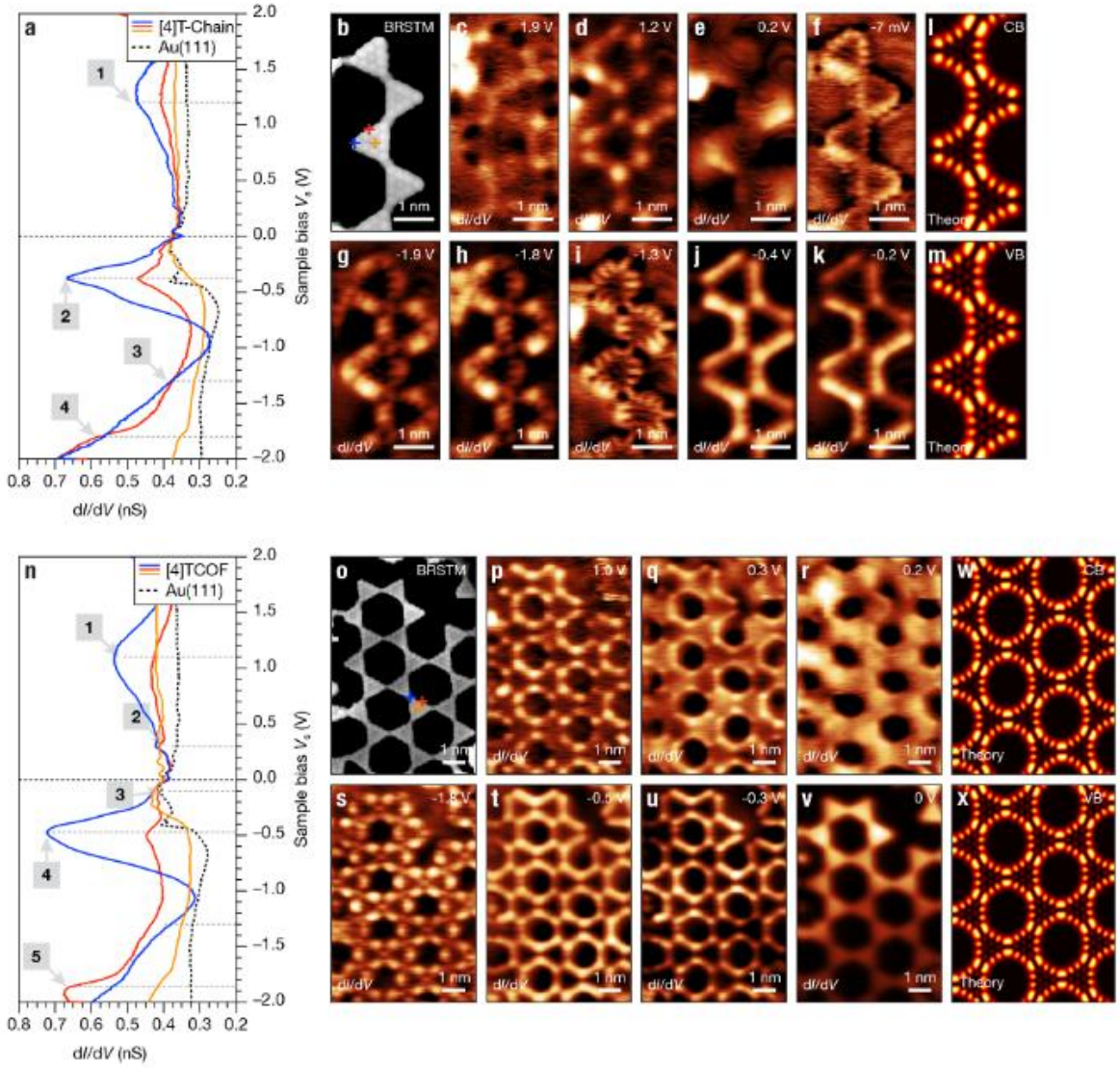

Figure 1.5 (A) d*I*/d*V* point spectra of [4]T-chain at the molecular positions marked in **B**. **(B)** Constant-current BRSTM image of [4]T-chain. The colored crosses correspond to curves shown in **A**. **(C-K)** Constant-current d*I*/d*V* maps at energies corresponding to peaks in **A**, with the bias voltage indicated on the image. **(L,M)** DFT LDOS projections for VB and CB of [4]T-chain. **(N)** d*I*/d*V* point spectra of [4]TCOF at the molecular positions marked in **O**. **(O)** Constant-current BRSTM image of [4]TCOF. The colored crosses correspond to curves shown in **N**. **(P-V))** Constant-current d*I*/d*V* maps at energies corresponding to peaks in **N**, with the bias voltage indicated in the image. **(W,X)** DFT LDOS projections for VB and CB of [4]TCOF. All STM experiments were performed at 4.5 K.

The striking similarities in the electronic characterization of [4]TCOF and [4]T-chain indicate that the overall behavior of the electrons is relatively unaffected by the dimensionality of the system. We infer that the [4]-triangulene subunits in both materials largely retain their intrinsic properties and weak magnetic exchange interactions between molecular units occur as a result.

The ground state of both [4]TCOF and [4]T-chain were modeled using first principles DFT calculations with the application of the generalized gradient approximation (GGA). Both a non-magnetic phase (NM) and an antiferromagnetic (AFM) phase were modeled to compare the ground state energies. In the AFM phase, the intra molecular alignment of unpaired electrons was assumed to be ferromagnetic (S = 3/2), while the intermolecular alignment, or the alignment of the total magnetic moment on adjacent [4]-triangulene subunits, was assumed to be antiparallel. Therefore, each unit cell contains a net zero magnetic moment. Calculations revealed energetic preference for the AFM phase with the energy of formation lowered by ΔE_f = –0.74 eV and –0.56 eV for [4]T-chain and [4]TCOF, respectively. The calculation for the NM phase predicted semimetallic behavior and a small band gap inconsistent with experimental results, while the calculation for the AFM phase predicts a very similar band gap o E_g = 0.72 eV and 0.8 eV for the [4]T-chain and [4]TCOF (Figure 1.6A), respectively. Moreover, the simulated LDOS maps for the VB and CB for the AFM phase (Figure 1.5L,M,W,X) closely resemble the nodal

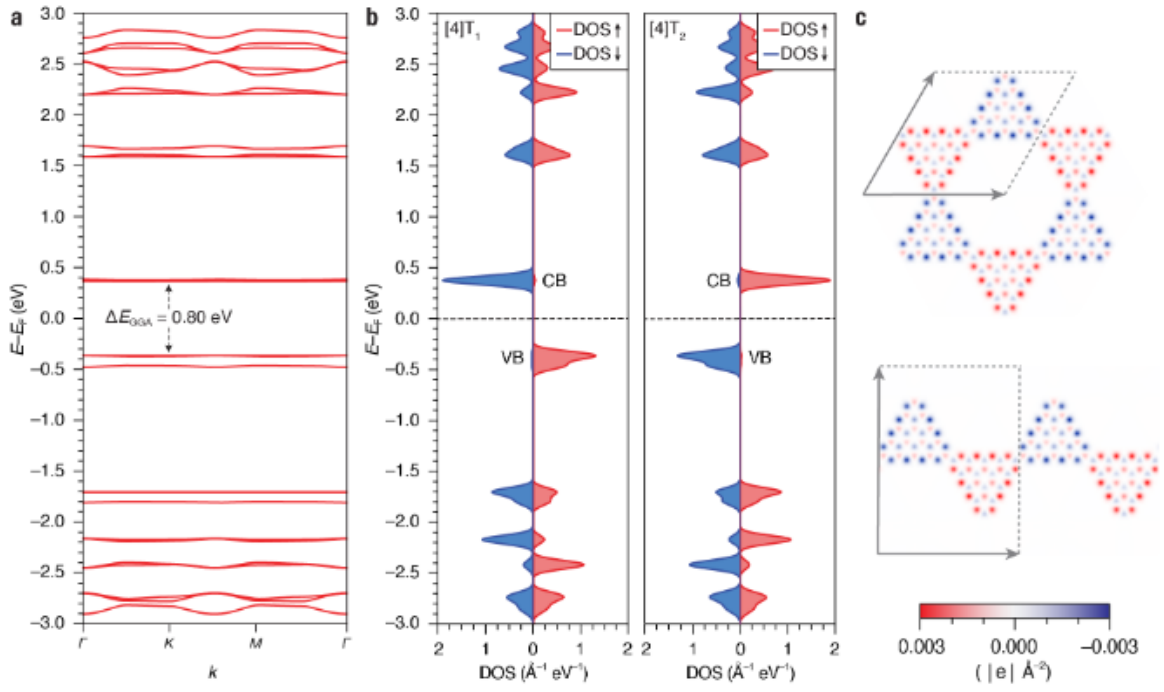

Figure 1.6 (A) DFT calculated band structure of [4]TCOF. **(B)** Calculated spin-polarized density of states (PDOS), broadened by 40 meV Gaussian. Red and blue represent opposite spins. **(C)** Spin density calculations for [4]TCOF (top) and [4]T-chain.

patterns observed in the d*I*/d*V* maps collected at the respective energies for the VB and CB band edge (Figure 1.5D,J,P,T), which is also reflected in spin density calculations for [4]TCOF (Figure 1.6C).

The close alignment between theoretical prediction for the AFM phase and experimental results, as well as the strong similarities between STS spectra for [4]T-chain and [4]TCOF, strongly suggest that antiferromagnetic behavior dominates the ground state of the system. However, there are some inconsistencies between experiment and prediction for [4]TCOF which likely arise from the limited scale at which it can be grown. Notably, while the estimated experimental band gap is similar to predictions, the AFM ordering and strong localization of electronic states near the Fermi energy should in very limited band dispersion and a very flat conduction and valence band, but the STS peaks associated with the VB and CB, especially the CB, are relatively broad, likely a result of the growth scale limitations.

To further investigate the magnetic behavior of [4]TCOF and [4]T-chain, low bias STS was performed to determine if inelastic tunneling events occur indicating spin excitations. During inelastic tunneling, electrons induce an excitation, such as a spin flip, in the sample, and through this transition lose a discrete amount of energy which manifests as a dip centered at Fermi energy (V_s = 0 V). This is a powerful tool for characterizing spin excitations and magnetic ground states of materials.

Low bias STS of [4]T-chain and [4]TCOF (Figure 1.7A,L) revealed distinct dips centered at V_s = 0 mV with energy scales very similar to previous reports of spin excitations in graphene nanomaterials. While the high spin (S = 3/2) of the molecular building blocks should lead to complex excitation behavior with multiple modes, only one distinct feature was observed in both spectra, likely due to experimental limitations such as thermal broadening. d*I*/d*V* maps collected at $V_s = \pm$ 50 mV, where the STS shoulders flanking the zero-bias dip appeared, revealed LDOS localization at the zig-zag edges (Figure 1.7C–K,N–T). This behavior was also not observed in isolated [4]-triangulene on Au(111).[72] These observations strongly indicate that the zero-bias feature is associated with spin excitations between covalently linked [4]-triangulene units in [4]TCOF and [4]T-chain and further confirms the AFM ground state.

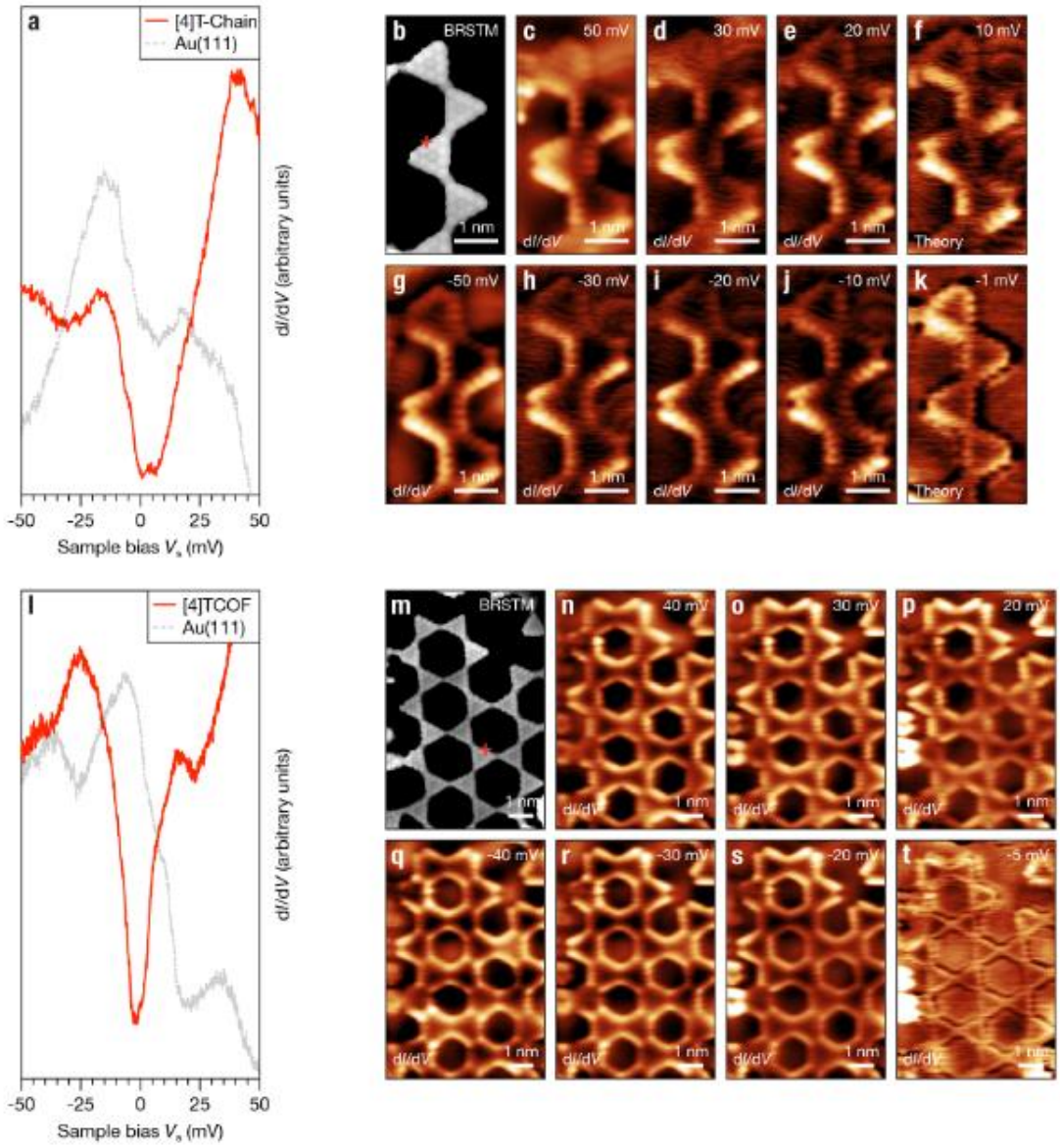

Figure 1.7 (A) Low-bias d*I*/d*V* point spectroscopy of [4]T-chain recorded at the position marked in **B**. **(B)** Constant-current BSTM image of [4]T-chain. **(C-K)** Constant-current d*I*/d*V* maps of [4]T-chain at various energies in the range of the zero-bias feature, indicated on the image. **(L)** Low-bias d*I*/d*V* point spectroscopy of [4]TCOF recorded at position marked in **M**. **(M)** Constant-current BRSTM image of [4]T-chain. **(N-T)** Constant-curreant d*I*/d*V* maps of [4]TCOF at various energies in the range of the zero-bias feature, indicated on the image.

1.5 Zigzag edge magnetism GNRs

Sublattice imbalance in nanographenes is not the only consequence of the bipartite lattice of graphene that induces magnetic behavior. The zig-zag edges of nanographenes have long been predicted to host spin-ordered electronic states. For example, zig-zag GNRs (ZGNRs) have been theorized and shown to exhibit ferromagnetic alignment between neighboring edge sites, and antiferromagnetic alignment across the edges.[11,13] The realization and control of these states could provide an exciting framework from carbon-based spintronic devices. The experimental confirmation of this magnetic edge behavior relies on probing the local environment of the edges using STM, since the overall magnetization of the material is zero due to antiferromagnetic coupling between the edges.

A major challenge for characterization of these edge states is the strong coupling between the zig-zag edges in ZGNRs with their growth substrate (Au(111)), convoluting the electronic and structural characterization of the material. Previous experiments have confirmed the zig-zag structure in 6-ZGNRs and probed their electronic behavior by dragging the GNRs onto islands of insulating KI deposited after GNR growth to decouple them from the substrate.[15]

Blackwell et al. used a different approach. Instead of synthesizing the all-carbon form of the 6-ZGNR, they used an acridine scaffold for the precursor design, which can grow into a 6-ZGNR with nitrogen atoms periodically doped along its edges (N-6-ZGNR), as shown in Figure 1.8A. Heteroatom doping is a versatile strategy in carbon nanomaterial synthesis and has important implications for band structure engineering and chemical functionalization of the materials. In this case the presence of nitrogen dopants is advantageous in two ways. First, it provides a local energy minimum for the surface orientation where the nitrogen atoms interact with the substrate and decouple the remaining carbons along the zig-zag edge, enabling local electronic characterization of the edge states (Figure 1.8C,D). This decoupling can be easily achieved with a voltage pulse from the STM tip. Second, the nitrogen lone pairs manifest as spin-split flat bands (Figure 1.8E,F) due to effective Zeeman splitting, which provide an internal probe for estimating the magnitude of the local exchange field resulting from zig-zag edge magnetism. They observed an experimental exchange splitting of $\Delta E \approx 100$ meV corresponding to an effective Zeeman field of $B_{eff} \approx 850$ T. These findings are a significant advancement in the realization and confirmation of zig-zag edge magnetism in GNRs and provide important implications for the design of novel materials where this behavior can be tuned to induce exotic electronic phenomena.[14]

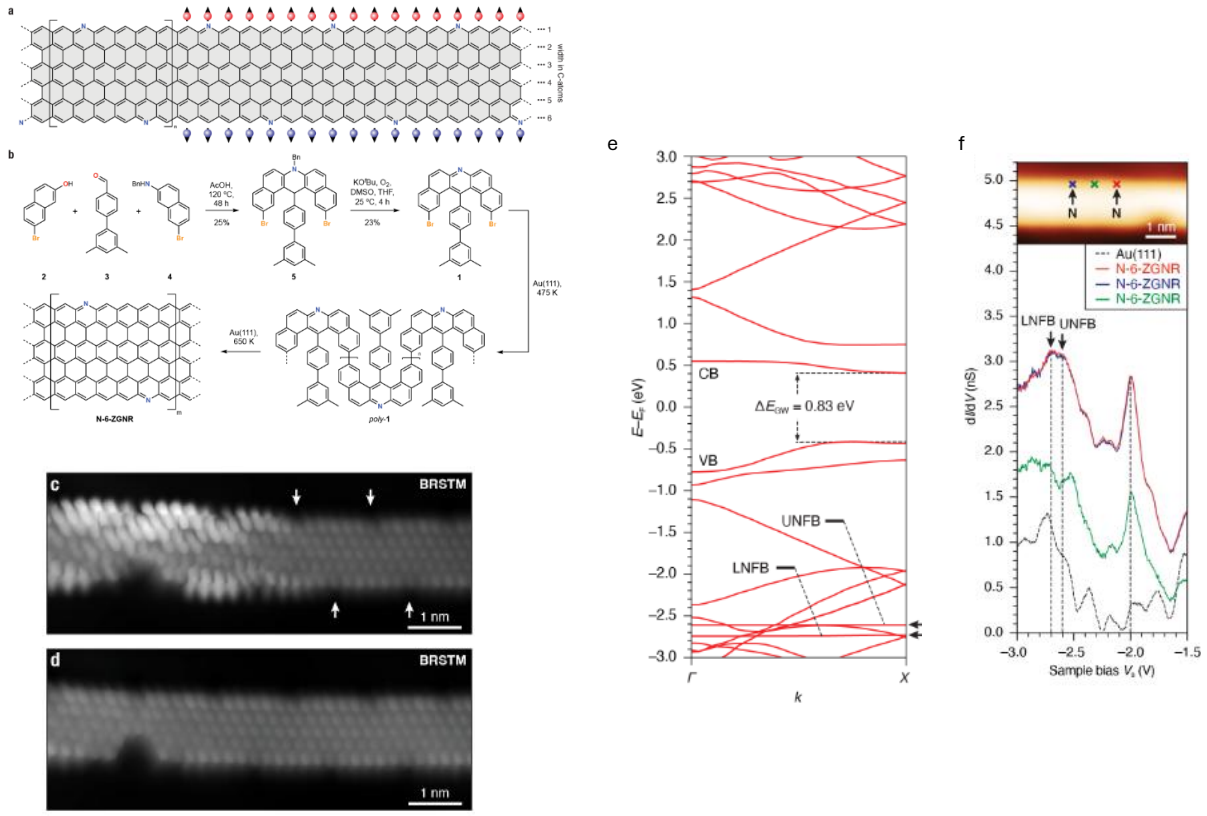

Figure 1.8 (A) Structure of N-6-ZGNRs with edge magnetism featuring ferromagnetic alignment along the edges and antiferromagnetic alignment across the edges. **(B)** Synthetic route for N-6-ZGNR precursor **1**, and schematic for on surface synthesis of N-6-ZGNRs. **(C)** BRSTM image of a partially decoupled N-G-ZGNR. On the left, strong hybridization between edge states and the Au(111) substrate results in distortion of the bond resolved image. On the right, the zig-zag edge is clearly visible, with dark spots labeled by arrows corresponding to the location of the nitrogen heteroatoms. **(D)** BRSTM image of a fully decoupled 6-N-ZGNR with a mouse-bite defect. **(E)** Predicted band structure for 6-N-ZGNR using DFT-GW. **(F)** *dI/dV* point spectra of 6-N-ZGNRs at areas marked in the inset. The peaks corresponding to the spin-split nitrogen dopant states are labeled upper and lower nitrogen flat band (UNFB and LNFB). Reproduced from Ref 14.

1.6 Pinwheel and cove-type 6-N-ZGNR growth attempts

The advancements in understanding and accessing zig-zag edge magnetism in GNRs have inspired numerous theoretical and experimental efforts to investigate the effects of periodic edge modification in these systems. ZGNR derivatives with specific edge alterations have been predicted to exhibit a wide range of exotic properties such as half-metallic[16] or topological behavior.[17] However, accessing the targeted structures remains a significant synthetic challenge, although a few ZGNR derivatives have been experimentally realized.[15,79] The acridine-based precursor scaffold used by Blackwell et al.[14] is significantly more accessible synthetically than the all-carbon analogue and therefore is an ideal platform from which to build precursors for edge-modified ZGNRs. In this section I will detail my attempts to grow GNRs imbued with periodically modified zig-zag edges from acridine-based precursors.

Our attempts to design ZGNR derivatives with edge alterations focused on periodically adding (removing) six-membered rings to (from) the zig-zag edge. The strategy was to replace the di-methylphenyl group on the established precursor (Figure 1.8B) with a pyrene (isopropyl group),

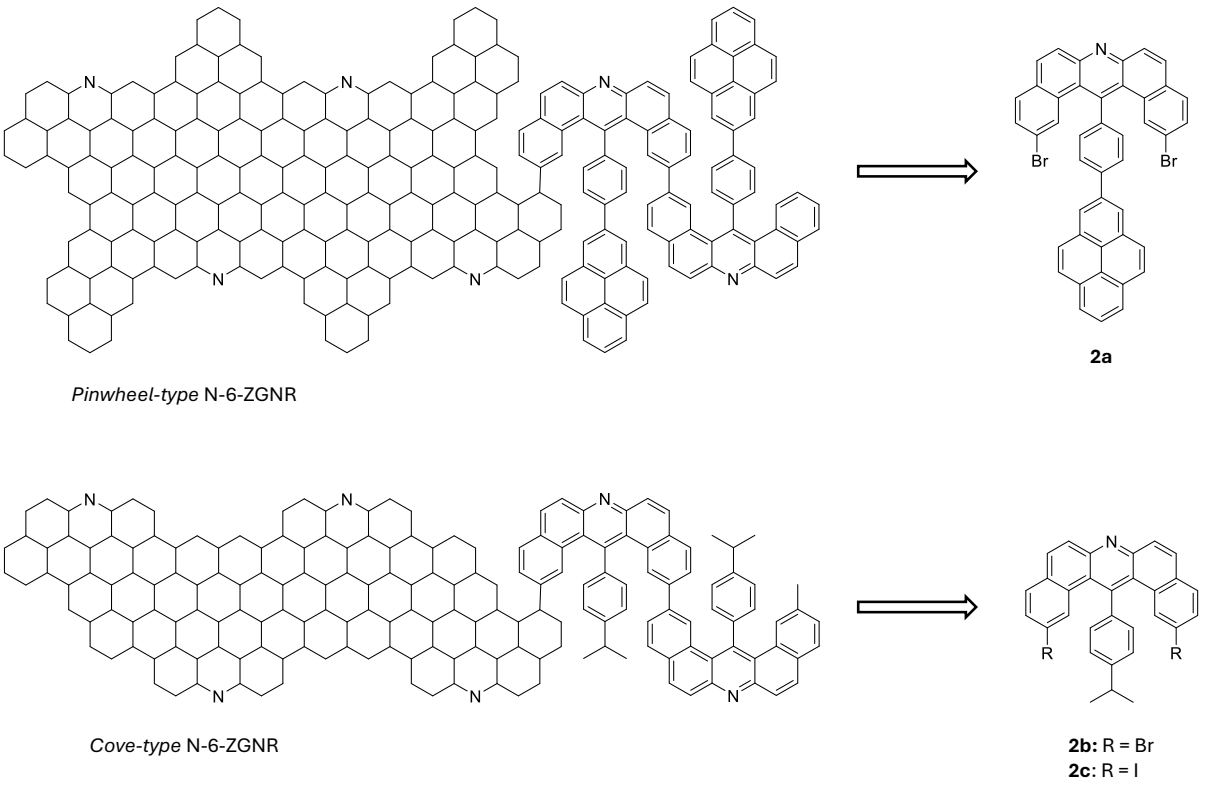

Figure 1.9 Schematic of design strategy to grow pinwheel-type (cove-type) N-6-ZGNRs from precursor **2a** (**2b,2c**), with chemical structures of precursors shown.

resulting in precursors **2a** (**2b,c**) targeting GNRs which will be deemed “pinwheel” (“cove”)-type 6-N-ZGNR, as shown in Figure 1.9.

Precursor **2a** was deposited onto a freshly cleaned Au(111) surface under UHV conditions. Relatively high evaporator temperatures (> 200 °C) were required to sublime this molecule making it difficult to produce high coverage molecular thin films due to contamination or decomposition at high temperatures. STM imaging revealed a relatively low surface coverage of the precursor, where molecules tended to form isolated dimers held together by hydrogen-bonding like interactions driven by the dipole of the N-C bond. Subsequent annealing of the substrate at incremental temperatures eventually resulted in cyclodehydrogenation of the monomer around 300 °C. However, no polymerization was observed. Instead, nearly every molecule observed on the surface remained in isolated dimers (Figure 1.10A). The cyclodehydrogenation of the molecular precursor was confirmed with BRSTM, shown in Figure 1.10B. This suggests that, like the growth attempts of [4]TCOF from brominated [4]-triangulene, dehalogenation and cyclodehydrogenation occur at roughly the same temperature for this precursor. Instead of forming undesired covalent bonds, the strong H-bonding-like interaction which drives the dimer formation prevents any polymerization or surface reaction whatsoever. Unfortunately, synthesis of the iodinated version of this precursor was not feasible at the time these experiments were performed.

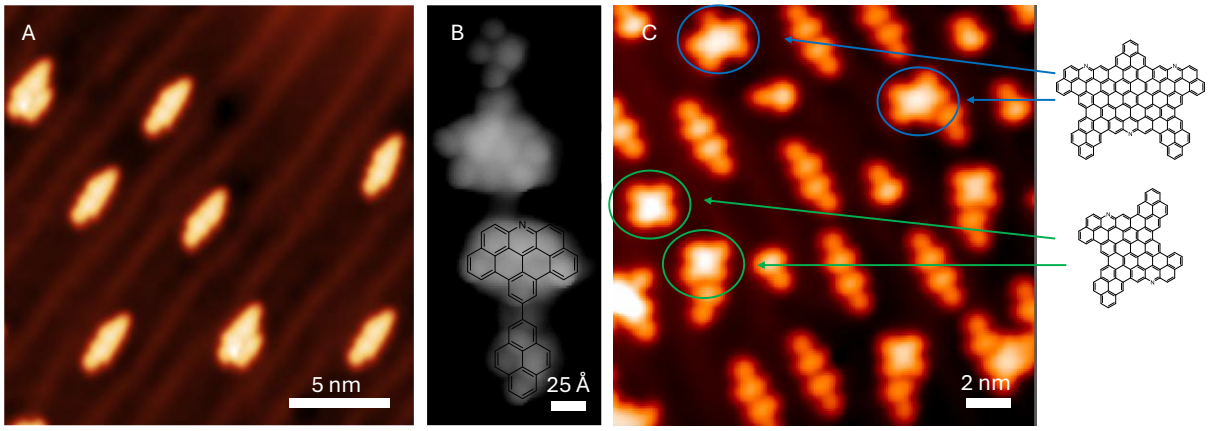

Figure 1.10 (A) STM topographic image of precursor **2a** as deposited on Au(111), forming isolated dimers on the surface. **(B)** Constant-current BRSTM image of cyclodehydrogenated dimers after substrate annealing to 300 °C. The structure for the cyclodehydrogenated monomer is overlain on the image. (V_s = 5 mV, V_M = 4 mV, I = 300 pA). = **(C)** STM topographic image of precursor **2a** transferred onto Au(111) using DCT after annealing to 300 °C. Dimers and trimers formed from desired C-C bond formation are highlighted in green and blue circles, respectively, and their suggested structures are given. STM topographic images were obtained with V_s = 0.50 V and I = 20 pA. All STM experiments were performed at T = 4.2 K.

Experiments were also attempted using DCT to deposit **2a** on Au(111) hoping to obtain a higher surface concentration of monomer which would facilitate polymerization. The molecule in crystalline form was carefully applied to a fiberglass applicator containing a tungsten filament, which was then briefly contacted with the Au(111) under UHV conditions following degassing of the molecule through resistive heating of the filament. The substrate was then annealed very slowly to 300 °C to induce polymerization and cyclodehydrogenation. STM imaging revealed a much higher density of molecules on the surface in some areas. While most molecules remained in the noncovalent dimers, even after attempting to optimize the growth parameters, some dimers and trimers which appeared to exhibit the desired covalent bonding pattern were observed, as shown in Figure 1.10C. Having exhausted all available growth optimization and deposition procedures, we concluded that strong non-covalent intermolecular attraction and limited diffusion of monomers due to large molecular weight were insurmountable challenges in the growth of pinwheel-type 6-Z-GNRs from precursor **2a**.

Attempts were also made to grow cove-type 6-N-ZGNRs by subliming precursor **2b** onto Au(111) under UHV conditions with an evaporator temperature of roughly 170 °C. Substrate annealing at incremental temperatures was then performed to induce polymerization at the brominated sites. STM imaging of the substrate did reveal some 1D chain formation, but closer inspection revealed that the chains were composed of dimers which assembled into chains driven again by H-bonding like interactions along the acridine moiety, shown in Figure 1.11A,B. The dimers themselves appeared to be covalently bound by 6-membered ring linkers formed from the cyclization of isopropyl groups on individual monomers, confirmed by BRSTM in 1.11C,D. The same behavior was observed in studies attempting to grow ZGNRs with oxygen and boron edge dopants where the precursor contained a central isopropyl group.[80] The cyclization of isopropyl groups has been previously reported and strategically employed to form phenyl ring chains on Au(111).[81] Much like attempts to grow pinwheel-type 6-N-ZGNRs from precursor **2a**, full cyclodehydrogenation of the **2b** was observed without any trace of the desired polymerization motif occurring.

Motivated by successful modification of [4]TCOF precursors to favor halogen cleavage at lower temperatures, precursor **2c** was synthesized, also designed to form cove-type 6-N-ZGNRs, featuring iodine at the desired polymerization sites. **2c** was sublimed onto Au(111) using the same conditions as precursor **2b**. Upon slow annealing of the substrate to 300 °C, STM imaging revealed what appeared to be dimers bound at the halogenated site of the monomer (Figure 1.11E). While these dimers apparently formed the desired intermediate for the surface-assisted Ullman-type coupling in the absence of cyclization at the isopropyl sites, no chains were

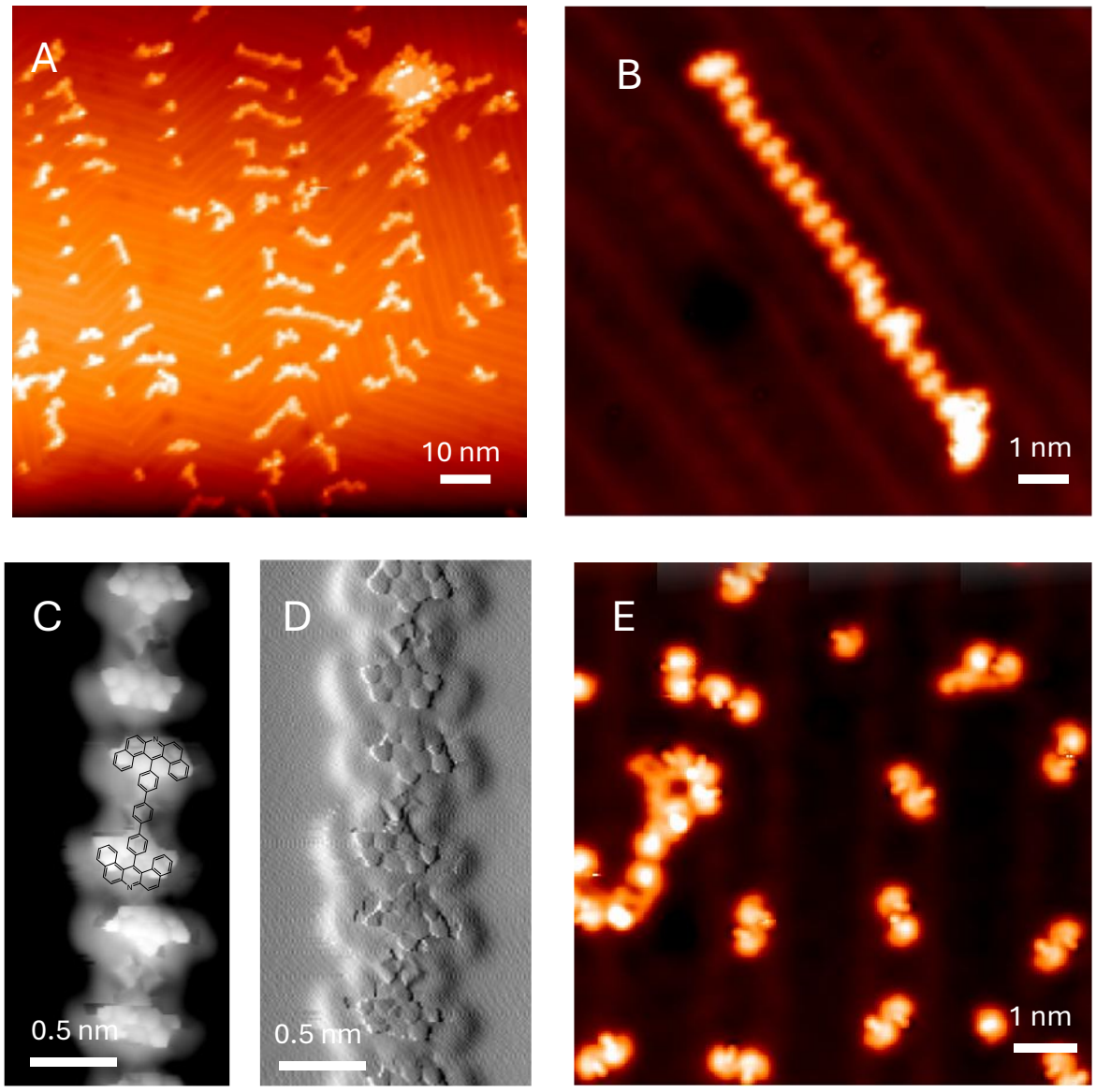

Figure 1.11 (A) Large scale STM topographic image of precursor **2b** on Au(111) after annealing the substrate to 300 °C showing self-assembled chains. **(B)** Close-up STM topographic image of the chains shown in **A**, revealing dog-bone shaped units. **(C)** Constant-current BRSTM image of chains formed by **2b,** revealing covalently bound dimers in hydrogen bonded chains (V_s = 5 meV, V_M = 4 meV, I = 300 pA). **(D)** Laplace filtered image of C, further elucidating the chemical structure of the chains. **(E)** STM topographic image of precursor **2c** on Au(111) after substrate annealing to 300 °C. All STM topographic images were collected with V_s = 0.5 V and I = 20 pA at 4.2 K.

observed and further substrate annealing resulted in decomposition of the precursor. The mechanism for the dimerization of these monomers remains to be understood.

While we were unsuccessful in our attempts to fabricate edge-modified 6-N-ZGNRs, the formation of C–C bonds between isopropyl groups on precursor **2b** inspired us to investigate whether this was a feasible surface synthesis motif for 1D nanographenes grown from similar scaffolds. We designed precursor **2d** (Figure S2) to form the 1D nanographene shown in Figure S2, with monomers linked by 6-membered rings formed between isopropyl groups.

Precursor **2d** was deposited on Au(111) under UHV with similar conditions to precursors **2b** and **2c**. STM imaging revealed 1D structures which also appeared to be driven by H-bonding like interactions, this time assembled in a "head-to toe" orientation resulting chain formation without any covalent bonding between monomers, as opposed to the "head-to-head" self-assembly pattern of precursors **2a–c**. Substrate annealing following deposition did not result in any covalent bond formation. See Figure S2.

We attribute the failures to grow ZGNR derivatives using this molecular building block to the strong H-bonding like intermolecular attractions which prevent the monomers from aligning in the correct orientation for polymerization to occur. Despite success with growing 6-N-ZGNRs from similar precursors, the growth limitations appear to be exacerbated for the pinwheel and cove-type 6-N-ZGNRs grown from precursors **2a–c**. Although the growth of 1D nanographenes from precursor **2d** was unsuccessful, the cyclization of isopropyl groups as a strategy for C–C bond formation in nanographene synthesis remains largely unexplored and could enable access to novel carbon nanostructures not obtainable through conventional surface-assisted Ullman-type coupling.

1.7 Topology in GNRs

Topology is an abstract mathematical concept that describes global properties of a space which are invariant under deformations and transformations[82] and has been extended to describe electronic phases which are highly robust to decoherence and perturbation.[83] As such, materials with topological phases are highly intriguing for the development of qubit arrays and other quantum architectures.[84,85] Understanding and exploiting these properties of matter has inspired many opportunities in materials research and design.

A simple analogy can be drawn between the path of adiabatic electronic transformations in topological systems and the Mobius strip,[86] which is a fundamental example of geometric topology. The Mobius strip is a topological surface created by joining two ends of a quasi-1D shape (i.e. long rectangular strip), following a 180 ° rotation of one end orthogonal to the surface. Although it is a one-sided surface, it takes two spatial rotations to move along the surface before returning to the initial location. Analogously, an electron in a non-topological band can be thought of as traveling in a normal circular path as it undergoes an adiabatic transformation, where one evolution returns it to its original state. An electron in a topological band, however, may wind two or more times before returning to the original state.[87]

The Berry phase[87] (or Zak phase in 1D/quasi-1D systems)[88] is a property that is derived from the path of an adiabatic movement of an electron within k-space. Throughout this evolution, the electron acquires a (Berry/Zak) phase, the geometry of which is defined by the electronic wave function and reflects how the electron "winds" before returning to its original state.[87–89]

The Zak phase, γ_{nk}, can be used to determine or classify the topology of specific bands and is defined by equation 1.4, where *k* is the wave vector, *a* is the length of the unit cell, and u_{nk} is the periodic component of the Bloch function for the band indexed by *n*.[90]

$$\gamma_{nk} = i\left(\frac{2\pi}{a}\right)\int_{-\pi/a}^{\pi/a} dk \left\langle u_{nk}\middle|\frac{\delta u_{nk}}{\delta k}\right\rangle \qquad \textbf{1.4}$$

The $\mathbb{Z}_2$ invariant is calculated from the Zak phase in 1D systems and is a binary index, meaning the two possible values for the invariant are 0 and 1, which reflect trivial and nontrivial topological phases in materials, respectively. The topological character of a 1D insulator is related to the Zak phase by summing over all occupied bands, and the $\mathbb{Z}_2$ invariant is determined by equation 1.5.[90]

$$(-1)^{\mathbb{Z}_2} = \exp(i\sum_n \gamma_n) \qquad \textbf{1.5}$$

Topological phases in GNRs have been extensively studied and a versatile system has been developed by Cao et al. which can simplify the calculation of the $\mathbb{Z}_2$ invariant in GNRs based on their symmetries, as shown in Table 1.1. This allows us to easily determine the topological nature of the GNR and predict the formation of symmetry protected topological states (SPTs), which localize at junctions between trivial and topological phase spaces.

Termination type	Zigzag (*N* = Odd)	Zigzag' (*N* = Odd)	Zigzag (*N* = Even)	Bearded (*N* = Even)
Unit cell shape	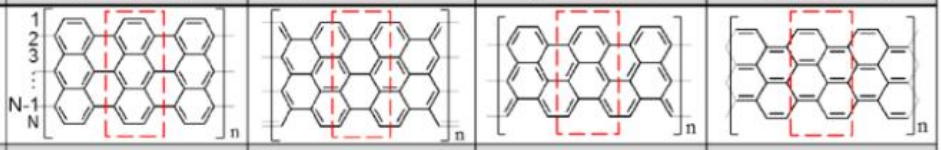			
Bulk Symmetry	Inversion/mirror	Inversion/mirror	Mirror	Inversion
Z_2	$\frac{1+(-1)^{\lfloor\frac{N}{3}\rfloor+\lfloor\frac{N+1}{2}\rfloor}}{2}$	$\frac{1-(-1)^{\lfloor\frac{N}{3}\rfloor+\lfloor\frac{N+1}{2}\rfloor}}{2}$		$\frac{1-(-1)^{\lfloor\frac{N}{3}\rfloor}}{2}$

Table 1.1 Categorization of topological groups of AGNRs distinguished by odd or even *N* (number of carbon atoms along the lateral zig-zag direction) and unit cell (edge) termination, which is shown by the dashed boxes. The expression for determining the $\mathbb{Z}_2$ invariant in each system is given in the bottom row. Reproduced from Ref 90.

SPTs in topologically nontrivial GNRs manifest as singly occupied end-states, where the terminating edges of the GNR can be thought of as a topological phase boundary between vacuum (trivial) and the GNR (topological). For example, 7-AGNRs with zigzag termination will host an unpaired electron localized at each end due to the topological nature of the band structure. On Au(111), a zero-bias peak is observed in the STS spectrum localized at the 7-AGNR ends, which results from the Kondo interaction between the unpaired electron – acting as a magnetic surface defect – and the conduction electrons in the substrate.[91] The nanographene length threshold for the generation of these SPT end-states prohibits the observation of magnetic exchange between them in pristine 7- or 9-AGNRs due to their spatial distance, and

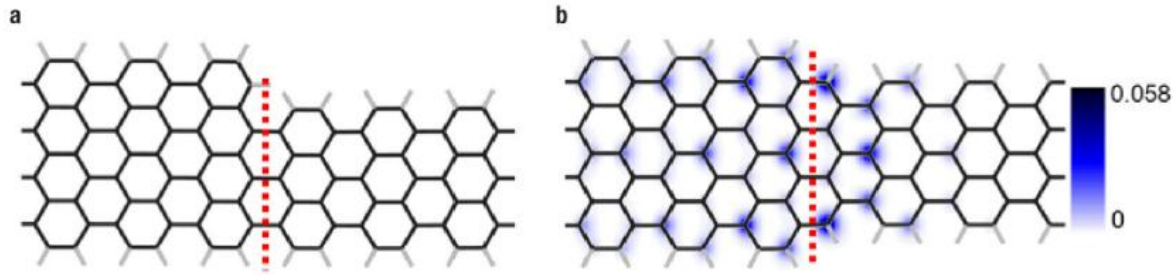

Figure 1.12 (A) Heterojunction formed between 7- and 9-AGNRs which both have zigzag termination with $\mathbb{Z}_2 = 1$. The boundary between equivalent topological phases results in no SPT formation. **(B)** Heterojunction formed between 7- and 9-AGNRs where the 7-AGNR has zigzag' termination ($\mathbb{Z}_2 = 0$), and the 9-AGNR has zigzag termination ($\mathbb{Z}_2 = 1$), resulting in a topological phase boundary and emergent SPT. Reproduced from Ref 90.

thus their magnetic moments are completely screened by Kondo interactions.[91]

Exploiting these topological properties in GNRs and creating robust SPTs which can weakly interact could be a great advancement for designing robust entangled qubits in solid-state systems. To accomplish such a feat, it is advantageous to install the SPTs periodically with tunable separation throughout the GNRs by engineering topological phase boundaries into the atomic structure. This can be realized by fusing two types of GNRs with different topological invariants defined by their edge termination. For example, 7 and 9AGNRs can both be topological or trivial depending with zigzag or zigzag' edge termination, respectively. If they are joined in a certain way which preserves the topological unit cell for one and the trivial unit cell for the other, an SPT can emerge at the junction between them, as shown in Figure 1.12.[90]

7/9-AGNR heterojunctions have been predicted to host zero-mode topological states, which was confirmed experimentally by Rizzo et al.[28] Their experiments hinged on a carefully designed precursor (precursor **1** in Figure 1.13A) which is designed to grow AGNRs with periodically alternating 7- and 9-AGNR segments (Figure 1.13B). Emergent topological bands were observed flanking the Fermi energy, (Figure 1.13C,D) resulting from hybridization of the periodic SPTs.[28]

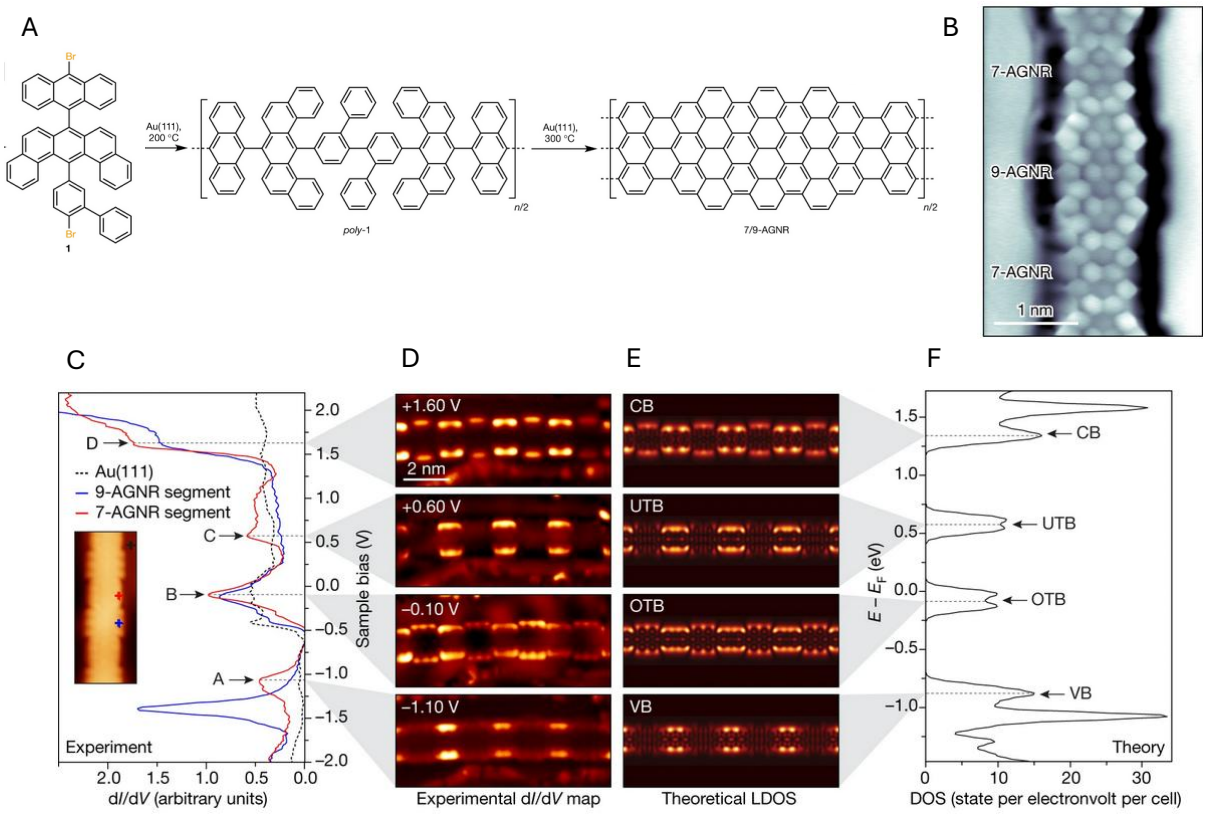

Figure 1.13 (A) Structure for topological 7/9-AGNR precursor and schematic for on-surface synthesis of topological 7/9-AGNRs. **(B)** BRSTM image of 7/9-AGNR featuring topological heterojuntion. **(C)** d*I*/d*V* spectroscopy collected on 7/9-AGNRs collected at locations shown in the inset. Topological bands are labeled B and C. **(D)** d*I*/d*V* maps collected at energies corresponding to labeled peaks in **C**. **(E)** DFT calculated projected LDOS maps for the CB, VB, and topological bands (UTB, LTB). **(F)** DFT calculated DOS for topological 7/9-AGNR. Reproduced from Ref 28.

To further understand the behavior of interacting SPTs in GNRs, the precursor was also co-deposited with compatible 7-AGNR (9-AGNR) precursors to fabricate 7-AGNRs (9-AGNRs) with discrete 9-AGNR (7-AGNR) sections installed, deemed 7/9/7 (9/7/9) topological quantum dots (TQDs). STS at these heterojunctions also revealed in-gap states absent in pristine 7- or 9-AGNRs resulting from exchange interactions between adjacent SPTs.[29]

1.8 9/7/9 Double quantum dot (DQD)

While the work performed by Rizzo et al. provides extremely useful insight into topological properties of GNRs, the distance and therefore strength of hybridization between SPTs in the double-heterojunctions are predetermined by the size of the precursor.[28,29] To further understand the behavior of SPTs in GNRs, it would be useful to tune a specific parameter such as the spatial separation between sites where the SPTs localize and determine how changing the hopping amplitude between SPTs results in changes to the STS spectrum.

Our strategy to synthesize a GNR containing a 9/7/9 double heterojunction with a tunable distance and interaction strength between SPTs was focused on co-depositing the 7-AGNR precursor 10,10'-dibromo-9,9'-bianthracene (DBBA) with precursor **3a** to cap 7-AGNRs of various lengths with 9-AGNR segments, as shown in Figure 1.14B. **3a** was designed with a non-topological 9-AGNR termination group to prevent coupling between 9-AGNR end states and SPTs emerging from the 7/9 heterojunction.[92]

Initial efforts to sublime precursor **3a** onto Au(111) resulted in decomposition of the molecule likely due to its high molecular weight. Attempts to transfer the molecule using DCT were also unsuccessful. These challenges associated with depositing high molecular weight compounds and other macromolecules/nanomaterials necessitate the use of more sophisticated techniques such as matrix assisted direct contact (MAD) transfer, which I will detail in Chapter 2.

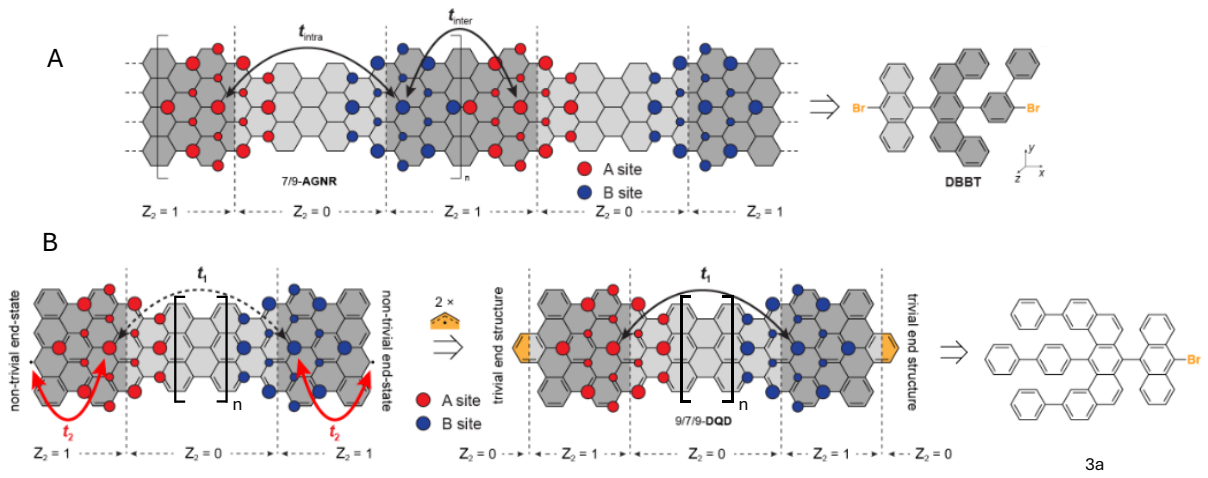

Figure 1.14 (A) Diagram of SPTs in 7/9-AGNRs with periodic SPTs featuring intercell and intracell (t_{inter} and t_{intra}), at fixed lengths as defined by precursor DBBT. **(B)** Schematic for design of 9/7/9 DQD (right) which features topologically trivial edge termination to suppress hopping between heterojunction SPTs and end states. Precursor **3a** was designed to cap varying lengths of 7-AGNR segments formed from DBBA, ideally enabling tunability of t_1.

MAD transfer successfully enabled STM characterization of precursor **3a** on Au(111). The substrate was annealed to 150 °C to remove the pyrene matrix (see Chapter 2) following which the temperature was slowly increased to 300 °C to induce dimerization and cyclodehydrogenation (Figure 1.15A). Subsequent STM imaging revealed a small surface concentration of cyclized dimers (9/7/9 DQD) as well as cyclized monomers (7/9 QD) (Figure 1.15B,C,D).

STS was performed on the resulting 9/7/9 DQD and the 7/9 QD (Figure 1.16A,B). Spectra collected on 7/9 QD were nearly featureless regardless of tip location, as expected for a small PAH. Spectra collected on the 9/7/9 DQD near the heterojunction, however, exhibited two

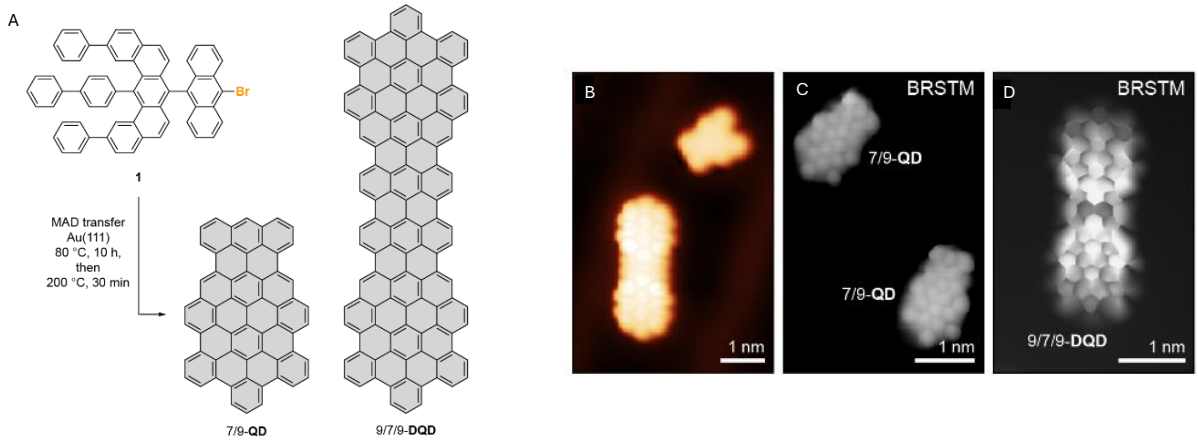

Figure 1.15 (A) Schematic of MAD transfer and surface-catalyzed dimerization and cyclodehydrogenation of precursor 3a to yield 7/9-QD and the 9/7/9-DQD. **(B)** STM topographic image of a 9/7/9 DQD and a 7/9-QD with a missing phenyl ring. **(C)** BRSTM image of isolated 7/9-QDs. **(D)** BRSTM image of isolated 9/7/9-DQD.

distinct low-bias peaks at V_s = 0 (peak 3) and 160 mV (peak 2) which were relatively sharp and broad, respectively (Figure 1.16A). Spectra collected at the 9-armchair (7-armchair) edge showed much larger prominence of peak 3 (peak 2) than peak 2 (peak 3). This is reflected in the d*I*/d*V* maps (Figure 1.16C–F), where LDOS is localized at the 9-AGNR (7-AGNR) segments at V_s = 3 mV (160 mV) associated with peak 3 (peak 2). First-principles DFT calculations under the local density approximation (LDA) predict a quasiparticle HOMO-LUMO gap of 0.158 eV (Figure 1.16K), which aligns extremely well with experimental results. Moreover, simulated LDOS projections at the HOMO and LUMO energies exhibit nodal patterns which match well with d*I*/d*V* maps obtained at energies corresponding to peaks 2 and 3 (160 and 0 meV) (Figure 1.16G–J). We report a surprisingly small experimental HOMO-LUMO gap of $E_g \approx 160$ meV in

the 9/7/9 DQD dimer, likely arising from SPTs. This demonstrates that the framework for understanding and engineering SPTs in 1D GNRs can be extended to 0D molecular systems.

Attempts to grow 7-AGNR segments terminated by 7/9 QDs by depositing DBBA on the substrate following the MAD transfer process were unsuccessful. Only 9/7/9 DQD dimers, 7/9 QD monomers, and regular 7-AGNRs were observed on the surface after incremental annealing up to 350 °C.

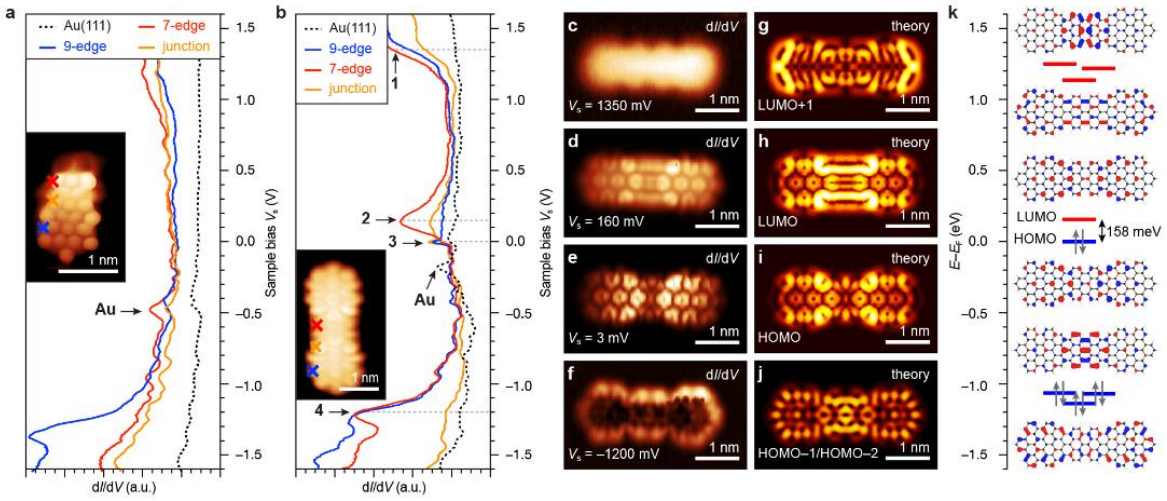

Figure 1.16 (A,B) –point spectra recorded on 7/9-QD and 9/7/9-DQD, respectively, at locations indicated in the inset images. **(C–F)** Constant-height –maps recorded on 9/7/9 DQD at biases corresponding to peaks labeled in **B**. **(G–J)** DFT LDOS projections for states electronic states corresponding to maps in **C**–**F**. **(K)** Calculated molecular orbital energies for 9/7/9-DQD, with the HOMO energy set to E_F.

1.9 7/5/7 GNR heterojunction growth attempts

Heterojunctions between 5- and 7-AGNRs can also produce SPTs. One way to access the 5/7 GNR heterojunction is by using Clar's goblet, which intrinsically hosts a topological frustration-induced open-shell singlet ground state, as a molecular building block. Initial attempts to fabricate 7/5/7 GNRs from precursor **4a** (Figure S3) resulted in defected GNRs containing multiple 5-membered rings which convoluted electronic characterization, although recent works have successfully synthesized and characterized this GNR.[93]

A precursor targeting an extended version of the 7/5/7 GNR, precursor **4b** (Figure S3), was designed and synthesized. Precursor **4b** was sublimed onto Au(111) under UHV conditions with an evaporator temperature of 190 °C. The substrate was then annealed at incrementally increasing temperatures to induce polymerization and cyclodehydrogenation. In the STM images obtained, very little polymerization was observed. Many monomers appeared to have undergone cyclodehydrogenation in the absence of polymerization, but a small number of dimers, many defective-looking, formed. The results of these experiments are shown in Figure S3.

1.10 Outlook

While on-surface synthesis of carbon nanomaterials has expanded to a vast repertoire of intriguing structures, there are some fundamental limitations and restrictions associated with the growth technique. In most cases, these processes are highly defect prone and it is difficult to synthesize pristine 1D and 2D structures that extend beyond the 10–20 nm range. Investigating other surface reactions that could lead to C–C bond formation, for example the coupling of isopropyl groups seen with precursor **2b** (Figure 1.11), could open new channels for the synthesis of these materials which could provide less defective structures.

Chapter 2 – Deposition and transfer techniques for polymers and other nanomaterials

While surface-assisted Ullman-like coupling synthesis techniques for growing GNRs and other graphitic nanomaterials have been widely successful at accessing a variety of structural moieties, there are some fundamental limitations. Most notable is the requirement that polymerization sites in the molecular precursors must be structurally symmetric for homogenous growth to occur. For GNRs, except in rare cases where the monomers adopt a strong orientational preference during polymerization,[94] this implies that the precursors must contain a mirror symmetry plane perpendicular to the growth/polymerization axis. Other growth parameters such as GNR length dispersity are also nearly impossible to control using this technique.

In-solution synthesis and polymerization techniques can access GNRs or polymeric GNR precursors with more sophisticated structures, and living polymerization methods can be employed to control the length and dispersity of resulting GNRs. Previous attempts to produce solution-synthesized GNRs have hinged on the Scholl reaction[95] to promote graphitization of the precursor polymers and used techniques such as Raman spectroscopy on resulting thin films to identify the distinctive signals associated with GNRs as evidence for their formation.[96] However, true structural characterization of solution-synthesized GNRs or polymer precursors remains a fundamental challenge, and the efficacy of the Scholl reaction for producing pristine, defect-free GNRs is unknown. Such materials cannot be sublimed in UHV without chemical decomposition and employing DCT to transfer them to substrates for characterization is unreliable due to aggregation of the material.

2.1 MAD transfer

Matrix assisted direct contact (MAD) transfer[97] (Figure 2.1) is a modified DCT technique that has successfully been employed to achieve isolated polymers and non-volatile PAHs (such as the 9/7/9 DQD precursor discussed in chapter 1)[92] on substrates for STM characterization. For GNR polymer precursors, this is performed on an Au(111) substrate which is then used to catalyze the cyclodehydrogenation of the polymer yielding the desired GNR. This technique hinges on dissolving the target material (e.g. polymer precursor) in molten pyrene with a concentration under 1 % by weight, and subsequently flash cooling to induce crystallization of the pyrene matrix while preventing co-crystallization of the polymer. This results in a solid matrix with isolated polymers or molecules dispersed throughout, which can be then ground into a fine powder, which is then transferred to the surface in UHV using a fiberglass applicator, analogous to a DCT technique. The substrate is then carefully annealed to disperse the matrix across the surface, then sublime away the pyrene matrix, and finally induce cyclodehydrogenation of isolated polymer precursors.[97]

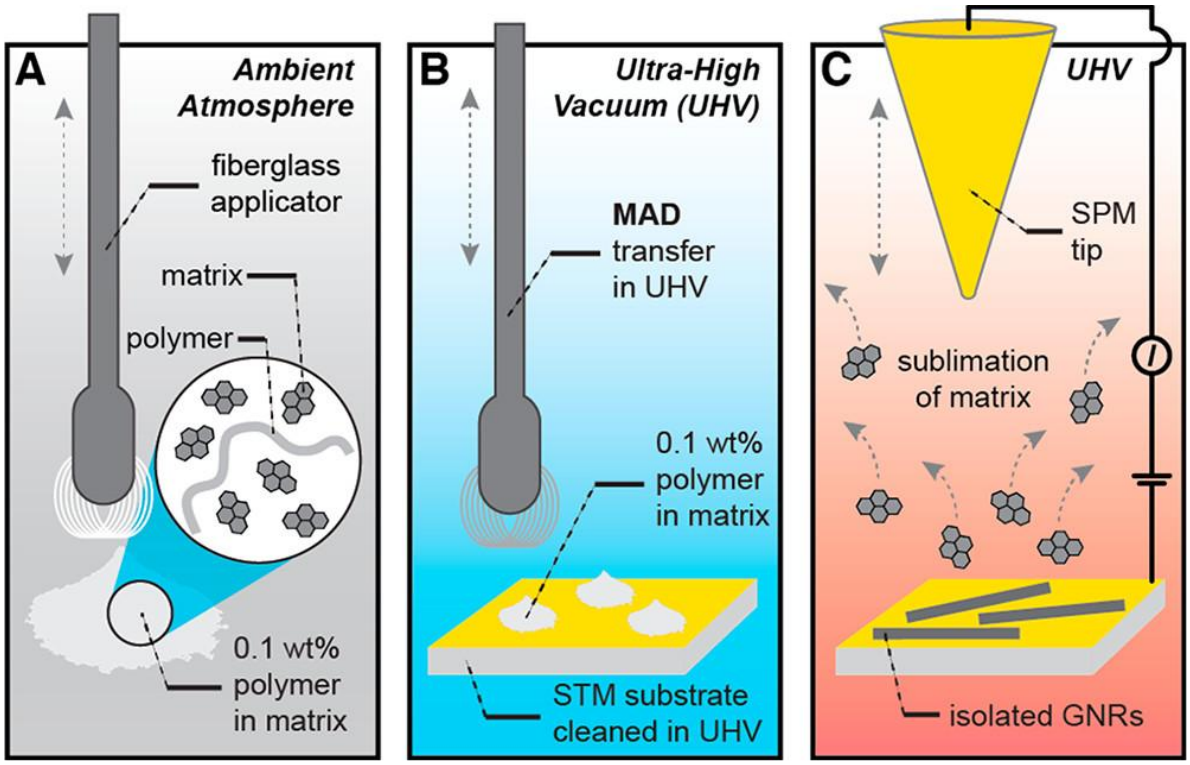

Figure 2.1 Schematic representation of MAD transfer process. **(A)** A fiberglass applicator is coated with a polymer dispersed in a pyrene matrix. **(B)** The applicator is then brought into UHV where it is contacted to a clean Au(111) surface. **(C)** The substrate is annealed to remove the pyrene matrix before characterization with STM. Reproduced from Ref 97.

This technique was first demonstrated using solution-synthesized chevron and N-doped 7 armchair GNR polymer precursors to form isolated GNRs on Au(111)[97] and has since been extended to achieve GNR structures which would have been previously inaccessible using on-surface polymerization methods.[43,98]

2.2 Length controlled polymerization of 9-AGNR precursors

Other parameters which solution-synthesis techniques can control much more effectively than on-surface methods include the length dispersity of polymers and resulting GNRs, well as the structure of the end-group. While iterations of alternating cross coupling and deprotection reactions have been used to synthesize oligomeric GNRs with precise length and end-group termination, this process involves attaching monomers to a chain one-by-one, which is a very tedious synthetic process.[98] A linear synthesis approach which can achieve GNR polymer precursors of consistent length with modifiable edge termination would represent a major achievement in the field of GNR synthesis towards the integration of GNRs into functional devices.

The experiments discussed on this section rely on living polymerization techniques, specifically Suzuki catalyst-transfer polymerization (SCTP),[99–101] to synthesize 9-AGNR polymer precursors with low length dispersity and tuneable edge termination. In this process, a bifunctional monomer (**M**) is used (e.g. precursors **1a** and **1b** in Figure 2.2A) which features a halide (Br) and a boronic ester at the desired polymerization sites, i.e. at the *para* positions of the central phenyl ring. A palladium cross-coupling catalyst (e.g. compound **2** in Figure 2.2A), the ligand (highlighted in blue) structure of which defines one of the end-groups in the resulting GNR, acts as an initiator (**I**) and catalyzes the extension of the bifunctional monomer **M** in one dimension. The Pd inserts into the C–Br bond of the monomer and induces transmetalation with an arylboronate ester of another monomer, followed by reductive elimination after which the Pd catalyst remains on the polymer chain and ring-walks to the last phenyl ring in the chain. It then re-inserts into the next C–Br bond to propagate the addition of another monomer. When the desired chain length is achieved, a terminator (**T**) (e.g., compound **3** in Figure 2.2A), which determines the end group functionalization on the other side of the GNR, is added to quench the catalyst and stop polymerization. This inhibits competing chain transfer and termination events which plague conventional step-growth polymerizations with high length dispersity *Đ, where Đ = M_n/M_w*, M_n is the number average molecular weight, and M_w is the weight average molecular weight. The technique also ensures that the molecular weight of the polymers and the resulting GNR length can be precisely controlled by tuning the monomer to initiator loading ratio, $\mathbf{[M]_0/[I]_0}$.[43]

SCTP synthesis of 9-AGNR polymers of varying lengths performed with precursors **1a** and initiator **2**, shown in Figure 2.2A, resulted in very low dispersity ($Đ < 1.2$) for polymers with less than twenty repeat units, but showed higher dispersity for larger chains (Figure 2.2B). This is due to decreased solubility in larger polymer chains, as evidenced by the consistently lower *Đ* in long polymers grown from precursor **1b** featuring alkyl solubilizing groups (Figure 2.2B). A linear relationship between M_n and percent conversion was observed indicating living polymerization. (Figure 2.2E). Matrix-assisted laser desoroption/ionization time-of-flight (MALDI-TOF) mass spectrometry revealed periodic peaks with m/z separation consistent with the mass of the monomer (Figure 2.2C). The length of the GNR polymer precursors was estimated by comparing the integrations of NMR signals associated with protons on the end functional groups from the terminator/initiator and the monomer (e.g. aldehyde and dimethyl acetal on **poly-1b**, Figure 2.2G), which closely matched $\mathbf{[M]_0/[I]_0}$ suggesting high termination efficiency consistent with low *Đ*.

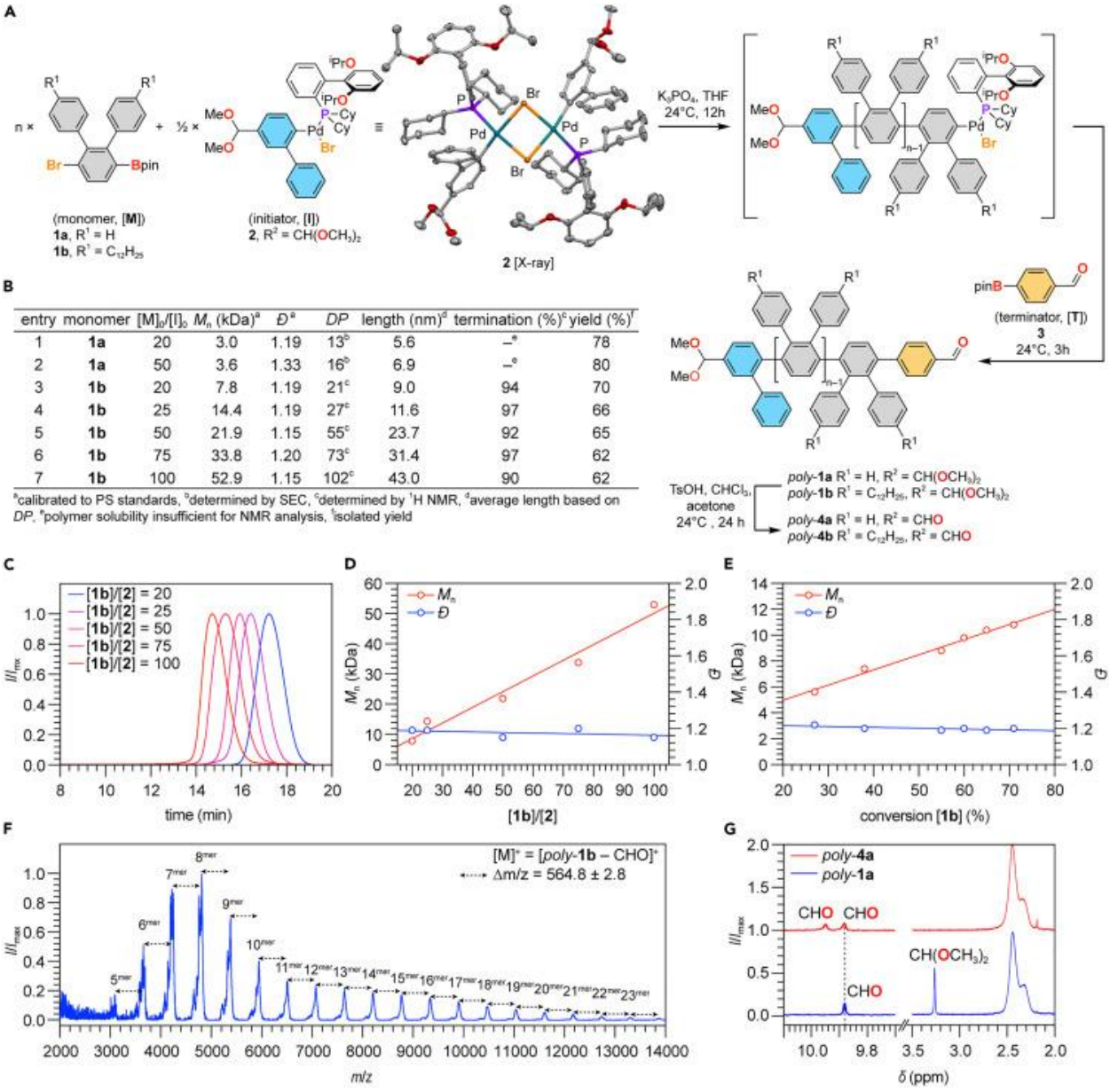

entry	monomer	$[M]_0/[I]_0$	M_n (kDa)[a]	$Đ$[a]	DP	length (nm)[d]	termination (%)[c]	yield (%)[f]
1	**1a**	20	3.0	1.19	13[b]	5.6	–[e]	78
2	**1a**	50	3.6	1.33	16[b]	6.9	–[e]	80
3	**1b**	20	7.8	1.19	21[c]	9.0	94	70
4	**1b**	25	14.4	1.19	27[c]	11.6	97	66
5	**1b**	50	21.9	1.15	55[c]	23.7	92	65
6	**1b**	75	33.8	1.20	73[c]	31.4	97	62
7	**1b**	100	52.9	1.15	102[c]	43.0	90	62

[a]calibrated to PS standards, [b]determined by SEC, [c]determined by ^{1}H NMR, [d]average length based on *DP*, [e]polymer solubility insufficient for NMR analysis, [f]isolated yield

Figure 2.2 SCTP synthesis of 9-AGNR polymer precursors. **(A)** Schematic of polymerization process, showing structures of o-terphenylene monomers **1a,b** (**M**), palladium complex initiator (**I**) including single X-ray crystal structure, terminator (**T**), and polymers **poly-1a**,**1b**,**4a**, and **4b**. **(B)** Summary of size exclusion chromatography (SEC) data, estimated length, termination efficiency, and yield of **poly-1a**,**b** at varying $\mathbf{[M]_0/[I]_0}$. **(C)** SEC traces of **poly-1b** samples. **(D)** M_n and $Đ$ plotted at varying loading ratios. **(E)** M_n and $Đ$ plotted as a function of monomer conversion. **(F)** MALDI-TOF spectroscopy of **poly-1b** samples. **(G)** ^{1}H-NMR spectra of **poly-1b** (blue) and **poly-4b** (red), featuring signals at δ = 3.27 ppm (dimethyl acetal) and 9.95 ppm (aldehyde).

2.3 MAD transfer of 9-AGNR polymer precursors

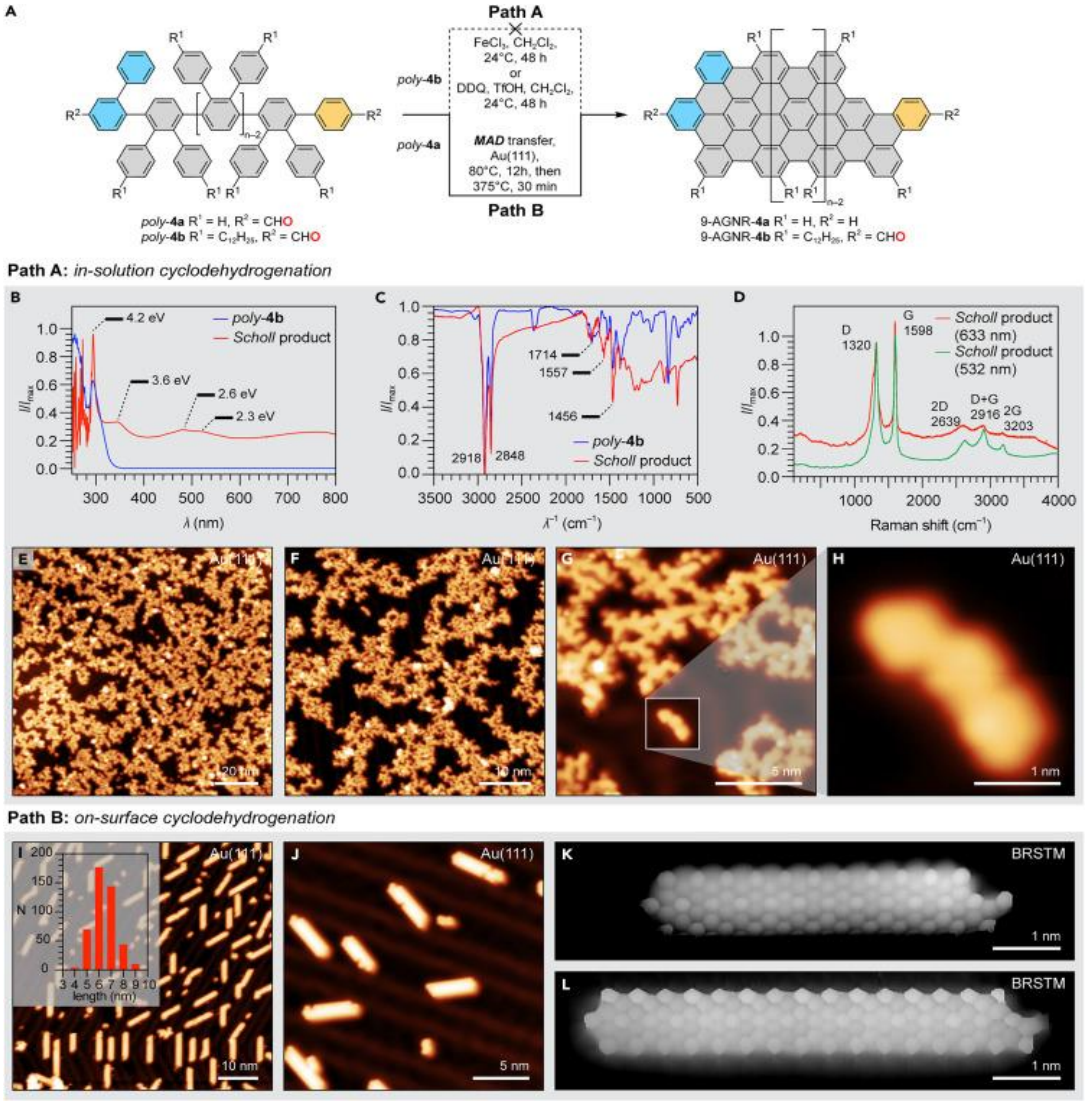

Figure 2.3 (A) Schematic of in-solution cyclodehydrogenation (path A) and surface catalyzed cyclodehydrogenation (path B) of **poly-4a,b**. **(B)** UV-Vis spectra of solution-cyclized **poly-4b**. **(C)** IR spectra of solution-cyclized **poly-4b**. **(D)** Raman spectroscopy of solution cyclized **poly-4b**. Excitation laser set to 633 nm and 532 nm. Spectra offset for clarity. **(E–H)** Topographic STM images of solution cyclized **poly-4b** transferred on Au(111) with MAD transfer (V_s = 200 mV, I = 20 pA). **(F,J)** Topographic STM images of **poly-4b** transferred to Au(111) using MAD transfer following surface catalyzed cyclodehydrogenation (V_s = 100 mV, 50 mV; I = 20 pA). **(K,L)** Constant-height BRSTM images of resultant 9-AGNRs with predicted edge structure using a CO functionalized tip. (V_s = 10 mV, V_M = 10 mV). All STM experiments were conducted at 4K.

In-solution cyclization of **poly-4b** was attempted via the Scholl reaction. While vibrational infrared (IR) spectroscopy revealed characteristic alkyl and aryl C–H vibrational modes at (2,918, 2,848, and 1,456 cm^{-1}) and Raman spectroscopy showed distinct D and G peaks associated with most graphene nanomaterials, the radial breathing-like mode for 9-AGNRs was not observed (Figure 2.3C,D).[102] Attempts to transfer the resulting material to substrates for STM characterization using MAD transfer resulted in amorphous carbon networks with indistinguishable chemical structure (Figure 2.3E–H). Attempting to cyclize **poly-4a** in solution was infeasible due to insolubility which only increases as C–C bonds are formed during the Scholl reaction.

MAD transfer was also attempted directly with **poly-4b** but was also unsuccessful and resulted in amorphous carbon films. This result was surprising light of previous successes with MAD transfer enabled characterization of other GNR polymer precursors. We hypothesize that the presence of solubilizing alkyl chains causes unwanted crosslinking reactions on the surface resulting in these amorphous carbon networks.

MAD transfer of **poly-4a**, however, yielded GNRs with consistent lengths and predicted edge terminations following surface-assisted cyclodehydrogenation (Figure 2.3I,J). The ideal concentration of **poly-4a** in the pyrene matrix was carefully optimized to a ratio of 1 : 5000 by weight. The powder was then coated on a fiberglass applicator fitted with a tungsten filament and brought into UHV. The tungsten filament was used to resistively heat the applicator at $T \approx$ 100 °C to outgas the material. The applicator was then carefully contacted to a freshly cleaned Au(111) substrate, which was subsequently annealed to 150 °C for 12 h to remove the pyrene matrix. The temperature was then slowly ramped to 350 °C to induce cyclodehydrogenation of the polymer forming the desired GNR. Although many locations on the substrate still contained amorphous carbon structures, certain domains were observed with a high concentration of pristine 9-AGNRs with relatively consistent length and the exact edge termination predicted by the structure of the initiator/terminator. The structure of the 9-AGNRs was confirmed with BRSTM (Figure 2.3K,L).

dI/dV point spectroscopy and differential conductance mapping were performed on the resultant 9-AGNRs, shown in Figure 2.4. Point spectra acquired at the bulk armchair edge of the GNR revealed four distinct features centered at V_S = –1.5 V (peak 1), -250 mV (peak 3), 1.1 V (peak 4), and 1.5 V (peak 5). Peaks 3 and 4 are consistent with previous reports for the VB and CB, respectively, observed in 9-AGNRs grown from on-surface polymerization. Spectra collected at both ends of the GNRs, however, revealed an additional peak centered at V_S = -900 mV which was not observed in previous experiments. Differential conductance maps acquired at V_S corresponding to peaks 1, 4, and 5 display bright features along the armchair edge. Maps collected at V_S = –250 mV and 300 mV corresponding to peak 3 are saturated by the Au(111) surface state but some LDOS localization is observed along the armchair edge. Maps collected at V_S = –900 mV corresponding to peak 2 displayed bright lobes localized at the terminating edges

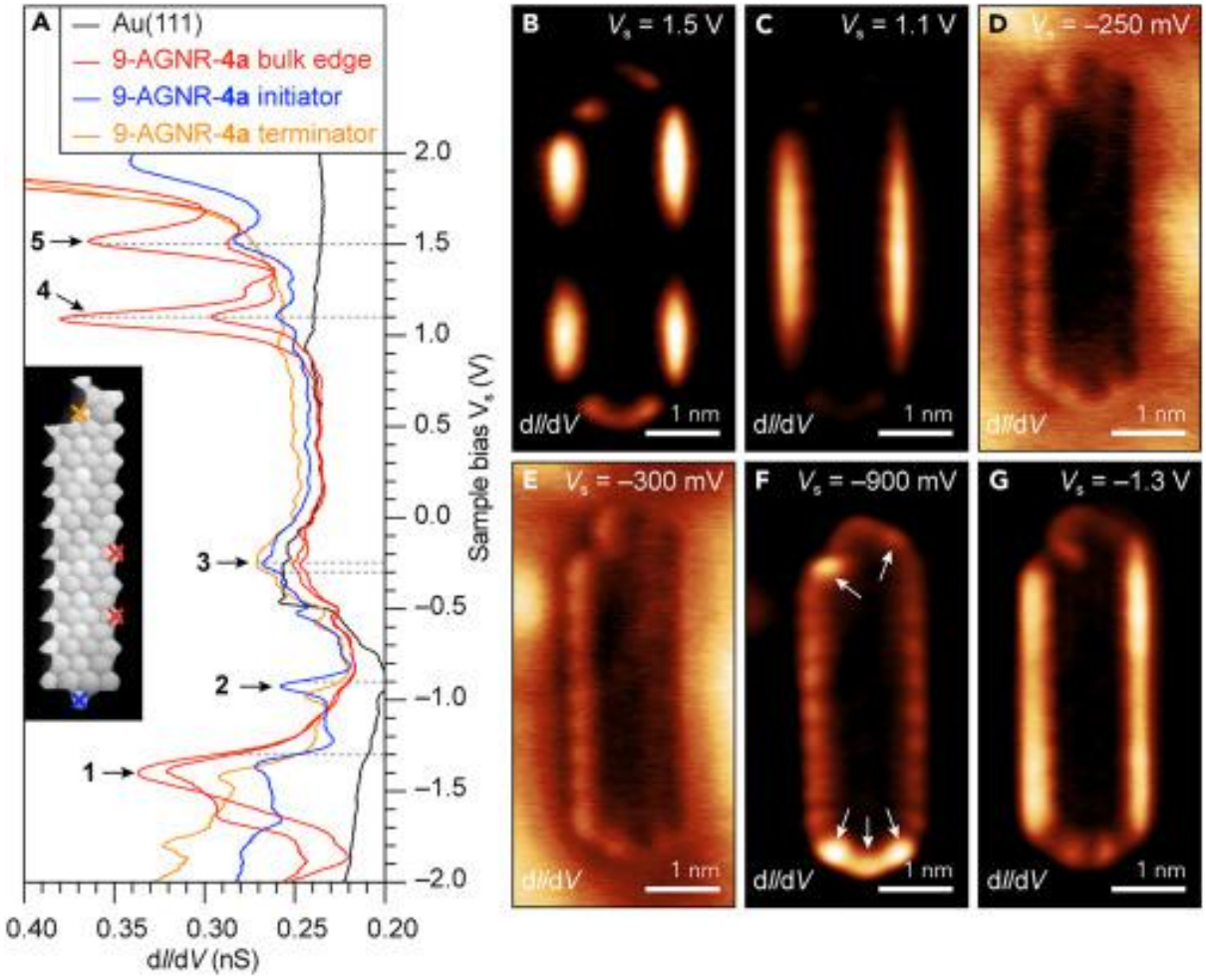

Figure 2.4 (A) d*I*/d*V* point spectra of 9-AGNRs formed from **poly-4a** performed at locations indicated on the BRSTM inset (V_M = 10 mV). **(B–G)** Differential conductance maps recorded at V_s corresponding to highlighted peaks in **A**.

of the GNR. We associate peak 2 with broadening of the VB due to the end structure rather than localized end-states.

2.4 Solvent aerosol deposition

Solvent aerosol deposition (SAD) is a deposition technique that involves aerosolizing a dilute solution or dispersion of the target material in a solvent and directing the droplets towards a substrate (Figure 2.5A). Ideally, the aerosolized droplets can be produced at fine enough scales such that they contain a single isolated nanomaterial or polymer, and the solvent is volatile enough that it evaporates almost instantaneously upon reaching the surface which prevents aggregation of the isolated material.[103–105] This contrasts with conventional drop-casting methods, where the concentration of target material builds up at the surface of the droplet as it

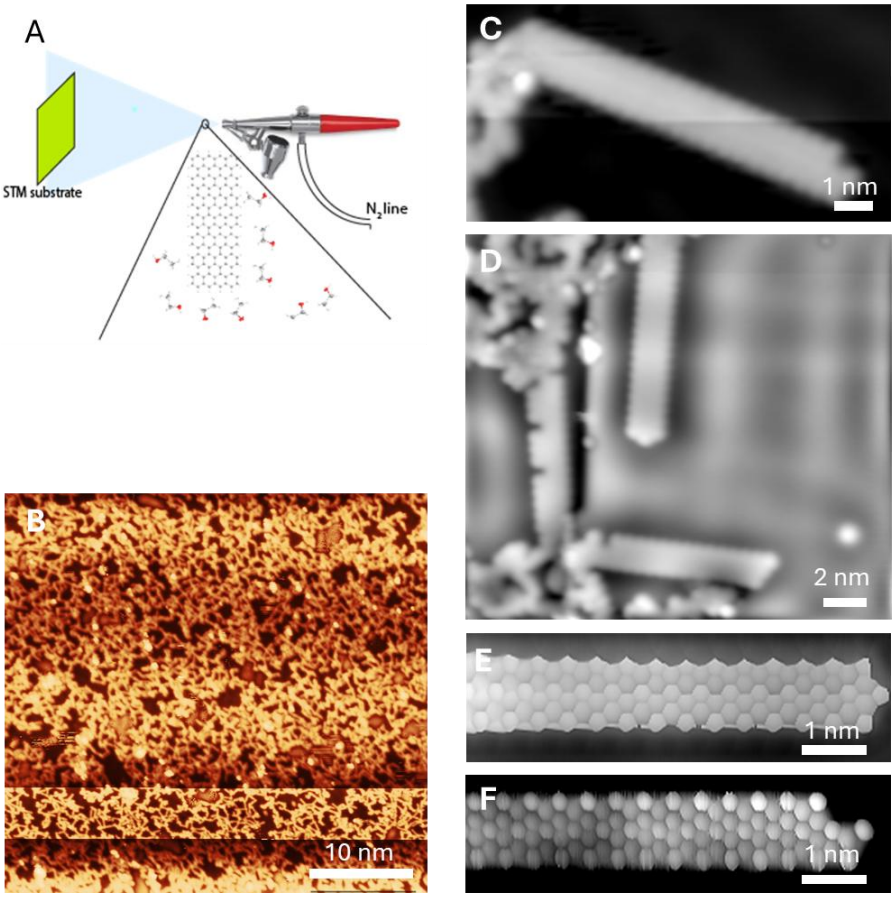

Figure 2.5 (A) Diagram of SAD process, where a dispersion of a nanomaterial or solution of polymer is aerosolized onto a substrate. **(B)** STM topographic image of solution-cyclized **poly-4b** deposited on Au(111) using SAD. **(C,D)** STM topographic images of **poly-4a** deposited on Au(111) with SAD following surface-catalyzed cyclodehydrogenation (V_s = 200 mV, I = 20 pA). **(E,F)** Constant-height BRSTM images of **poly-4a** deposited on Au(111) with SAD following surface-catalyzed cyclodehydrogenation showing an example of each predicted end structure (V_s = 10 mV, V_M = 10 mV).

evaporates, leading to aggregation at the boundaries which is known as the “coffee-stain” effect.[106,107]

SAD has previously been employed to isolate 1D nanomaterials such as carbon nanotubes (CNTs) on substrates for characterization with ambient atomic force microscopy. This can be achieved with very volatile solvents such as dichloro-ethane and results in remarkably clean surfaces with isolated CNTs and very little aggregation. These results inspired efforts to investigate whether this method could be extended to transfer solution-synthesized GNRs or polymer precursors onto catalytic Au(111) substrates for STM characterization in UHV. Although previous experiments have used MAD transfer to successfully transfer isolated 9-AGNR polymer

precursors,[43] the technique has two main drawbacks. First, stamping a macroscopic amount of matrix/material on the substrate results in highly inconsistent surface coverage depending on the distance from the stamp location. Even for optimized MAD samples, only very specific domains host the correct environment for the proper cyclodehydrogenation of isolated polymer precursors, and locating/identifying these domains can be extremely time-consuming. Second, while pyrene is volatile enough to be removed from Au(111) substrates by annealing to 150 °C, it tends to build up in the chamber leading to eventual contamination that is difficult to remove. SAD could provide solutions to both problems, as the level of surface coverage should be consistent across domains similar in size to the aerosol droplets rather than varying across the entire substrate, and volatile solvents should be significantly easier to remove than the pyrene matrix.

We attempted to deposit **poly-4b**, which contains aryl solubilizing groups, as well as the material obtained from the Scholl reaction performed on **poly-4b**, using SAD. **Poly-4b** was dissolved in ethanol at a concentration less than 1mg/L, while the graphitized Scholl product was sonicated in DCM following which the solution was centrifuged and the supernatant containing a dilute dispersion of the material was collected. A clean Au(111) substrate was removed from the chamber briefly following which a precision airbrush gun was used to aerosolize the respective solutions onto the substrate. The substrate was then returned to UHV and annealed to 120 °C to remove residual solvent or water, and for the **poly-4a** sample the temperature was then slowly ramped to 300 °C to induce cyclodehydrogenation. Results for the solution-cyclized poly-**4b** sample experiments were similar to those obtained using MAD,[43] and only amorphous carbon networks were observed on the surface (Figure 2.5B). Attempts to deposit **poly-4a** to the surface and form desired 9-AGNRs were slightly more successful. While a large amount of amorphous carbon was observed, some 9-AGNRs featuring the desired edge termination were observed, often extending out of the amorphous carbon domains (Figure 2.5C,D). Their structure was confirmed with BRSTM (Figure 2.5E,F).

While SAD still resulted in a large amount of undesired interpolymer crosslinking, the observation of some pristine GNR segments, although not fully isolated, are encouraging. These amorphous carbon domains are never absent even in successful MAD experiments. We infer that SAD of these polymers could be further optimized using more sophisticated aerosol techniques such as electrospray ionization (ESI) to produce more isolated pristine GNRs.[103,108,109]

2.5 Phosphorene nanoribbons

Phosphorene nanoribbons (PNRs) are 1D nanostructures analogous to GNRs derived from black phosphorous, a layered material composed of 2D sheets of covalently bound phosphorous atoms analogous to graphite.[110–112] PNRs can be fabricated through a relatively simple top-down process which involves the ion scissoring of phosphorene sheets from black phosphorous crystals[113] along the zigzag edge of the phosphorene, producing micron-scale nanostructures with high aspect ratios (widths as low as 5 nm).[114] Evidence suggests that the resulting PNRs bulk edge exclusively features the zigzag orientation (Figure 2.6A), resulting in predicted

emergent magnetic behavior similar to that of ZGNRs.[115] The fabrication process involves two steps. The black phosphorous is first intercalated with lithium ions to weaken in the interlayer attraction. The material is then sonicated in a solvent – dimethylformamide (DMF) or N-methyl-2-pyrrolidone (NMP) – to form stable dispersions of isolated PNRs.[114]

The predicted edge magnetism in PNRs and the apparent prominence of zigzag edges produced from this top-down fabrication procedure has prompted investigation into the magnetic properties of the material. PNRs in solution are predicted to feature 100-fold increased magnetic susceptibility, χ, with respect to bulk black phosphorous (Figure 2.6C). Magnetic linear birefringence performed on PNR solutions indicates saturation of the orientational anisotropy under much milder conditions (weaker magnetic fields, room temperature) than other

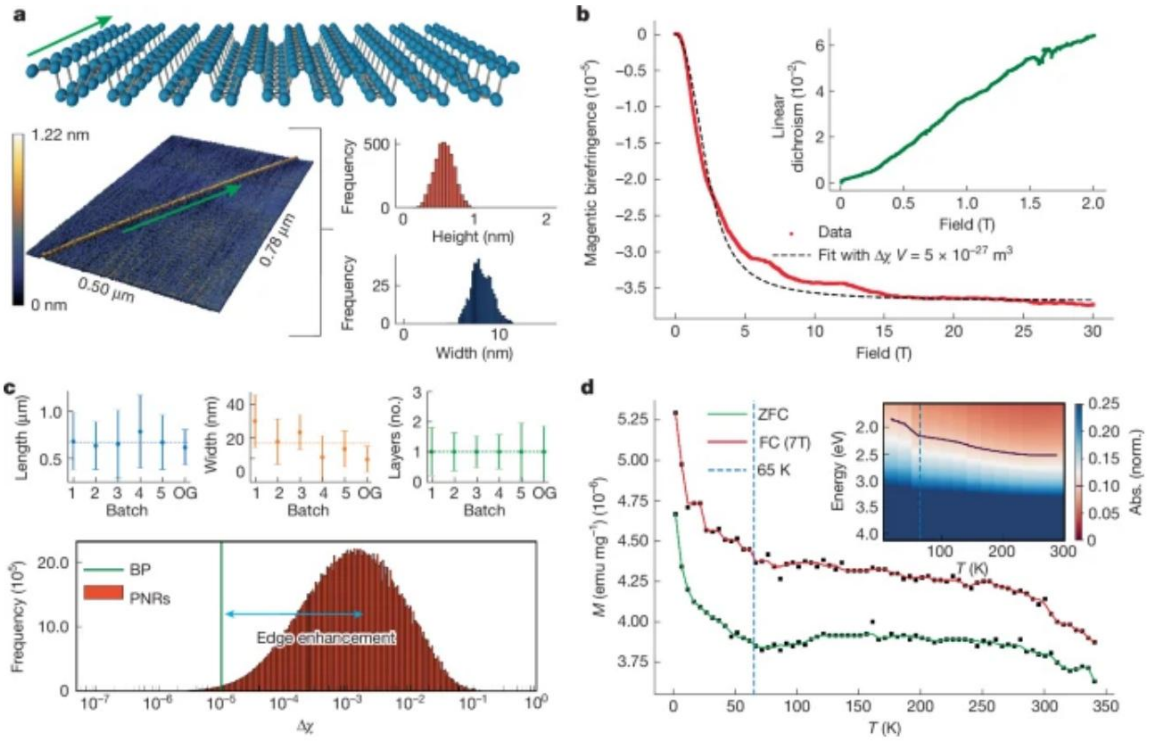

Figure 2.6 (A) Top, 3D structures of PNRs featuring zigzag edges. Bottom, AFM image and histogram of height and width for a representative PNR. **(B)** Magnetic linear birefringence data shows alignment of PNRs with respect to external fields. Inset, linear dichroism signal increases with external magnetic field, indicating orientational anisotropy of PNRs. **(C)** Bottom, histogram of anisotropy and calculated magnetic susceptibility χ from all possible PNR volumes, derived from transmission electron microscopy and AFM data. **(D)** SQUID measurements showing field cooled (FC) and zero field cooled (ZFC) magnetization (M) at varying temperatures.

nanomaterials (Figure 2.6B). This orientational alignment is corroborated by increased linear dichroism signal with increasing fields, with the light polarized parallel to the magnetic field (inset, Figure 2.6B). Results from superconducting quantum interference device (SQUID) magnetometry measurements show non-Curie behavior even above room temperature indicated by the offset of the 7T field-cooled (FC) and zero field-cooled (ZFC) magnetizations. Additionally, signatures of a magnetic phase transition were observed near 65 K (Figure 2.6D).[112]

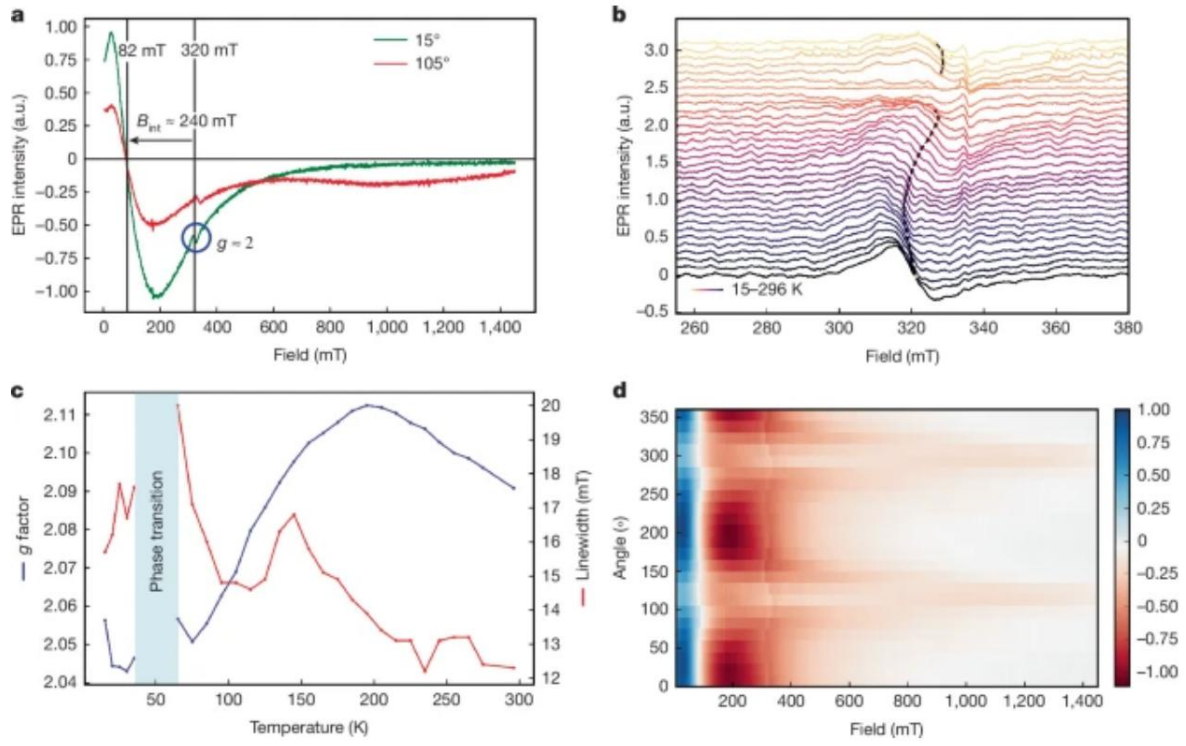

Figure 2.7 (A) cwEPR signal of PNR films, displaying EPR signal at 320 mT and a large FMR signal at 82 mT. **(B)** Line cuts of the EPR signal at varying temperatures. Dashed black line indicates the zero-intensity crossing. **(C)** Extracted g factor and line width at varying temperatures. Divergence in line-width near 50 K indicates a magnetic phase transition. **(D)** Dependence of EPR signal intensity on rotation angle of EPR tube.

Continuous wave electron paramagnetic resonance spectroscopy (cwEPR) was also performed on PNR thin films, revealing an EPR signal well as an intense ferromagnetic resonance (FMR) signal (Figure 2.7A). The EPR signal vanishes near 50 K corresponding to divergence of the linewidth, indicating the presence of a magnetic phase transition at a similar temperature to that observed in SQUID measurements (Figure 2.7C).[112]

These results provide insight for the magnetic behavior of PNRs. Scanning tunneling microscopy presents an ideal opportunity to confirm the zigzag edge structure and corroborate the evidence for edge-enhanced magnetism, potentially elucidating the width dependence of this behavior by probing individual PNRs.

Initial experiments were performed with ambient atomic force microscopy (AFM) to optimize the conditions for depositing PNRs on substrates using SAD. The PNR dispersion in NMP or DMF was first diluted by approximately 100:1 with the corresponding solvent. The resulting dilute dispersion was then aerosolized onto a freshly cleaved HOPG substrate using a precision airbrush gun. DMF and NMP are highly volatile solvents, so the length and number of pulses with the aerosol gun was limited to prevent condensation of solvent droplets. AFM imaging readily revealed isolated PNRs at relatively consistent surface coverage with very little sign of aggregation or surface contamination (see Figure S4), much more promising for possible UHV STM characterization than results obtained by drop-casting the PNR dispersion. Better results were obtained from PNRs dispersed in NMP than DMF.

We then attempted to prepare samples for UHV STM characterization by using SAD to deposit dilute PNR dispersions on Au(111) substrates. STM images revealed an unresolvable multilayer film coating the substrate which could not be removed with thermal annealing. This occurred with both NMP and DMF dispersions of PNRs and control experiments indicated that the contamination originates from the solvent. However, the same control experiment performed on HOPG yielded much cleaner surfaces. The source of the contamination is unknown but we proceeded with experiments on HOPG.

Samples were then prepared by aerosolizing dilute PNR dispersions onto freshly cleaved HOPG, following which they were transferred to UHV and annealed to 150 °C to remove most of the solvent molecules. Samples were not annealed to higher temperatures to prevent thermal degradation of the PNRs. The substrate was then characterized with STM.

Locating PNRs on the surface using STM proved challenging due to the limited range of the *xy*-piezo stage of the STM head when compared to ambient AMF and the low density of PNRs on the surface. Furthermore, the STM probe is very sensitive to residual solvent molecules and surfactants used in the PNR synthesis. Since imaging quality quickly degrades while scanning on PNR samples, frequent tip preparation had to be performed on a separate clean Au(111) substrate. Features with dimensions commensurate with PNRs were encountered on the surface, yet it remained ambiguous whether these were PNRs which had been deposited onto the surface or could be attributed to grain boundaries/defects in the HOPG. A low signal to noise ratio and broadening of the features when reducing the scan area can be attributed to the collection of surfactant molecules on the tip. Large clusters were occasionally observed as illustrated in Figure 2.8A. Occasionally longer straighter features were observed which may have been few-layer (Figure 2.8B) or single layer (Figure 2.8C) PNRs averaging roughly 0.5–0.7 nm in height. Atomically resolved imaging with CO functionalized STM tips on or along the edges of these structures was unsuccessful (Figure 2.8D).

Structural and electronic characterization of PNRs using STM remains an unresolved challenge. The solvents used in the fabrication process prove to be very difficult to fully remove and tend to introduce contamination and interfere with measurements.

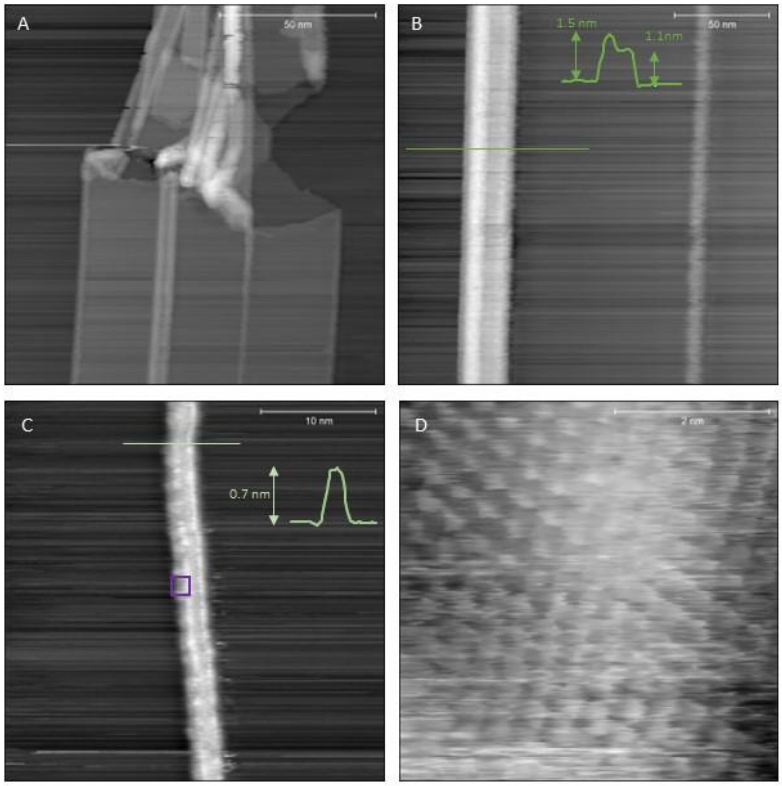

Figure 2.8 (A) STM image of a PNR cluster accumulated on a HOPG step edge. **(B,C)** STM images of suspected few-layer and single layer PNRs, with line profiles corresponding to the cross sections shown in the image. **(D)** Close-up STM image of the area in the blue box in C (V_s = 500 mV, I_t = 20 pA). All STM experiments were performed at T = 4.2 K.

2.6 Outlook

Solution-based synthesis techniques and wet top-down nanomaterial fabrication procedures (such as PNR fabrication process) have the potential to drastically expand our repertoire of exotic nanomaterials and could lead to previously inaccessible phases in such materials. However, the discrete isolation and structural characterization of individual nanomaterials remain a difficult challenge. Employment of more sophisticated techniques such as electrospray ionization deposition could possibly provide better results.

Chapter 3 – Novel Van der Waals heterostructures leveraging molecular templating

Van der Waals heterostructures composed of layered 2D materials have become a major topic of research in materials science over the past two decades. These heterostructures are composed of deliberately stacked 2D monolayers which are bound together by weak interlayer interactions.[47,48] By tuning the twist angle between layers, combining different materials with lattice-mismatch, or intercalating metal atoms, periodic strain can be induced in the layered materials, forming Moiré mini-bands which can induce strongly correlated electronic phenomena.[116,117] The most ubiquitous example is twisted bilayer graphene (TBG), which can exhibit states with high effective carrier mass near the Fermi energy, creating the ideal environment for the formation of strongly correlated electronic phases and resulting in emergent phenomena such as superconductivity at particular interlayer twist angles (Figure 3.1B,C,E).[8,10,49,118–120]

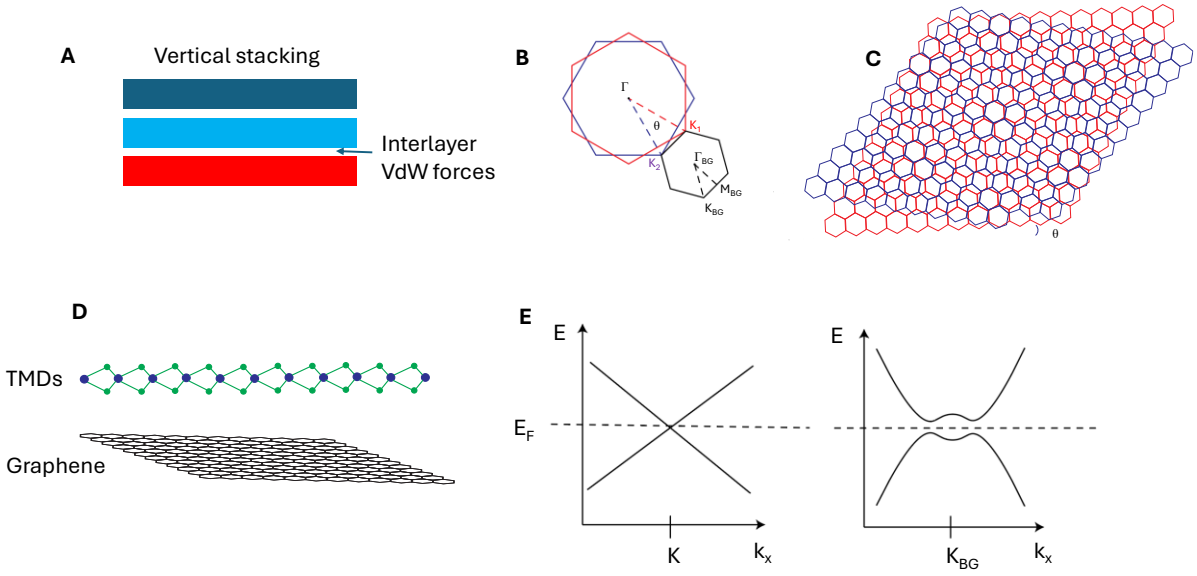

Figure 3.1 (A) Schematic of vertical stacking of layered materials to produce Van der Waals heterostructures. **(B)** First Brillouin zone for to layers of monolayer graphene at a relative twist angle θ showing the resulting Brillouin zone for twisted bilayer graphene. **(C)** Example of Moiré pattern in twisted bilayer graphene at representative angle θ. **(D)** Top, cross-sectional sketch of representative monolayer TMD. Bottom, sketch of monolayer graphene. **(E)** Left, sketch of band structure of monolayer graphene around the K-point. Right, sketch of representative twisted bilayer graphene band structure where a quasiparticle gap emerges.

While the realization of such phenomena and integration of host materials into device architectures remains highly desirable, several constraints limit its progress. First, there is a narrow field of bulk layered materials with optimal properties, e.g. lattice symmetry, metallicity, high carrier mass, etc. from which to choose. Transition metal dichalcogenides (TMDs, Figure 3.1D), host an attractive variety of properties including intrinsic exotic phenomena such as superconductivity.[121] Second, the fabrication of certain heterostructures remains highly specialized and unscalable, such as TBG, requiring a very complex exfoliation procedure involving very precise micrometers.[47] Third, the energy scale at which these phenomena break down is very low for conventional heterostructure architectures, i.e. the critical temperature for the phase transition is often well below the standard liquid helium cryostat at 4K, requiring very expensive and high-maintenance dilution refrigeration systems to achieve the temperatures necessary to observe them.[50]

One strategy to overcome the first two challenges is to exploit molecular templating to modify the electronic structure of monolayer 2D materials by inducing periodic strain in the system (Figure 3.2). This strategy has several advantages. For example, while 2D nanomaterials grown from molecular precursors tend to suffer from limited and defective growth resulting in patches no larger than 10–20 nm, molecular self-assemblies which rely on weak intermolecular interactions to form a periodic lattice can be easily grown at much larger scales. This could drastically simplify fabrication of layered heterostructure by using the molecular film as a global layer. Another advantage is that there are several motifs which can be used to induce self-assembly such as hydrogen bonding and π-π interactions. This allows for a wide range of molecular candidates which not only have a variety of symmetries but can also have attractive intrinsic properties such as magnetism or Coulombic charge that can be leveraged. While these molecular films have limited bulk properties due to very weak electron interactions in the absence of covalent bonds between lattice sites, they present a promising strategy to tune the

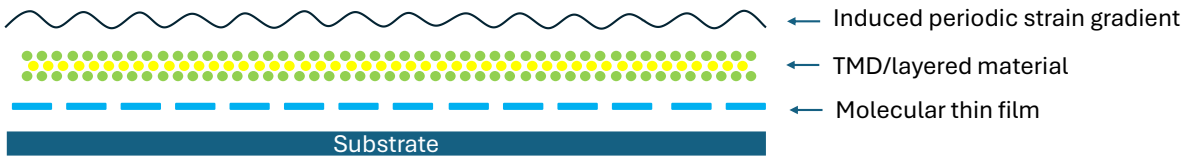

Figure 3.2 Illustration of heterostructure architecture leveraging molecular templating.

electronic structure of inherently more interesting materials such as metallic TMDs. Moreover, some magnetic molecules can interact through magnetic exchange facilitated by a metallic substrate, for example iron(II)-pthalocyanine (FePc) and manganese(II)-pthalocyanine (MnPc) forming an antiferromagnetic ground state mediated by the RKKY interaction.[64] The analogous interaction of these magnetic molecules through a metallic monolayer in the proposed heterostructure could enhance the hybridization between the layers and potentially induce exotic electronic phenomena.

There are some unique challenges in employing this approach to fabricate Van der Waals heterostructures which will be discussed later in this chapter. Notably, the molecular thin films tend to decompose or sublime from the surface upon high temperature annealing, which is a ubiquitous step in the preparation and exfoliation of bulk layered materials to monolayer for STM characterization.

In this chapter I will detail this molecular templating strategy and the attempted fabrication of the inverted heterostructure architecture. I will begin by discussing the selection of molecular thin films, including two candidates which form, respectively, a 2D Kondo lattice and a 2D Coulomb charge crystal. I will then discuss the selection of layered materials, properties of monolayer TMDs, and the in-vacuum transfer technique used to exfoliate monolayer flakes. Finally, I will cover the fabrication attempts of the heterostructures, both inverted and conventional.

3.1 Molecular thin films

In this section I will detail the growth and characterization of two types of molecular thin films. The first is composed of trioxatriangulenium (TOTA) molecules (structure shown in Figure 3.3B) which can host a non-zero charge on the central carbon. I will show that tuning the surface coverage of charged molecules can access a regime where they become equally spaced into a hexagonal lattice-like periodic system even in the absence of an attractive force driving molecular self-assembly. In this regime the film can be considered as a 2D Coulomb lattice, which is attractive for our molecular templating strategy. TOTA derivatives are also promising for incorporation into gated graphene-based devices wherein electron doping could populate the LUMO and neutralize the charge on the molecule,[122] allowing a reversible switch between a self-assembled molecular thin film and the 2D Coulomb lattice.

The second molecular film I will discuss is composed of phthalocyanine (Pc) metal organic complexes, which may contain metal centers that can host a range of magnetic moments. The self-assembly is driven by dipole-dipole interactions between molecules which are functionalized with fluorine (see Figure 3.5). The resulting thin film is a molecular Kondo lattice which has been shown to have a magnetic ground state mediated by the Ruderman Kittel Kasuya Yosida (RKKY interaction)[123] for certain metal centers.[64] These properties also make these films attractive for our molecular templating strategy, as the Kondo lattice forms an effective flat band at the zero energy which can be easily hybridized with metallic bands in 2D materials. This has been demonstrated in TMD heterostructures where intrinsic coinciding charge and spin density waves (CDW, SDW) in one layer form a Kondo lattice when hybridized with a metallic layer, causing a hybridization gap-opening associated with the formation of heavy fermions (see Figure 3.8).[50]

3.1.1 TOTA

TOTA is a planar polycyclic aromatic hydrocarbon which can host a stable carbocation on the central carbon. This position can also be easily functionalized and attached to another small

molecule, which allows the TOTA to act as a functional platform molecule. Previous studies on these neutral functionalized TOTA molecules have leveraged the relatively strong physisorption of the TOTA base to a metallic substrate to decouple a small molecule from the surface and from its neighbors while freezing its location.[124] This architecture can be used to create a film of molecular rotors or similar nanomachines. For example, by attaching a phenyl-based molecule with a strong dipole to the TOTA core, a molecular thin film can be fabricated in which freely rotating dipoles are evenly spaced and too far apart to interact with one another, allowing their orientation to be easily manipulated by an electric field. STM studies have been conducted investigating the survival of the central bond with varying functional groups/molecules on metallic substrates and found that larger functional groups, despite having lower bond dissociation energies, survive better than smaller groups such as hydrogen or methane.[125]

Another application of these molecular thin films involves their incorporation into devices wherein a gate voltage can be used to populate the LUMO,[122] neutralizing the charge and inducing switchable self-assembly of the molecules via dipole interactions. The energy of the LUMO can be tuned via functionalization of the TOTA edges. Electron withdrawing groups such as NO_2 are predicted to lower the energy of the LUMO, bringing it closer to the Fermi energy and making it easier to populate via electron doping. In this section I will detail the electronic characterization of $TOTA^+$ and methyl-$TOTA^+$ to show the effect of electron donating groups to the LUMO. Other $TOTA^+$ derivatives with strong electron withdrawing groups have yet to be characterized.

Finally, I will show that by tuning the surface concentration of the cationic $TOTA^+$, a quasi-periodic 2D Coulomb crystal can be achieved at sub-monolayer coverage, which is exciting inherently and as a candidate for a 2D molecular template. Notably, CDWs exist in many 2D materials which host strongly correlated phenomena, and templating with a charged lattice defined by molecular interactions could open a new door for exciting heterostructure fabrication.

Sub-monolayer thin films of methyl-$TOTA^+$ (see Figure S5 for structure and STM results) were grown on an Au(111) surface by subliming methyl-$TOTA^+BF_4^-$ in its crystalline form using a K-cell type evaporator. The sublimation temperature of the salt was 160 °C. At low surface concentrations, a high proportion of defective, asymmetric molecules was observed without thermal annealing of the substrate. Possible causes include impurities in the material or decomposition of the desired product either during sublimation or catalyzed by the gold substrate. The anion BF_4^- was never observed on the surface. Some molecules which retained three-fold symmetry (presumably methyl-TOTA) were observed and characterized with STS. d*I*/d*V* spectroscopy at the molecular center revealed a single large peak within 2eV from E_F at 1.1 V associated with the LUMO. When collecting d*I*/d*V* spectroscopy at the corner of the molecule, a sharp increase in tunneling current occurred at 1.2 V, indicative of a spontaneous change in either the tip or the sample. When the molecule was imaged again it had moved and no longer appeared to have C_3 symmetry. Subsequently collecting d*I*/d*V* spectra at the center again revealed that the LUMO peak at 1.1 V had vanished. We believe this dramatic tunneling

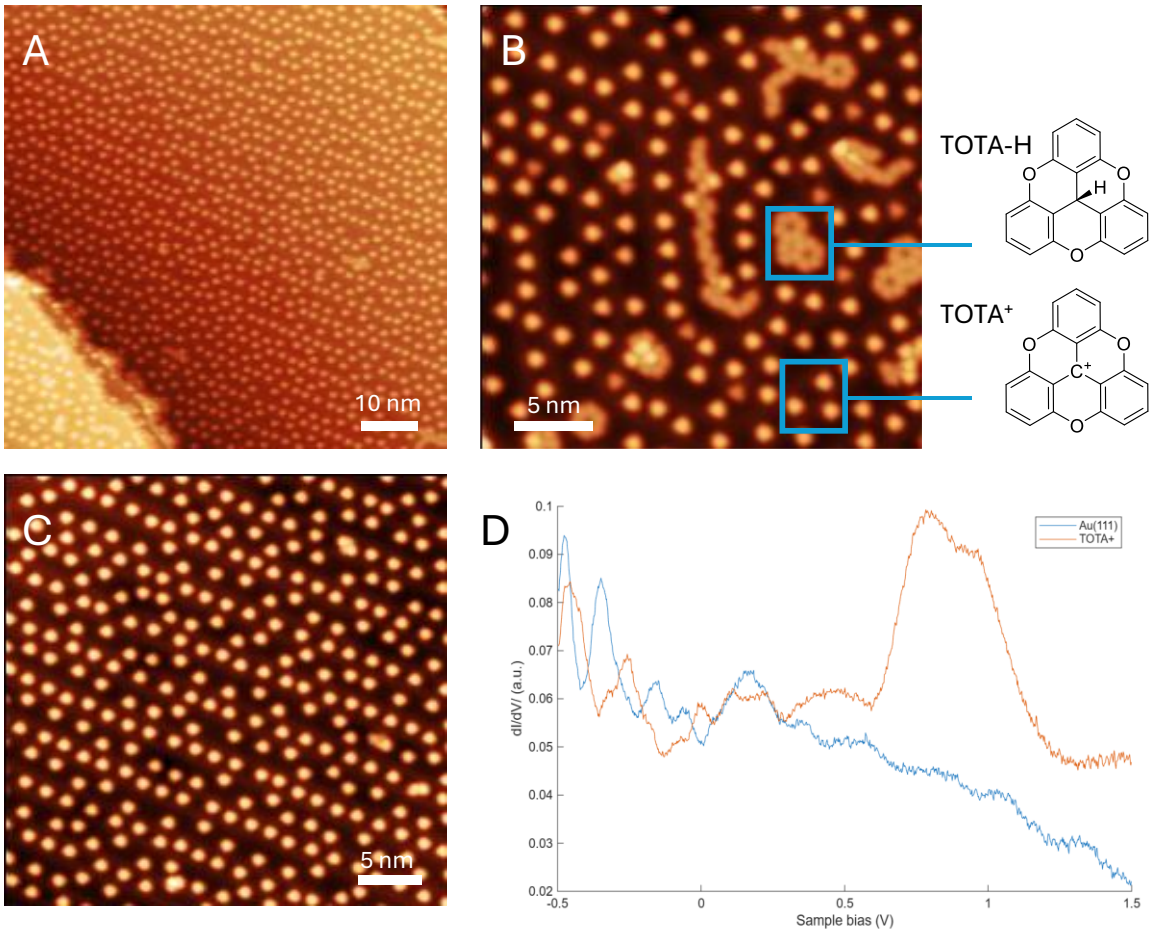

Figure 3.3 Images and d*I*/d*V* spectroscopy of $TOTA^+$ deposited on Au(111) as TOTA-H. **(A–C)** Topographic images of TOTA thin films. Structures of $TOTA^+$ and TOTA-H are shown in **B** where both species are identified in the topographic image. The neutral TOTA-H forms a hexagonal self-assembly pattern while the $TOTA^+$ molecules appear repel one another/ **(D)** d*I*/d*V* spectroscopy of $TOTA^+$ collected at the center of the molecule, showing a large peak around 800 mV corresponding the LUMO of $TOTA^+$, and Au(111) background.

current change is associated with a dehydrogenation at the methyl position, allowing the π-electrons to rearrange and neutralize the charge in the molecule and causing the disappearance of the LUMO peak.

$TOTA^+$ was deposited on Au(111) by subliming the salt $TOTA^+BF_4^-$ at 165 °C. All deposition attempts for $TOTA^+$ from the salt form resulted in very low coverage films, with most of the deposited molecules adhering to the gold step edges. Increasing the deposition temperature or time significantly resulted in contamination of the sample from decomposition products or other impurities which we were unable to remove. High coverage films were grown by subliming the molecule in its neutral, hydrogenated form TOTA-H. Previous reports have

indicated that TOTA-H can be sublimed in UHV as low as 70 °C and that upon deposition on Au(111) very few molecules retain their neutral form with most of them losing the hydrogen and forming the charged species $TOTA^+$.[125] The two species can easily be distinguished via STM because the neutral TOTA-H self assembles in a hexagonal packing structure while the $TOTA^+$ spreads out around the gold surface (Figure 3.4 B). The $TOTA^+$ molecules appear to repel each other indicating that if any charge transfer occurs, it is only partial and does not fully neutralize the charge on the molecule. TOTA-H was sublimed at 120 °C onto Au(111), resulting in high coverage sub-monolayer molecular films which were characterized with STM (Figure 3.4A,B). Consistent with previous reports, only a small amount of self-assembly occurred, indicating that most of the molecules formed $TOTA^+$ on the surface. Upon annealing the substrate to 100 °C, we observed that 100% of the molecules had converted to the charged species (Figure 3.4C). This complete conversion with such minimal substrate annealing indicates that the dehydrogenation occurs on and is catalyzed by the gold substrate. This is consistent with reports showing that molecular derivatives with larger substituents on the central carbon are less likely to decompose to $TOTA^+$ than counterparts with smaller substituents, although the relative bond dissociation energies are higher.

Differential conductance point spectroscopy was performed on $TOTA^+$ revealing a large peak at 900 mV associated with the LUMO (Figure 3.4D). No surface reaction was observed when collecting point spectroscopy at the corners as with the methyl-$TOTA^+$. The relative LUMO energies of $TOTA^+$ and methyl-$TOTA^+$ are consistent with gas phase calculations, which also predict that substitution with electron withdrawing groups such as NO_2 or CN at the corners would lower the LUMO energy considerably. These molecules could be incorporated into a device wherein the LUMO, if close enough to the Fermi energy, could be easily populated with a positive gate voltage, allowing observation of spontaneous neutralization and re-assembly of the molecules on the device. This would open a door to a new class of molecular based nanomachines, which could be used for a wide variety of applications. NO_2-$TOTA^+$ has been synthesized and is being characterized by our device-integrated STM collaborators.

As discussed previously, TOTA is also useful as a platform molecule, which can be functionalized at the central carbon to decouple another small molecule from the surface, while defining its position by the self-assembly of the TOTA platform.[124] By functionalizing the platform with a freely rotating molecule with a strong molecular dipole, this architecture could be used to build an array of nano-rotors wherein the orientation of the rotating molecule can be easily controlled by an in-plane electric field. TOTA functionalized with 4-methoxybenzonitrile on the central carbon was synthesized and several attempts were made to grow thin films of the molecule on Au(111). However, only self-assembled chains inconsistent with the shape, symmetry, or structure of the target molecule were observed on the surface. It is uncertain whether these formations result from a sample impurity or some decomposition product that forms during sublimation.

While unanalogous to highly unstable ion trap Coulomb crystals made possible only by laser cooling,[126] a periodic 2D lattice of molecular charges, which we will deem a 2D molecular

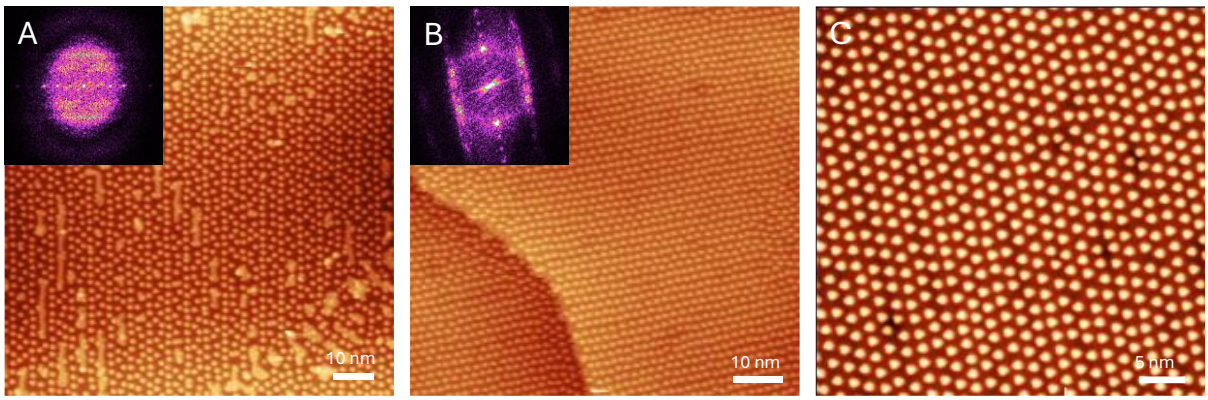

Figure 3.4 Topographic images of high density TOTA thin films. **(A)** Topographic image of TOTA thin film as deposited from TOTA-H. The majority of molecules have converted to $TOTA^+$. Inset shows the 2D FFT of the image, showing some small peaks corresponding to molecules adhering to herringbone reconstruction in Au(111). **(B)** Topographic image of TOTA thin film after annealing to 100 °C, inducing complete conversion to $TOTA^+$. Inset shows the 2D FFT of the image, showing hexagonal peaks which indicate the emergence of periodicity in the thin film. **(C)** Close-up image of the same thin film shown in **B**.

Coulomb crystal, could be a very exciting template for heterostructure fabrication. $TOTA^+$ is the perfect molecular candidate given it is easy to sublime as TOTA-H and readily converts to $TOTA^+$ on Au(111). The mild deposition conditions allow for very precise tuning of the surface coverage. Coulomb repulsion between the molecules, although likely screened by interactions with the gold surface such as strong physisorption and partial charge transfer, will dominate and will be defined by equation 3.1[60] where ϵ_{eff} is the effective permittivity of the medium including the gold substrate, ignoring surface screening effects which may reduce $U(r)$. At high surface coverage, the molecules will arrange to minimize $U(r)$. At maximum surface coverage, this will result in a hexagonal molecular lattice in which the periodicity is defined by Coulomb repulsion between charged molecules rather than attractive intermolecular forces which induce self-assembly.

$$U(r) = \frac{e^2}{4\pi\epsilon_0\epsilon_{eff}r} \qquad \textbf{3.1}$$

2D fast Fourier transforms on images of medium-high concentration samples show no distinct peaks, indicating the coverage is too low to induce periodic order. As the surface concentration is slowly increased, each time annealing the substrate to 100 °C to induce full conversion to $TOTA^+$, peaks begin to emerge in the FFT (Figure 3.3B). This indicates that the threshold at which periodicity is induced defined by the minimization of $U(r)$ is being approached. While perfect periodicity was not achieved, the surface coverage could likely be pushed even further. Moreover, this demonstrates the possibility of using a molecule like TOTA to form a periodic charged system on the surface, resulting in a 2D molecular Coulomb crystal which could be used for molecular templating. The interplay between, for example, a charge density wave intrinsic to a 2D layered material and a substrate templated with periodic charges could be very interesting

and offer novel insight into the physics of these systems as CDWs are often associated with strongly correlated electronic phases.

3.1.2 Phthalocyanines

Phthalocyanines are a class of inorganic compounds composed of an aromatic macrocycle ligand and a metal center, commonly used as pigments and dyes and in applications such as OLEDs and photovoltaics. The ligand is an aromatic 18-π electron system with a –2 charge in its deprotonated state, and due to its planarity is optimal for studying on the surface.[127] A wide variety of metal centers can be exchanged at the core, and various STM studies have been conducted characterizing their electronic structures.[64]

These molecules do not tend to spontaneously assemble on the surface except for at very high surface concentrations. However, a dipole self-assembly motif can be induced by installing fluorine atoms on the edges of the ligand. If the molecules are partially fluorinated, they can interdigitate with each other and form a twisted square lattice (Figure 3.7). If the molecule is fully fluorinated, it will not self-assemble on its own because the dipoles will repel each other. However, it can form an alternating self-assembly with a non-fluorinated molecule (Figure 3.5). This allows for the formation of a checkerboard-like lattice with alternating metal centers at each position. These architectures are attractive because metal centers can be selected which contain d-orbitals with unpaired electrons such that the resulting thin film is a lattice of weakly-interacting or non-interacting spins. While the absence of covalent bonds between molecules makes it unlikely for conventional magnetic exchange interactions to occur between lattice sites, some films have been shown to be capable of forming an antiferromagnetic ground state on Au(111) mediated by the RKKY interaction.[64] In a system with periodic magnetic defects on a metal substrate such as this, the Kondo effect and RKKY interaction will compete to dominate the ground state. If the molecule is a low-spin system with $S = 1/2$, the conduction electrons in the substrate will completely screen the magnetic moment below the Kondo temperature and a magnetic ground state cannot be achieved. If, however, the molecular spin is high with $S > 1/2$, the Kondo effect will not fully screen the magnetic moment, and exchange between lattice sites can occur mediated by scattering of conduction electrons in the substrate (RKKY), resulting in a magnetic ground state. While they are competing interactions, the Kondo effect has been shown to coexist in RKKY dominated systems via the persistent presence of Kondo features in the dI/dV spectrum.[64] These molecular thin films in the presence of a metal are in essence a 2D molecular Kondo lattice with a magnetic ground state, making them very intriguing for the purpose of molecular templating.

Initial attempts to grow molecular thin films were performed with vanadium (IV) oxide-phthalocyanine and fully fluorinated copper (II) phthalocyanine (Figure 3.5). The two molecules were co-deposited sequentially after separately optimizing their deposition conditions. The deposition temperatures for VOPc and $CUF_{16}Pc$ were 260 °C and 275 °C, respectively.

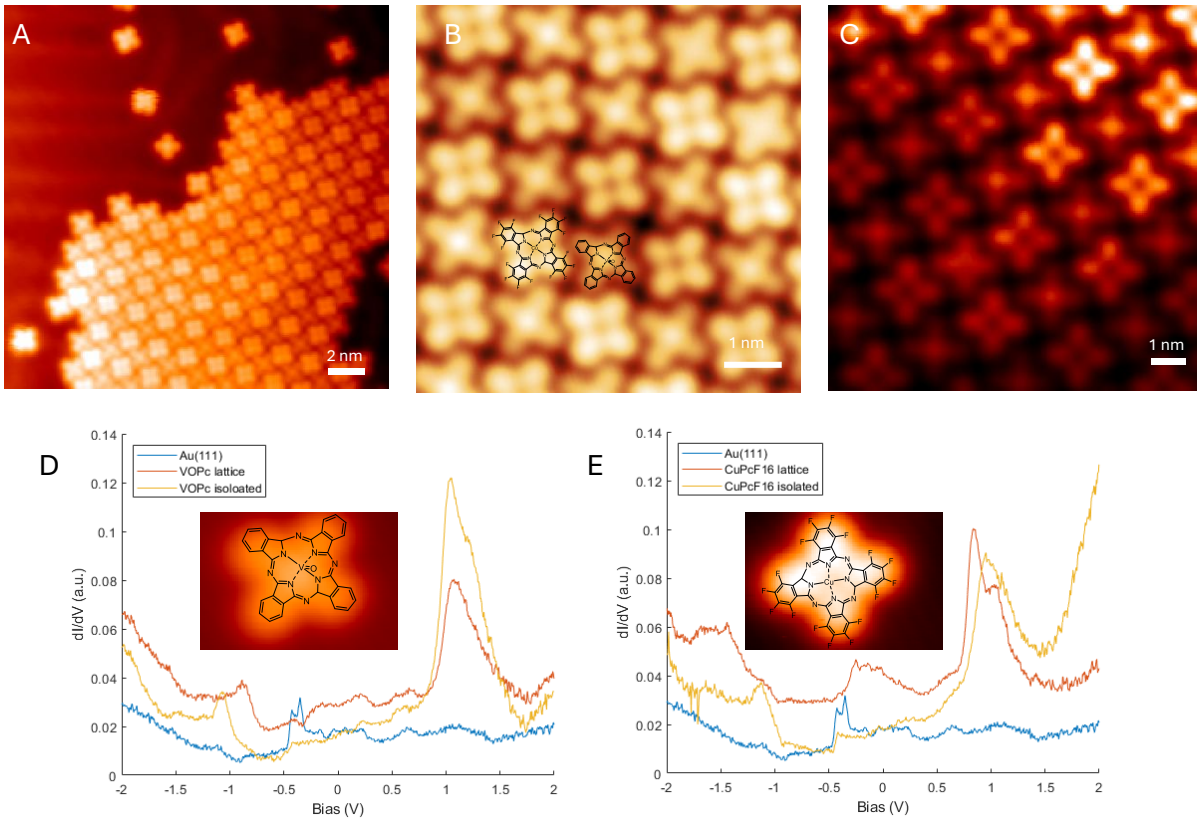

Figure 3.5 (A-C) STM topographic images of VOPc/$CuPcF_{16}$ thin films grown on Au(111). The structures are overlayed in **B** highlighting the self-assembly motif. **(D,E)** d*I*/d*V* point spectroscopy collected on VoPc, $CuPcF_{16}$ in the center of the molecule, comparing the spectrum collected on the isolated species with that collected on the same molecule within the thin film.

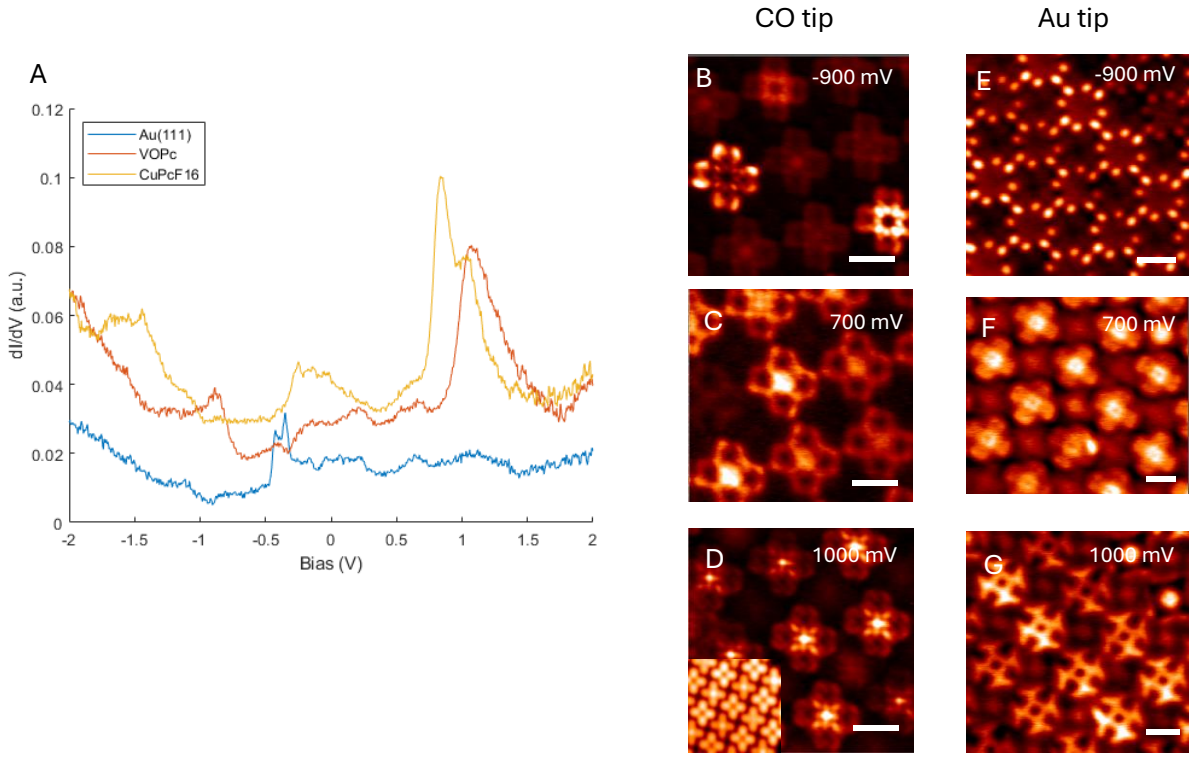

Figure 3.6 (A) d*I*/d*V* spectroscopy of VOPc/$CuPcF_{16}$ thin films, collected at the respective molecular centers, and Au(111) background. **(B-D)** d*I*/d*V* maps collected at the VOPc HOMO, the $CuPcF_{16}$ LUMO, and the VOPc LUMO, respectively, with a CO functionalized tip. Inset in **D** shows the corresponding topographic image for the set of dI/dV maps. **(E-G)** d*I*/d*V* maps collected at the VOPc HOMO, the $CuPcF_{16}$ LUMO, and the VOPc LUMO, respectively, with a metallic (*s*-wave) tip.

For every phthalocyanine on which deposition was attempted, a very large amount of a very regular impurity was observed on the surface for initial deposition attempts. To achievecomplete removal of the impurity, outgassing of the evaporator was performed at temperatures within 5 °C of the deposition temperature for several days.

Checkerboard-like lattices were achieved with VOPc and $CUF_{16}Pc$ by sequentially depositing the molecules at their respective deposition temperatures for 30 minutes. This resulted in a low surface concentration of self-assembled molecules, with patches varying from 10 – 30 nm in size. The molecules were characterized with d*I*/d*V* spectroscopy both while isolated from other molecules and in the self-assembled patches. The HOMO and LUMO peaks for both species are apparent in the spectra and show a small shift in energy between the isolated molecules and their self-assembled counterparts (Figure 3.5D,F). d*I*/d*V* maps were also collected at voltages associated with the HOMO and LUMO of the VOPc and the LUMO of the CuPc with both an s-wave (metallic) tip and a p-wave (CO functionalized) tip (Figure 3.6B-G). Notably, no Kondo feature was observed in the spectrum for either molecule although they are predicted to have spin $S = 1/2$. This could indicate that the Kondo temperature for this system is below 4K or that some unexpected charge transfer or interaction between the molecules and the gold substrate occurs.

We also attempted to grow these molecular lattices on bulk $NbSe_2$ as well as HOPG. On $NbSe_2$, although both molecular species were observed on the surface, self-assembly did not occur. On HOPG, the molecules were very mobile on the surface making it very difficult to obtain STM images (see Figure S6).

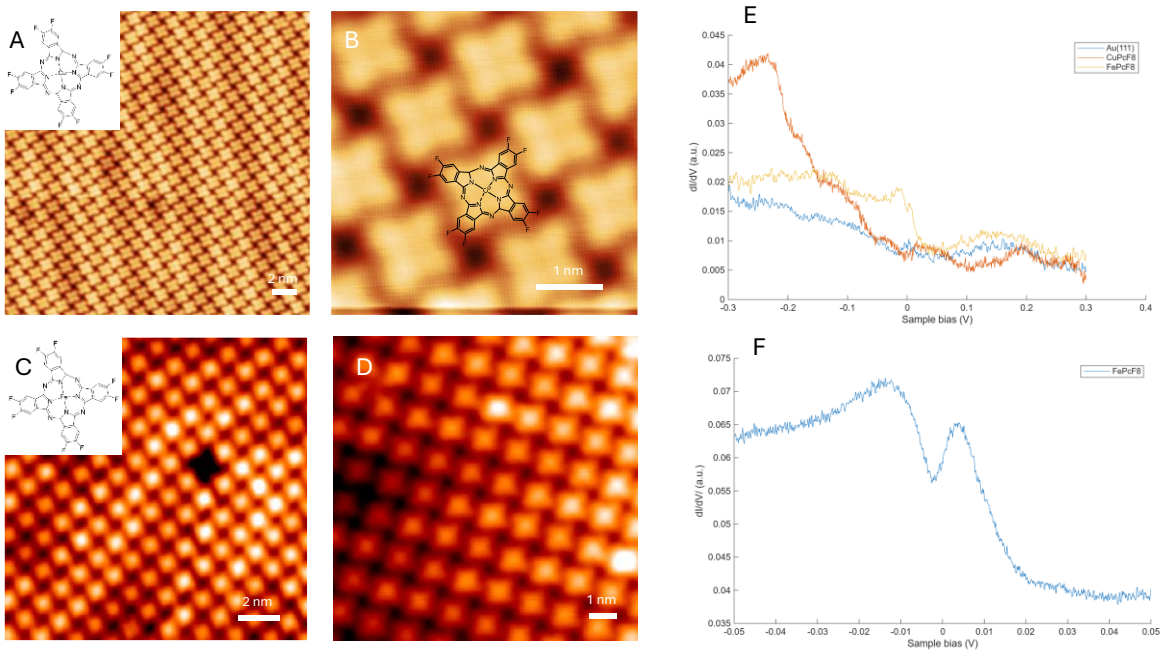

Figure 3.7 (A,B) Topographic images of $CuPcF_8$ thin films. Inset in **A** shows the structure of $CuPcF_8$, and the structure is included in **B** to illustrate the self-assembly motif. **(C,D)** Topographic images of $FePcF_8$ thin films. Inset in C shows the structure of $FePcF_8$. **(E)** d*I*/d*V* spectroscopy of $CuPcF_8$, $FePcF_8$ – collected at the center of the molecule – and Au(111) background. No zero-bias feature is observed in the $CuPcF_8$ spectrum, while an obvious shoulder appears in the $FePcF_8$ spectrum consistent with a Kondo feature. **(F)** d*I*/d*V* spectrum of $FePcF_8$, zoomed in at the zero-bias Kondo feature.

Thin films were also grown with $CuPcF_8$ (Figure 3.7A,B), which can self-assemble without an unflourinated counterpart, removing the requirement for a sequential co-deposition drastically simplifies the process. These films were also grown with an approximate evaporator temperature of 275 °C, very similar to the $CuPcF_{16}$. Very large patches of $CuPcF_8$ were grown on Au(111) up to 100 nm. The d*I*/d*V* spectroscopy on these systems was also very similar to what was observed on $CuPcF_{16}$, with the HOMO and LUMO peaks at similar energies and no observable Kondo feature (Figure 3.7E).

In addition, we grew thin films with Fe(II)PcF_8 (S = 3/2) and achieved large patches of self-assembled molecules (Figure 3.7C,D). Consistent with the literature, d*I*/d*V* spectroscopy collected at the molecular center shows a zero-bias anomaly associated with the Kondo effect (Figure 3.7F). This characteristic dip has previously been confirmed to have Kondo character with variable temperature measurements and does not appear as a sharp peak due to the high spin (S > 1/2) which complicates the mechanism and tends to change the shape of the zero-bias feature.[64] These $FePcF_8$ films are ideal candidates for our molecular templating strategy as a

periodic array of local magnetic moments in the presence of an electron bath, ideal for the formation of heavy fermions in 2D Van der Waals heterostructures.

3.2 Properties of TMDs

TMDs are layered materials composed of three atomic layers, with two layers of chalcogen atoms surrounding a layer of transition metal atoms. They have attracted a strong interest in condensed matter physics due to their unique transport properties and the variety of exotic correlated electronic phases they can host. For example, at low temperatures, $NbSe_2$ and several other metallic TMDs exhibit superconductivity,[121] 1T TaS_2 hosts a coexisting spin density wave (SDW) and CDW which has properties of a quantum spin liquid,[50] and $TiSe_2$ has been shown to host an excitonic insulator phase in its ground state.[128] Many of these properties are exhibited in the bulk material as well as its monolayer form, although in some cases the critical temperature for the correlated phase transition becomes much lower for the monolayer. The properties of monolayer TMDs are also highly dependent on the substrate, as hybridization can suppress some of these electronic phenomena and periodic strain due to lattice mismatch can also affect the electronic structure.[116,117] I will focus on the properties of two TMDs, MoS_2 and $NbSe_2$ which were used in the experiments detailed in sections 3.3-3.5.

MoS_2 is one of the few common naturally occurring TMDs. It exhibits semiconducting properties, with an indirect band gap of roughly 1.2 eV in its bulk form and a direct band gap of approximately 1.8 eV in its monolayer form. It has been fabricated into transistor devices shown to have high electron mobility and a large current on/off ratio. Due to the strong attraction between gold and sulfur atoms it can be easily exfoliated onto Au(111), on which it forms a distinctive hexagonal Moiré pattern (see Figure 3.10F). It has also been shown to exhibit a charge density wave in its monolayer form on Au(111) induced by the presence of selenium vacancies.[129] We chose MoS_2 for our experiments because it is cost effective and relatively easy to exfoliate compared to other TMDs.

$NbSe_2$ has been widely studied and has many unique characteristics. It is a metallic TMD which hosts a superconducting phase in its bulk form with a critical temperature around 7 K, relatively high compared to other TMDs. It is also a superconductor in its monolayer form with a T_c of 1.2 K. Bulk $NbSe_2$ also exhibits a distinct 3x3 charge density wave which is present in its bulk form and in its monolayer form depending on the substrate. For example, ML $NbSe_2$ grown on bilayer graphene or hBN retains its charge density wave and superconductive properties[121] while they are both suppressed on Au(111).[130] Like MoS_2, it is easily exfoliated onto Au(111) where it also shows a distinct hexagonal Moiré pattern (see Figure 3.11A,B). $NbSe_2$ is an optimal candidate for the molecular templated heterostructure because of its metallic properties which will be ideal for the hybridization with the molecular lattice, either through interactions between local magnetic moments and conduction electrons (Kondo, RKKY), or periodic strain and charge localization.

3.3 TMD heterostructures and exfoliation procedures

The wide range of unique intrinsic properties in TMDs presents an ideal opportunity for fabricating novel Van der Waals heterostructures. By carefully combining layers with specific properties and/or carefully tuning the twist angle between layers, even more exotic phenomena can emerge. There has been a plethora of recent research detailing the fabrication and characterization of such layered heterostructures. In this section I will discuss some important examples which are somewhat analogous to our proposed heterostructures, as well as common exfoliation and fabrication procedures.

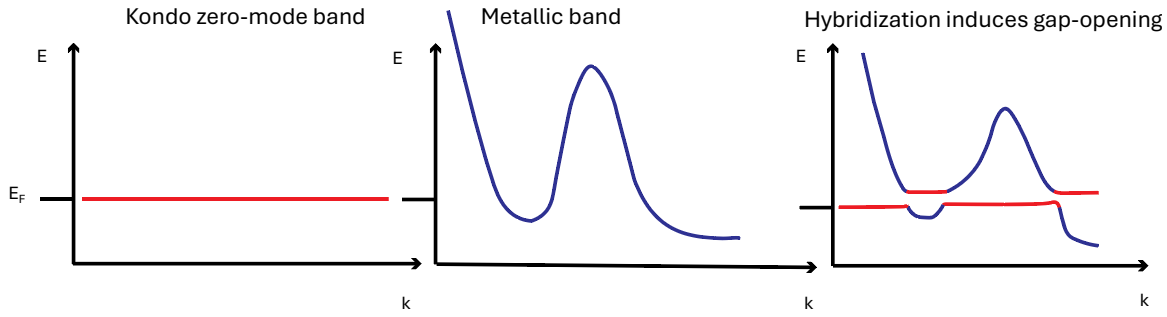

Figure 3.8 Illustration of band structure hybridization between a 2D Kondo lattice and metallic band leading to gap opening associated with heavy fermion formation.

As previously discussed, an array of magnetic moments (Kondo lattice) in the presence of an electron bath confined to a monolayer can induce the formation of heavy fermions, which serves as a platform for emergent exotic phenomena from unconventional topological superconductivity to non-Fermi liquid behavior. A simplified model of the system is shown where the zero-mode Kondo peak is treated simply as a flat band, which can hybridize with the metallic band (electron bath) resulting in a quasiparticle gap opening at the Fermi energy (Figure 3.8). This phenomenon has been demonstrated in conventional TMD heterostructures composed of the 1H and 1T phases of TaS_2. While 1H TaS_2 is a metal, 1T TaS_2 is a semiconductor with a stable charge density wave, with local magnetic moments occurring at each CDW lattice site, effectively a Kondo lattice in the presence of a metal. A quasiparticle gap was observed in d*I*/d*V* spectra obtained on 1H TaS_2 on 1T TaS_2, whereas the expected Kondo resonance was observed for the reverse orientation.[50] Analogously, we expect to observe a Kondo resonance with a magnetic phthalocyanine lattice grown on top of a metallic TMD and could possibly

observe an emergent quasiparticle gap if the metallic layer is templated with the Kondo lattice underneath it.

Many of these TMD heterostructures are grown with molecular beam epitaxy directly (MBE) on the characterization substrate. For example, the TaS_2 heterostructures mentioned above were grown using MBE on HOPG resulting in small islands and random location of the desired heterostructure.[50] Because our molecular thin films can theoretically be grown to complete coverage of an entire substrate, this would drastically simplify the process of locating the desired heterostructure as it would only require locating one monolayer flake. However, these molecular thin films are not highly temperature stable and therefore unlikely to survive during MBE or CVD growth processes, eliminating these as options for the heterostructure fabrication.

A common method for producing monolayer TMD samples on metallic substrate is the so-called "flip" method (Figure 3.9C).[131] In this technique, metal atoms are deposited onto a monolayer

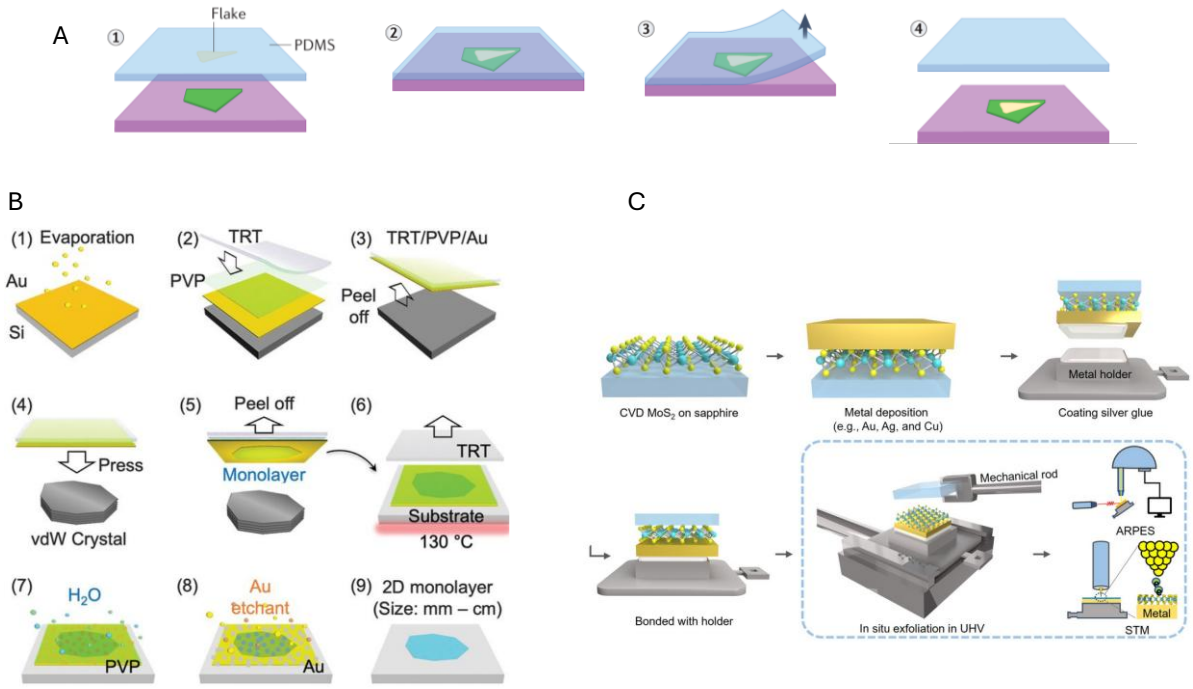

Figure 3.9 (A) Conventional exfoliation/transfer process for layered materials. Flakes are coated with a polymer film following exfoliation in to transfer onto another substrate. Reproduced from Ref 47. **(B)** Gold tape method for exfoliation of TMDs. Reproduced from Ref 132. **(C)** "Flip" method for transferring monolayer TMDs grown from CVD on insulating substrates onto gold films. Reproduced from Ref 131.

TMD sample, usually grown with CVD or sapphire or other insulating substrate. The metal film will then protect the TMD layer underneath from air as the sample is transferred. It can then be

mounted using conductive epoxy to a sample plate, and then cleaved from the growth substrate in vacuum, exposing a clean TMD monolayer. While this method can produce high quality and high coverage monolayer TMDs on metallic substrate, there are two limitations for our application. First, for air sensitive materials, the deposition of the metal film must be performed in the same chamber as the growth of the material to prevent oxidation. Second, in order to achieve a molecular thin film underneath the TMD, the molecular layer would also have to be deposited in the same chamber and would be unlikely to survive the growth of the metallic film. The “gold-tape” method is another technique that leverages the strong attraction between gold and chalcogen atoms to exfoliate TMD flakes (Figure 3.9B).[132]

The most practical method for achieving our desired heterostructures is exfoliation of the monolayer material from a bulk crystal. Layered materials are commonly exfoliated and transferred this way by cleaving a flake from bulk onto SiO_2 using the Scotch tape method, then coating the flake in a polymer film such as PMMA, which can be used to transfer the flake onto the desired substrate, generally using a small amount of heat to release the flake from the polymer film (Figure 3.8A).[47] This method does tend to induce contamination as the polymer film leaves behind a thin residue which may not be visible with ambient AFM or other techniques but strongly interferes with UHV STM measurements. Previous STM studies using this method to fabricate devices have used the so-called “scratch method”, where contact-mode AFM is used with a high deflection set-point to clean the desired flake by scanning over it repeatedly.[122] The position of the flake is then located in STM by using the metallic contacts on the device as a visual guide and then using capacitive coarse scanning to locate the flake. However, for our purposes, the absence of device contacts and the lack of an optical microscope on the STM seems to necessitate the ability to transfer multiple flakes onto the substrate at once without having to clean them individually. Ideally, the surrounding gold substrate would also be clean enough to condition the STM tip.

We attempted to exfoliate flakes of MoS_2 onto Au(111) using the polymer film method without scratch cleaning, but upon STM characterization the substrate was covered with a film that made it impossible to scan on even with significant substrate annealing (see Figure S7). Our first attempts to circumvent this issue involved choosing a different material to transfer the flake to avoid the polymer residue. Muscovite mica is an ideal candidate because it can be cleaved to expose an atomically clean surface and interacts strongly enough with the TMDs to transfer them from SiO_2 to Au(111). We attempted to transfer MoS_2 onto Au(111) using this technique, then transferred the substrate into the vacuum chamber where it was annealed at 373 K for one hour. While the gold substrate still had some residue on it, we did find multilayer flakes of MoS_2 which were relatively clean (Figure S7C).

3.4 In-vacuum transfer of monolayer TMDs

While our mica-based transfer method did produce clean multi-layer flakes of MoS_2, the surrounding substrate was not ideally clean. Moreover, intend to extend the method to air sensitive TMDs like $NbSe_2$. One way to address both challenges is to perform the exfoliation and transfer in the vacuum chamber, leveraging the strong attraction of Au(111) to chalcogen atoms. A bulk crystal can simply be glued using vacuum compatible epoxy to a stamp, cleaved in vacuum, and then brought it into contact with a gold substrate, where the surface attraction will be stronger than the interlayer attraction in the TMD crystal, resulting in cleavage of high-quality monolayer flakes (Figure 3.10A). While this is a crude exfoliation method, it results in a large number of clean monolayer flakes transferred to the substrate. This method has been demonstrated to produce much cleaner flakes than traditional exfoliation methods.[133]

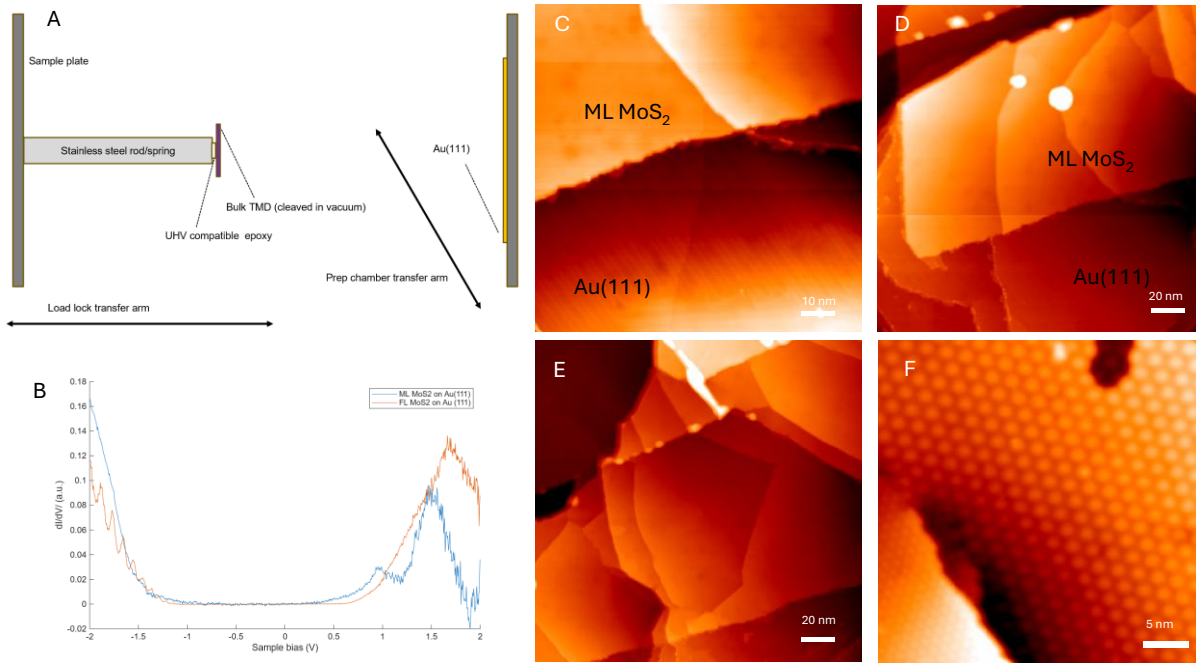

Figure 3.10 (A) Illustration of in-vacuum TMD exfoliation set-up. **(B)** dI/dV spectra of monolayer and few-layer MoS_2 transferred onto Au(111). **(C,D)** Topographic images of monolayer MoS_2 and Au(111) boundary. The areas corresponding to Au(111) and MoS_2 are labeled. **(E)** Large scale topographic image of monolayer and few layer MoS_2 on Au(111). **(F)** Topographic image of monolayer MoS_2 on Au(111) clearly displaying the hexagonal Moiré pattern, the periodicity of which differs on different grains of Au(111).

Our first attempts to perform this technique involved $NbSe_2$. We built a stamp by attaching a small metal rod to a sample plate and mounting the $NbSe_2$ crystal to the rod using Torr Seal epoxy. The $NbSe_2$ was cleaved in the load lock using Kapton tape and transferred into the preparation chamber where it was brought into contact with a clean Au(111) surface. After slowly and rigidly separating the stamp from the substrate, the substrate was annealed to 373 K

for 30 min. STM characterization of the sample revealed that there was still quite a bit of surface contamination, albeit much cleaner than any previous attempts. Clean few layer (see Figure S8) and monolayer flakes of $NbSe_2$ (Figure 3.11) were both located on the substrate. The monolayer $NbSe_2$ shows a distinctive hexagonal Moiré pattern characteristic of the mismatch between the TMD and Au(111) lattices (Figure 3.11A,B). The Moiré lattice varies in size on different terraces due to different orientation angles, and the monolayer flake maps very well over the gold step edges. d*I*/d*V* spectroscopy on these areas is consistent with reports for monolayer $NbSe_2$ on Au(111) (Figure 3.11D), with a distinct peak around 1.0 V and a featureless spectrum near the Fermi energy, as the charge density wave is suppressed.[130] However, in areas where few to multi-layer $NbSe_2$ is observed, the charge density wave is visible in the STM images (Figure 3.12E,F), and a gap is also apparent in the d*I*/d*V* spectrum around the Fermi energy consistent with the CDW gap (Figure 3.12 G,H). The FFT image also shows distinct peaks at 1/3 of the Bragg vector, consistent with a 3x3 CDW (inset Figure 3.12E).[121]

We narrowed the source of the surface contamination to the Torr Seal epoxy, and to produce cleaner samples we built a stamp using a conductive epoxy (H20E), this time with MoS_2. We also modified the stamp design with a spring in order to maximize the contact area between the TMD crystal and the Au(111) substrate. A very small amount of H20E was applied to the stamp and the MoS_2 was attached to it. The stamp was then baked in an oven to cure the epoxy at 373 K for an hour, then transferred into an isolated vacuum chamber where it was baked in order to remove any outgassing contaminants from the epoxy. Finally, the MoS_2 was cleaved and the stamp was moved into the vacuum chamber, where we performed the exfoliation onto Au(111), which was then annealed at 373 K. This resulted in high quality large monolayer flakes with minimal surface contamination (3.10A). Again, the distinctive hexagonal Moiré pattern is apparent on the areas with monolayer MoS_2. The spectroscopy of both monolayer and few layer MoS_2 is consistent with the literature.[131]

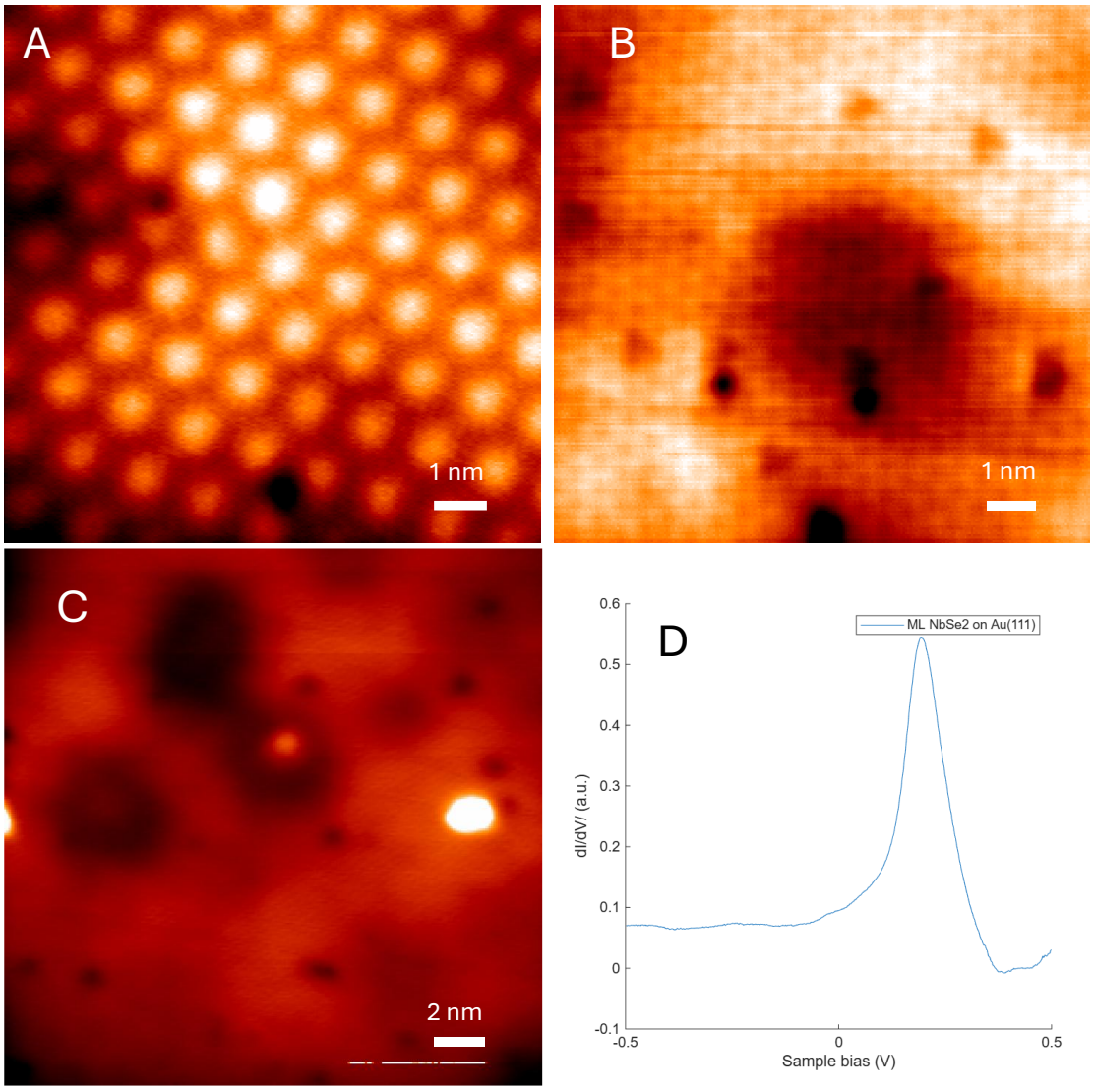

Figure 3.11 (A-C) Topographic images of monolayer $NbSe_2$ on Au(111). **A** and **B** show the distinct Au(111)/TMD Moiré patter. **(D)** d*I*/d*V* spectroscopy of monolayer $NbSe_2$ on Au(111).

3.5 Heterostructure fabrication attempts

We first attempted to grow molecular thin films of $CuPcF_8$ on flakes of $NbSe_2$ transferred to Au(111). On several occasions we located patches of self-assembled molecular films on multi/few layer $NbSe_2$ (Figure 3.12A-D). d*I*/d*V* spectroscopy collected on the molecular patches displayed no Kondo resonance at zero bias, the same as $CuPcF_8$ on Au(111). Instead, as the $NbSe_2$ flakes in these cases were composed of multiple layers, the CDW gap was visible in the STS spectrum, convoluting the spectroscopy near zero bias (Figure 3.12 G). A distinct variation between spectroscopy collected on the molecular thin film and on the bare $NbSe_2$ was not observed, however the zero-bias gap did appear slightly narrower for spectra collected on the molecular thin film (Figure 3.12H).

We then attempted to fabricate the molecular templated heterostructures by first growing high coverage films of $FePcF_8$ and then attempting to exfoliate ML MoS_2 onto the substrate. Films of $FePcF_8$ were grown on Au(111) at about 50% ML coverage, leaving exposed gold for the MoS_2 flakes to ideally adhere to. The in-vacuum exfoliation of MoS_2 was then attempted on the same substrate. The substrate was then annealed to 373 K for about 10 min. Unfortunately, STM imaging revealed that a significant portion of the molecule had sublimed from the surface during the annealing process. However, some large self-assembled patches remained on the surface. Large terraces of ML MoS_2 were observed on the surface, in some cases very close to molecular patches (Figure 3.13 and Figure S9). On several occasions we located smaller ML MoS_2 flakes ~10 nm directly up against small molecular patches, with a small amount of overlap at the edge (Figure 3.13A-C,E). STS spectroscopy at the center of the flakes was consistent with ML MoS_2 strongly coupled to Au(111). At the edge of the flake however, the spectrum was more consistent with few layer MoS_2 indicating that the edge could be slightly decoupled from the gold surface by the molecule (Figure 3.13D). However, no distinct overlap or templating of the MoS_2 with the molecule was observed. It appears that the attraction between the MoS_2 and the gold is too strong for any interaction between the molecules, which are likely mobile at room temperature, and the MoS_2. We hypothesize that the MoS_2 flakes displace the molecule during transfer.

We also attempted to fabricate heterostructures with the TOTA Coulomb crystal and ML MoS_2 using the same process. High coverage films of $TOTA^+$ were grown by subliming TOTA-H onto Au(111) and annealing the substrate to 373 K. Subsequently, MoS_2 was transferred onto the substrate using the in-vacuum exfoliation technique. In some areas, like the experiments with the $FePcF_8$ films, small monolayer MoS_2 flakes were observed with the distinctive hexagonal Moiré pattern indicating that they were strongly hybridized with Au(111). TOTA was observed along the edges of the MoS_2 flakes and appeared to have been similarly displaced during transfer (Figure 3.14). In some areas, terraces which appeared to be on top of the molecular thin film were observed, but we could not confirm that it was MoS_2 due to what appeared to be

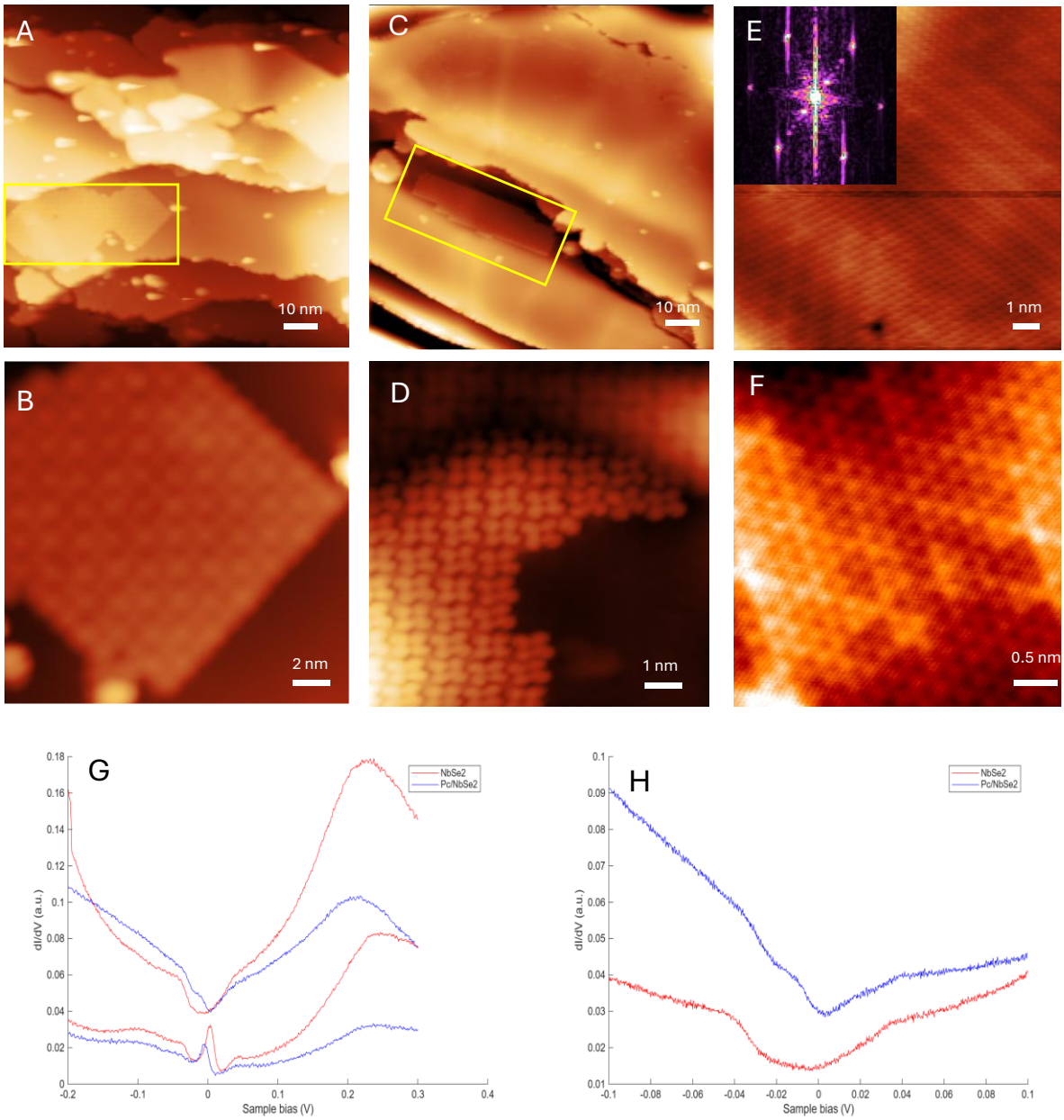

Figure 3.12 (A–D) Topographic images of $CuPcF_8$ films grown on few layer $NbSe_2$ transferred onto Au(111). The patches of self-assembled molecules are highlighted with yellow boxes in large scale images **A** and **C**. **(E,F)** Topographic images of bare few layer $NbSe_2$ transferred onto Au(111). The inset in **E** shows the 2D FFT of the image, which displays peaks corresponding to a 3x3 CDW. **(G,H)** d*I*/d*V* spectroscopy in areas with $CuPcF_8$ thin films on few layer $NbSe_2$. The red curves were collected directly on $NbSe_2$ and the blue curves were collected on the $CuPcF_8$ molecular center. The two sets of curves in **G** correspond to different occurrences of $CuPcF_8$ on $NbSe_2$ with different tips and are artificially offset. The slight narrowing of the CDW gap is highlighted in **H**.

strong mechanical noise when scanning on these areas, which was not present in the same scan window where the molecule was visible. This could possibly be MoS_2 and if so indicate that it is not strongly coupled with the surface, or that some residue is still present in some areas.

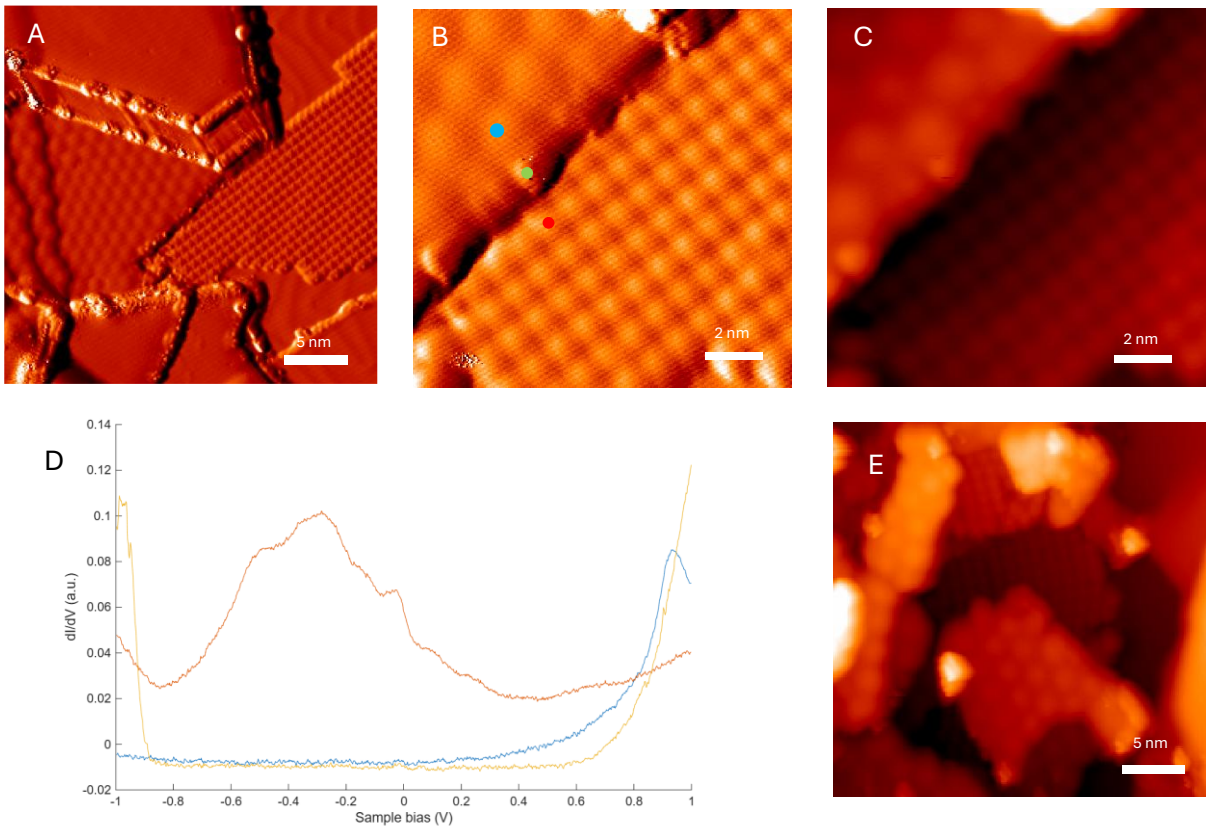

Figure 3.13 Images and spectroscopy of monolayer MoS_2 transferred onto Au(111) with $FePcF_8$ islands. **(A,B)** Current images of $FePcF_8$ thin films intersecting with monolayer MoS_2 on Au(111). A Moiré pattern is observed on the monolayer MoS_2. **B** shows the boundary between the molecular thin film and the monolayer MoS_2 where there is a possible overlap. The dots on the image represent the locations where d*I*/d*V* spectroscopy was collected and correspond by color to the spectra in **D**. **(C)** Topographic image corresponding to **B**. **(D)** d*I*/d*V* spectroscopy at locations corresponding to dots in **B**. **(E)** Topographic image of another area with monolayer MoS_2 near $FePcF_8$ thin film.

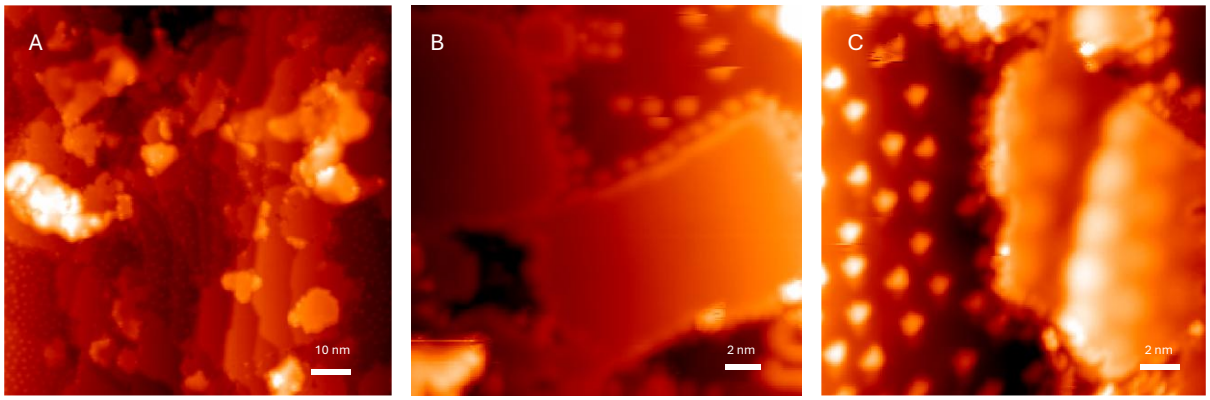

Figure 3.14 Topographic images of monolayer MoS_2 transferred onto Au(111) with $TOTA^+$ thin film.

3.6 Outlook

We conclude that this crude method may not be sufficient for fabricating molecular templated heterostructures due to the instability and mobility of the molecular films on the surface at room temperature. Further experiments are being planned to screen different molecular thin films and layered materials. More sophisticated device fabrication techniques may also be able to access the desired structures. We could employ the scratch cleaning method so that we may rely on conventional exfoliation methods that do not require Au(111) or similar metal substrate. However this would require that the molecular films survive ambient conditions and subsequent in-vacuum annealing. Confining the molecules in a porous 2D material and stacking this with the desired heterostructure monolayer could allow us to trap the molecular thin films under the TMDs. Substrate annealing could then subsequently be performed to improve cleanliness without risking subliming the molecular thin films from the substrate, although they still may decompose at higher temperatures. Demonstrative success of this strategy could incite a new phase of heterostructure fabrication and research.

References

1. Wallace, P. R. The Band Theory of Graphite. *Phys. Rev.* **71**, 622–634 (1947).

2. Castro Neto, A. H., Guinea, F., Peres, N. M. R., Novoselov, K. S. & Geim, A. K. The electronic properties of graphene. *Rev. Mod. Phys.* **81**, 109–162 (2009).

3. Novoselov, K. S. *et al.* Electric Field Effect in Atomically Thin Carbon Films. *Science* **306**, 666–669 (2004).

4. Novoselov, K. S. *et al.* Two-dimensional gas of massless Dirac fermions in graphene. *Nature* **438**, 197–200 (2005).

5. Bolotin, K. I. *et al.* Ultrahigh electron mobility in suspended graphene. *Solid State Communications* **146**, 351–355 (2008).

6. Das Sarma, S., Adam, S., Hwang, E. H. & Rossi, E. Electronic transport in two-dimensional graphene. *Rev. Mod. Phys.* **83**, 407–470 (2011).

7. Reddy, D., Register, L. F., Carpenter, G. D. & Banerjee, S. K. Graphene field-effect transistors. *J. Phys. D: Appl. Phys.* **44**, 313001 (2011).

8. Ohta, T., Bostwick, A., Seyller, T., Horn, K. & Rotenberg, E. Controlling the Electronic Structure of Bilayer Graphene. *Science* **313**, 951–954 (2006).

9. Castro, E. V. *et al.* Biased Bilayer Graphene: Semiconductor with a Gap Tunable by the Electric Field Effect. *Phys. Rev. Lett.* **99**, 216802 (2007).

10. Zhang, Y. *et al.* Direct observation of a widely tunable bandgap in bilayer graphene. *Nature* **459**, 820–823 (2009).

11. Nakada, K., Fujita, M., Dresselhaus, G. & Dresselhaus, M. S. Edge state in graphene ribbons: Nanometer size effect and edge shape dependence. *Phys. Rev. B* **54**, 17954–17961 (1996).

12. Son, Y.-W., Cohen, M. L. & Louie, S. G. Energy Gaps in Graphene Nanoribbons. *Phys. Rev. Lett.* **97**, 216803 (2006).

13. Fujita, M., Wakabayashi, K., Nakada, K. & Kusakabe, K. Peculiar Localized State at Zigzag Graphite Edge. *J. Phys. Soc. Jpn.* **65**, 1920–1923 (1996).

14. Blackwell, R. E. *et al.* Spin splitting of dopant edge state in magnetic zigzag graphene nanoribbons. *Nature* **600**, 647–652 (2021).

15. Ruffieux, P. *et al.* On-surface synthesis of graphene nanoribbons with zigzag edge topology. *Nature* **531**, 489–492 (2016).

16. Son, Y.-W., Cohen, M. L. & Louie, S. G. Half-metallic graphene nanoribbons. *Nature* **444**, 347–349 (2006).

17. Lee, Y.-L., Zhao, F., Cao, T., Ihm, J. & Louie, S. G. Topological Phases in Cove-Edged and Chevron Graphene Nanoribbons: Geometric Structures, Z2 Invariants, and Junction States. *Nano Lett.* **18**, 7247–7253 (2018).

18. Pereira Júnior, M. L. *et al.* Charge Transport Mechanism in Chevron-Graphene Nanoribbons. *J. Phys. Chem. C* **124**, 22392–22398 (2020).

19. Yazyev, O. V., Capaz, R. B. & Louie, S. G. Theory of magnetic edge states in chiral graphene nanoribbons. *Phys. Rev. B* **84**, 115406 (2011).

20. Tao, C. *et al.* Spatially resolving edge states of chiral graphene nanoribbons. *Nature Phys* **7**, 616–620 (2011).

21. Wang, X.-Y. *et al.* Bottom-Up Synthesis of Heteroatom-Doped Chiral Graphene Nanoribbons. *J. Am. Chem. Soc.* **140**, 9104–9107 (2018).

22. Jacobse, P. H. *et al.* Five-Membered Rings Create Off-Zero Modes in Nanographene. *ACS Nano* **17**, 24901–24909 (2023).

23. McCurdy, R. D. *et al.* Engineering Robust Metallic Zero-Mode States in Olympicene Graphene Nanoribbons. *J. Am. Chem. Soc.* **145**, 15162–15170 (2023).

24. Rizzo, D. J. *et al.* Inducing metallicity in graphene nanoribbons via zero-mode superlattices. *Science* **369**, 1597–1603 (2020).

25. Gröning, O. *et al.* Engineering of robust topological quantum phases in graphene nanoribbons. *Nature* **560**, 209–213 (2018).

26. Zhu, X. *et al.* Topological Structure Realized in Cove-Edged Graphene Nanoribbons via Incorporation of Periodic Pentagon Rings. *J. Am. Chem. Soc.* **146**, 7152–7158 (2024).

27. McCurdy, R. D. *et al.* Engineering Robust Metallic Zero-Mode States in Olympicene Graphene Nanoribbons. *J. Am. Chem. Soc.* **145**, 15162–15170 (2023).

28. Rizzo, D. J. *et al.* Topological band engineering of graphene nanoribbons. *Nature* **560**, 204–208 (2018).

29. Rizzo, D. J. *et al.* Rationally Designed Topological Quantum Dots in Bottom-Up Graphene Nanoribbons. *ACS Nano* **15**, 20633–20642 (2021).

30. Wen, E. C. H. *et al.* Fermi-Level Engineering of Nitrogen Core-Doped Armchair Graphene Nanoribbons. *J. Am. Chem. Soc.* **145**, 19338–19346 (2023).

31. Jacobse, P. H. *et al.* Coupling of Nondegenerate Topological Modes in Nitrogen Core-Doped Graphene Nanoribbons. *ACS Nano* **19**, 13029–13036 (2025).

32. Wen, E. C. H. *et al.* Magnetic Interactions in Substitutional Core-Doped Graphene Nanoribbons. *J. Am. Chem. Soc.* **144**, 13696–13703 (2022).

33. Durr, R. A. *et al.* Orbitally Matched Edge-Doping in Graphene Nanoribbons. *J. Am. Chem. Soc.* **140**, 807–813 (2018).

34. Abbas, A. N. *et al.* Patterning, Characterization, and Chemical Sensing Applications of Graphene Nanoribbon Arrays Down to 5 nm Using Helium Ion Beam Lithography. *ACS Nano* **8**, 1538–1546 (2014).

35. Kosynkin, D. V. *et al.* Longitudinal unzipping of carbon nanotubes to form graphene nanoribbons. *Nature* **458**, 872–876 (2009).

36. Chen, Z. *et al.* Synthesis of Graphene Nanoribbons by Ambient-Pressure Chemical Vapor Deposition and Device Integration. *J. Am. Chem. Soc.* **138**, 15488–15496 (2016).

37. Shekhirev, M. *et al.* Highly Selective Gas Sensors Based on Graphene Nanoribbons Grown by Chemical Vapor Deposition. *ACS Appl. Mater. Interfaces* **12**, 7392–7402 (2020).

38. Lyu, B. *et al.* Graphene nanoribbons grown in hBN stacks for high-performance electronics. *Nature* **628**, 758–764 (2024).

39. Bottom-Up Synthesized Nanoporous Graphene Transistors - Mutlu - 2021 - Advanced Functional Materials - Wiley Online Library. https://advanced.onlinelibrary.wiley.com/doi/abs/10.1002/adfm.202103798.

40. Cai, J. *et al.* Atomically precise bottom-up fabrication of graphene nanoribbons. *Nature* **466**, 470–473 (2010).

41. Talirz, L., Ruffieux, P. & Fasel, R. On-Surface Synthesis of Atomically Precise Graphene Nanoribbons. *Advanced Materials* **28**, 6222–6231 (2016).

42. Grill, L. *et al.* Nano-architectures by covalent assembly of molecular building blocks. *Nature Nanotech* **2**, 687–691 (2007).

43. Pun, S. H., Delgado, A., Dadich, C., Cronin, A. & Fischer, F. R. Controlled catalyst-transfer polymerization in graphene nanoribbon synthesis. *Chem* **10**, 675–685 (2024).

44. Webster, O. W. Living Polymerization Methods. *Science* **251**, 887–893 (1991).

45. Ballard, J. B., Carmichael, E. S., Shi, D., Lyding, J. W. & Gruebele, M. Laser Absorption Scanning Tunneling Microscopy of Carbon Nanotubes. *Nano Lett.* **6**, 45–49 (2006).

46. Albrecht, P. M. & Lyding, J. W. Ultrahigh-vacuum scanning tunneling microscopy and spectroscopy of single-walled carbon nanotubes on hydrogen-passivated Si(100) surfaces. *Appl. Phys. Lett.* **83**, 5029–5031 (2003).

47. Castellanos-Gomez, A. *et al.* Van der Waals heterostructures. *Nat Rev Methods Primers* **2**, 58 (2022).

48. Geim, A. K. & Grigorieva, I. V. Van der Waals heterostructures. *Nature* **499**, 419–425 (2013).

49. Cao, Y. *et al.* Unconventional superconductivity in magic-angle graphene superlattices. *Nature* **556**, 43–50 (2018).

50. Vaňo, V. *et al.* Artificial heavy fermions in a van der Waals heterostructure. *Nature* **599**, 582–586 (2021).

51. Voigtlander, B. *Scanning Probe Microscopy - Atomic Force Microscopy and Scanning Tunneling Microscopy*. (Springer, 2015).

52. Bardeen, J. Tunnelling from a Many-Particle Point of View. *Phys. Rev. Lett.* **6**, 57–59 (1961).

53. Tersoff, J. & Hamann, D. R. Theory of the scanning tunneling microscope. *Phys. Rev. B* **31**, 805–813 (1985).

54. Gross, L., Mohn, F., Moll, N., Liljeroth, P. & Meyer, G. The Chemical Structure of a Molecule Resolved by Atomic Force Microscopy. *Science* **325**, 1110–1114 (2009).

55. Gross, L. *et al.* Bond-Order Discrimination by Atomic Force Microscopy. *Science* **337**, 1326–1329 (2012).

56. Mohn, F., Gross, L., Moll, N. & Meyer, G. Imaging the charge distribution within a single molecule. *Nature Nanotech* **7**, 227–231 (2012).

57. Hapala, P. *et al.* Mechanism of high-resolution STM/AFM imaging with functionalized tips. *Phys. Rev. B* **90**, 085421 (2014).

58. Repp, J., Meyer, G., Stojković, S. M., Gourdon, A. & Joachim, C. Molecules on Insulating Films: Scanning-Tunneling Microscopy Imaging of Individual Molecular Orbitals. *Phys. Rev. Lett.* **94**, 026803 (2005).

59. Giessibl, F. J. Atomic resolution on Si(111)-(7×7) by noncontact atomic force microscopy with a force sensor based on a quartz tuning fork. *Appl. Phys. Lett.* **76**, 1470–1472 (2000).

60. Kittel, C. *Introduction to Solid State Physics*. (Wiley, 2005).

61. Balents, L. Spin liquids in frustrated magnets. *Nature* **464**, 199–208 (2010).

62. Bardeen, J., Cooper, L. N. & Schrieffer, J. R. Theory of Superconductivity. *Phys. Rev.* **108**, 1175–1204 (1957).

63. Madhavan, V., Chen, W., Jamneala, T., Crommie, M. F. & Wingreen, N. S. Tunneling into a Single Magnetic Atom: Spectroscopic Evidence of the Kondo Resonance. *Science* **280**, 567–569 (1998).

64. Giro$V_s$ky, J. *et al.* Long-range ferrimagnetic order in a two-dimensional supramolecular Kondo lattice. *Nat Commun* **8**, 15388 (2017).

65. Turco, E. Demonstrating Kondo behavior by temperature-dependent scanning tunneling spectroscopy. *Phys. Rev. Res.* **6**, (2024).

66. Mishra, S. *et al.* Collective All-Carbon Magnetism in Triangulene Dimers. *Angewandte Chemie* **132**, 12139–12145 (2020).

67. Catarina, G. *et al.* Conformational Tuning of Magnetic Interactions in Coupled Nanographenes. *Nano Lett.* **24**, 12536–12544 (2024).

68. Yazyev, O. V. Emergence of magnetism in graphene materials and nanostructures. *Rep. Prog. Phys.* **73**, 056501 (2010).

69. Lieb, E. H. Two theorems on the Hubbard model. *Phys. Rev. Lett.* **62**, 1201–1204 (1989).

70. Hubbard, J. Electron correlations in narrow energy bands. *Proc. A* **276**, 238–257 (1963).

71. Ovchinnikov, A. A. Multiplicity of the ground state of large alternant organic molecules with conjugated bonds. *Theoret. Chim. Acta* **47**, 297–304 (1978).

72. Mishra, S. *et al.* Synthesis and Characterization of π-Extended Triangulene. *J. Am. Chem. Soc.* **141**, 10621–10625 (2019).

73. Hermele, M., Ran, Y., Lee, P. A. & Wen, X.-G. Properties of an algebraic spin liquid on the kagome lattice. *Phys. Rev. B* **77**, 224413 (2008).

74. Guo, H.-M. & Franz, M. Topological insulator on the kagome lattice. *Phys. Rev. B* **80**, 113102 (2009).

75. Yan, Y. *et al.* Engineering phase-frustration-induced flat bands in an aza-triangulene covalent kagome lattice. *Nat. Mater.* 1–8 (2026) doi:10.1038/s41563-026-02528-3.

76. Sethi, G., Zhou, Y., Zhu, L., Yang, L. & Liu, F. Flat-Band-Enabled Triplet Excitonic Insulator in a Diatomic Kagome Lattice. *Phys. Rev. Lett.* **126**, 196403 (2021).

77. Delgado, A. *et al.* Low Energy Excitations in a [4]Triangulene Honeycomb Antiferromagnet. (2026).

78. Björk, J., Hanke, F. & Stafström, S. Mechanisms of Halogen-Based Covalent Self-Assembly on Metal Surfaces. *J. Am. Chem. Soc.* **135**, 5768–5775 (2013).

79. Wang, X. *et al.* Cove-Edged Graphene Nanoribbons with Incorporation of Periodic Zigzag-Edge Segments. *J. Am. Chem. Soc.* **144**, 228–235 (2022).

80. Kinikar, A. *et al.* Sterically Selective [3 + 3] Cycloaromatization in the On-Surface Synthesis of Nanographenes. *ACS Nanosci. Au* **4**, 128–135 (2024).

81. Kinikar, A. *et al.* On-surface polyarylene synthesis by cycloaromatization of isopropyl substituents. *Nat. Synth* **1**, 289–296 (2022).

82. Hatcher, A. *Algebraic Topology*. (Cambridge University Press).

83. Senthil, T. Symmetry-Protected Topological Phases of Quantum Matter. *Annual Review of Condensed Matter Physics* **6**, 299–324 (2015).

84. Flensberg, K., von Oppen, F. & Stern, A. Engineered platforms for topological superconductivity and Majorana zero modes. *Nat Rev Mater* **6**, 944–958 (2021).

85. Lutchyn, R. M. *et al.* Majorana zero modes in superconductor–semiconductor heterostructures. *Nat Rev Mater* **3**, 52–68 (2018).

86. Starostin, E. L. & van der Heijden, G. H. M. The shape of a Möbius strip. *Nature Mater* **6**, 563–567 (2007).

87. Berry, M. V. Quantal Phase Factors Accompanying Adiabatic Changes. *Proceedings of the Royal Society of London. Series A, Mathematical and Physical Sciences* **392**, 45–57 (1984).

88. Zak, J. Berry's phase for energy bands in solids. *Phys. Rev. Lett.* **62**, 2747–2750 (1989).

89. Xiao, D., Chang, M.-C. & Niu, Q. Berry phase effects on electronic properties. *Rev. Mod. Phys.* **82**, 1959–2007 (2010).

90. Cao, T., Zhao, F. & Louie, S. G. Topological Phases in Graphene Nanoribbons: Junction States, Spin Centers, and Quantum Spin Chains. *Phys. Rev. Lett.* **119**, 076401 (2017).

91. Diniz, G. S., Luiz, G. I., Latgé, A. & Vernek, E. From Kondo to local singlet state in graphene nanoribbons with magnetic impurities. *Phys. Rev. B* **97**, 115444 (2018).

92. Slicker, K. *et al.* Engineering Small HOMO–LUMO Gaps in Polycyclic Aromatic Hydrocarbons with Topologically Protected States. *Nano Lett.* **24**, 5387–5392 (2024).

93. Yin, R. *et al.* Tailoring Near Fermi-Level Topological Flatbands in Clar's Goblet Graphene Nanoribbons through Regioselective Cyclization of Five-Membered Rings. *J. Am. Chem. Soc.* **147**, 34303–34315 (2025).

94. Daugherty, M. C. *et al.* Regioselective On-Surface Synthesis of [3]Triangulene Graphene Nanoribbons. *J. Am. Chem. Soc.* **146**, 15879–15886 (2024).

95. Zhang, Y., Pun, S. H. & Miao, Q. The Scholl Reaction as a Powerful Tool for Synthesis of Curved Polycyclic Aromatics. *Chem. Rev.* **122**, 14554–14593 (2022).

96. Veber, G. *et al.* Reticular Growth of Graphene Nanoribbon 2D Covalent Organic Frameworks. *Chem* **6**, 1125–1133 (2020).

97. McCurdy, R. D. *et al.* Synergetic Bottom-Up Synthesis of Graphene Nanoribbons by Matrix-Assisted Direct Transfer. *J. Am. Chem. Soc.* **143**, 4174–4178 (2021).

98. Yin, J. *et al.* Programmable Fabrication of Monodisperse Graphene Nanoribbons via Deterministic Iterative Synthesis. *J. Am. Chem. Soc.* **144**, 16012–16019 (2022).

99. Elmalem, E., Kiriy, A. & Huck, W. T. S. Chain-Growth Suzuki Polymerization of n-Type Fluorene Copolymers. *Macromolecules* **44**, 9057–9061 (2011).

100. Yokoyama, A. *et al.* Chain-Growth Polymerization for the Synthesis of Polyfluorene via Suzuki−Miyaura Coupling Reaction from an Externally Added Initiator Unit. *J. Am. Chem. Soc.* **129**, 7236–7237 (2007).

101. Yokozawa, T. & Yokoyama, A. Chain-Growth Condensation Polymerization for the Synthesis of Well-Defined Condensation Polymers and π-Conjugated Polymers. *Chem. Rev.* **109**, 5595–5619 (2009).

102. Borin Barin, G. *et al.* Surface-Synthesized Graphene Nanoribbons for Room Temperature Switching Devices: Substrate Transfer and ex Situ Characterization. *ACS Appl. Nano Mater.* **2**, 2184–2192 (2019).

103. Satterley, C. J. *et al.* Electrospray deposition of fullerenes in ultra-high vacuum: in situ scanning tunneling microscopy and photoemission spectroscopy. *Nanotechnology* **18**, 455304 (2007).

104. Zhao, X. *et al.* Spray deposition of steam treated and functionalized single-walled and multi-walled carbon nanotube films for supercapacitors. *Nanotechnology* **20**, 065605 (2009).

105. Powell, M. J. & Carmalt, C. J. Aerosols: A Sustainable Route to Functional Materials. *Chemistry – A European Journal* **23**, 15543–15552 (2017).

106. Bisen, G. G. *et al.* Effect of substrate temperature on ultrasonic spray deposited film morphology and coffee stain effect. *Bull Mater Sci* **47**, 67 (2024).

107. Majumder, M. *et al.* Overcoming the "Coffee-Stain" Effect by Compositional Marangoni-Flow-Assisted Drop-Drying. *J. Phys. Chem. B* **116**, 6536–6542 (2012).

108. Hinaut, A. *et al.* Electrospray deposition of structurally complex molecules revealed by atomic force microscopy. *Nanoscale* **10**, 1337–1344 (2018).

109. Kolar, K. *et al.* Clean Electrospray Deposition of Porphyrin Molecules and Polyethylene Glycol Chains onto a Au(100) Surface. *J. Phys. Chem. C* **130**, 650–660 (2026).

110. Wu, Q. *et al.* Electronic and transport properties of phosphorene nanoribbons. *Phys. Rev. B* **92**, 035436 (2015).

111. Nourbakhsh, Z. & Asgari, R. Excitons and optical spectra of phosphorene nanoribbons. *Phys. Rev. B* **94**, 035437 (2016).

112. Ashoka, A. *et al.* Magnetically and optically active edges in phosphorene nanoribbons. *Nature* **639**, 348–353 (2025).

113. Sofer, Z. *et al.* Layered Black Phosphorus: Strongly Anisotropic Magnetic, Electronic, and Electron-Transfer Properties. *Angewandte Chemie International Edition* **55**, 3382–3386 (2016).

114. Watts, M. C. *et al.* Production of phosphorene nanoribbons. *Nature* **568**, 216–220 (2019).

115. Zhu, Z. *et al.* Magnetism of zigzag edge phosphorene nanoribbons. *Appl. Phys. Lett.* **105**, 113105 (2014).

116. Andrei, E. Y. *et al.* The marvels of moiré materials. *Nat Rev Mater* **6**, 201–206 (2021).

117. He, F. *et al.* Moiré Patterns in 2D Materials: A Review. *ACS Nano* **15**, 5944–5958 (2021).

118. Yankowitz, M. *et al.* Tuning superconductivity in twisted bilayer graphene. *Science* **363**, 1059–1064 (2019).

119. Tarnopolsky, G., Kruchkov, A. J. & Vishwanath, A. Origin of Magic Angles in Twisted Bilayer Graphene. *Phys. Rev. Lett.* **122**, 106405 (2019).

120. Hou, Y. *et al.* Strain Engineering of Twisted Bilayer Graphene: The Rise of Strain-Twistronics. *Small* **21**, 2311185 (2025).

121. Ugeda, M. M. *et al.* Characterization of collective ground states in single-layer NbSe2. *Nature Phys* **12**, 92–97 (2016).

122. Tsai, H.-Z. *et al.* Molecular Self-Assembly in a Poorly Screened Environment: F4TCNQ on Graphene/BN. *ACS Nano* **9**, 12168–12173 (2015).

123. Bergmann, G. Ruderman-Kittel-Kasuya-Yosida interaction in disordered metals. *Phys. Rev. B* **36**, 2469–2472 (1987).

124. Mortezapour, B., Hamer, S., Herges, R., Robles, R. & Berndt, R. Orientational Order of Phenyl Rotors on Triangular Platforms on Ag and Au(111). *ACS Nano* **19**, 38773–38780 (2025).

125. Jasper-Tönnies, T. *et al.* Stability of functionalized platform molecules on Au(111). *J. Chem. Phys.* **149**, 244705 (2018).

126. Kiesenhofer, D. *et al.* Controlling Two-Dimensional Coulomb Crystals of More Than 100 Ions in a Monolithic Radio-Frequency Trap. *PRX Quantum* **4**, 020317 (2023).

127. Claessens, C. G., Hahn, U. & Torres, T. Phthalocyanines: From outstanding electronic properties to emerging applications. *The Chemical Record* **8**, 75–97 (2008).

128. Cheng, Y. *et al.* Light-induced dimension crossover dictated by excitonic correlations. *Nat Commun* **13**, 963 (2022).

129. Radisavljevic, B., Radenovic, A., Brivio, J., Giacometti, V. & Kis, A. Single-layer MoS2 transistors. *Nature Nanotech* **6**, 147–150 (2011).

130. Dreher, P. *et al.* Proximity Effects on the Charge Density Wave Order and Superconductivity in Single-Layer NbSe2. *ACS Nano* **15**, 19430–19438 (2021).

131. Shen, J. *et al.* Metal-assisted vacuum transfer enabling in situ visualization of charge density waves in monolayer MoS2. *Science Advances* **11**, eadr9753 (2025).

132. Liu, F. *et al.* Disassembling 2D van der Waals crystals into macroscopic monolayers and reassembling into artificial lattices. *Science* **367**, 903–906 (2020).

133. Panasci, S. E., Schilirò, E., Roccaforte, F. & Giannazzo, F. Gold-Assisted Exfoliation of Large-Area Monolayer Transition Metal Dichalcogenides: From Interface Properties to Device Applications. *Advanced Functional Materials* **35**, 2414532 (2025).

Supporting Figures

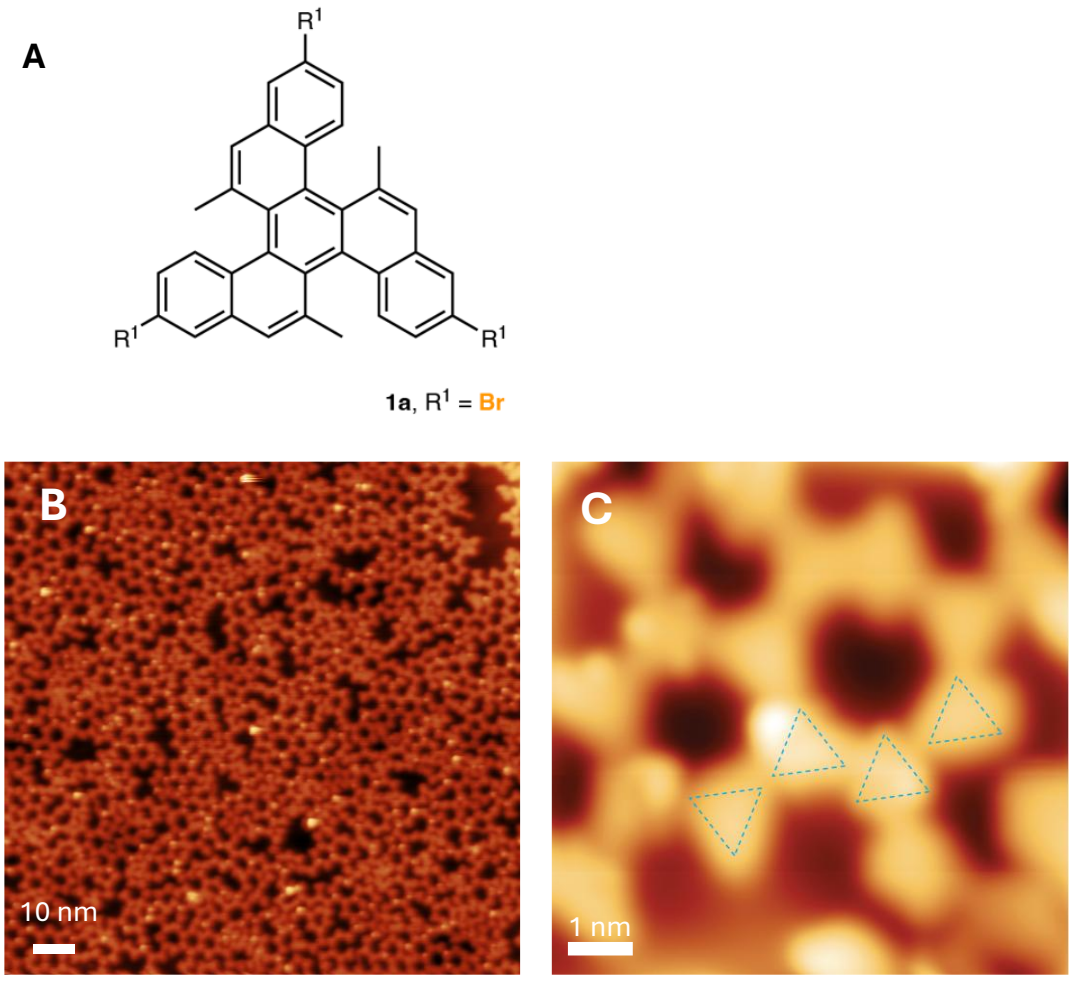

Figure S1. (A) Structure of [4]TCOF precursor **1a**. **(B,C)** STM topographic images following growth attempts of [4]TCOF from precursor **1a** on Au(111). V_s = 200 mV, I = 20 pA.

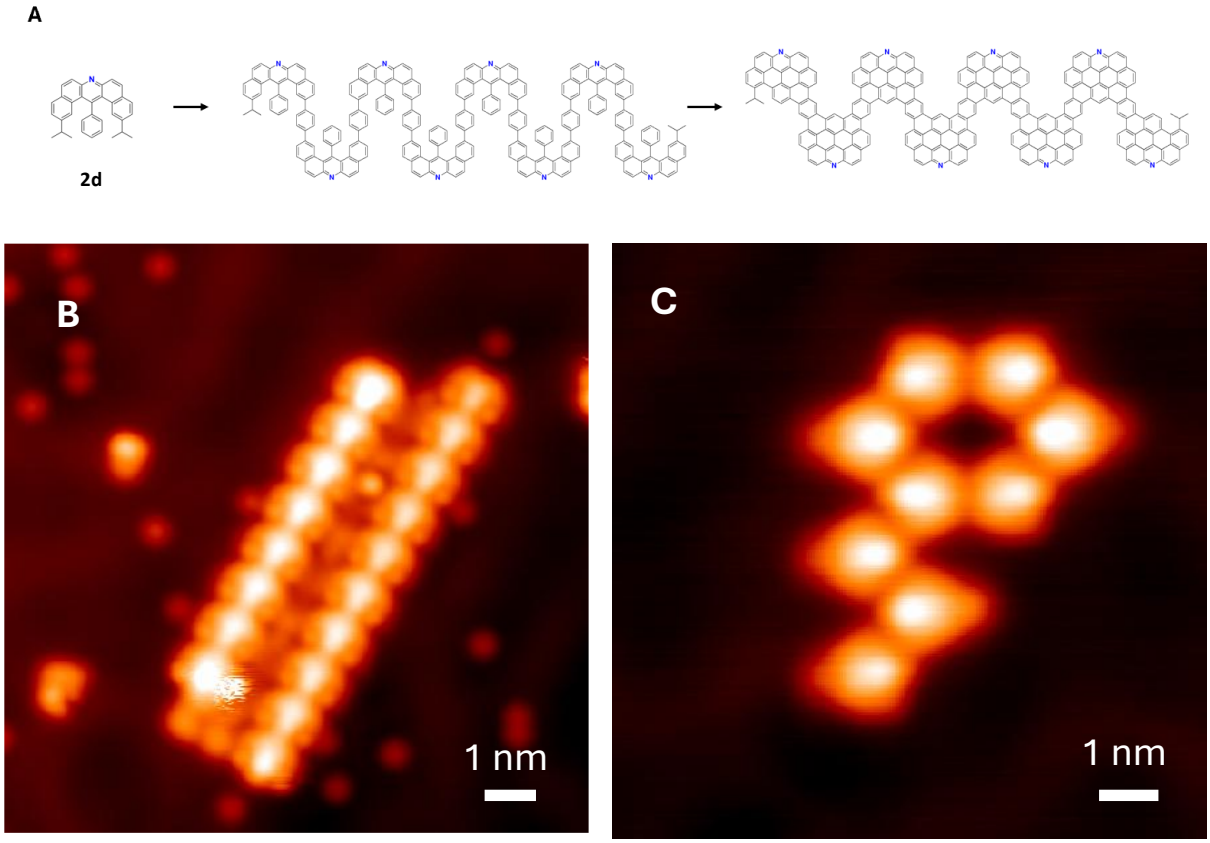

Figure S2. (A) Proposed scheme for on surface synthesis of a 1D nanographene from precursor **2d**. **(B)** STM topographic image of precursor **2d** as deposited on Au(111). **(C)** STM topographic image of precursor **2d** following thermal annealing to 300 °C. V_s = 200 mV, I = 20 pA.

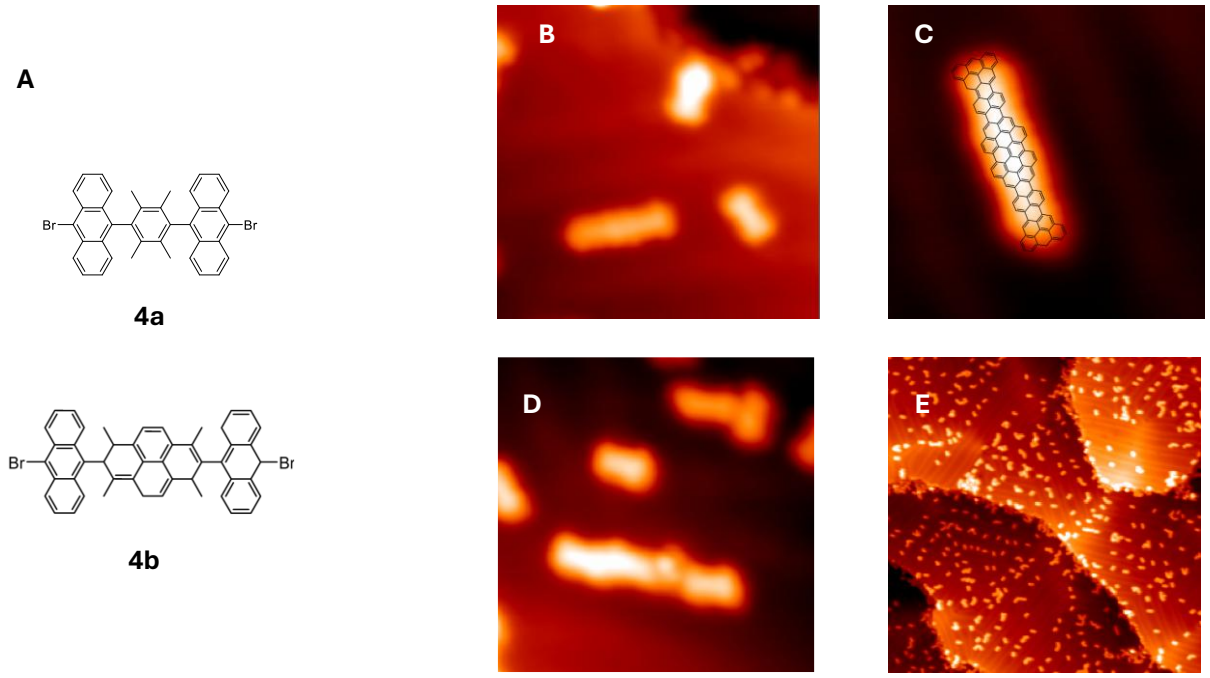

Figure S3. (A) Structures of 7/5/7-AGNR precursors **4a,b** which are designed to grow GNRs with periodic 7/5 and 5/7 heterojunctions. Attempts to grow GNRs from **4a** resulted in methyl cleavage and 5-membered ring formation, prompting design of **4b**. **(B-E)** STM topographic images of **4b** on Au(111) after thermal annealing to 300 °C. Individual monomers and some dimers which appear to have closed down on the surface are observed, along with defective structures and a very low degree of polymerization. Proposed structure of cyclodehydrogenated dimer is overlayed in **C**. V_s = 200 mV, I = 20 pA.

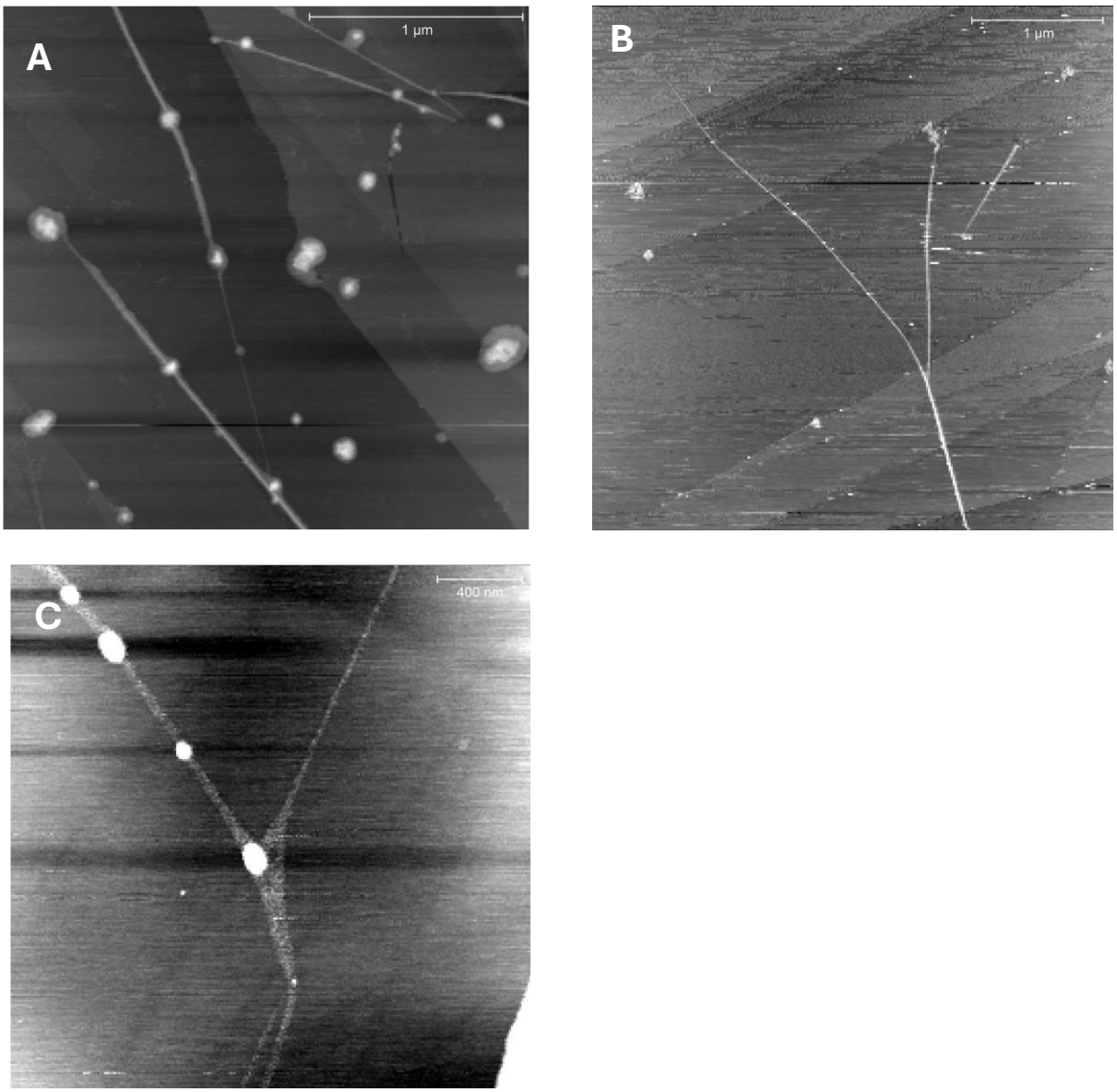

Figure S4. Ambient AFM images of PNRs from NMP dispersion on HOPG following deposition with the SAD process. Some contamination is observed but overall, the surfaces are remarkably clean. Y-junctions, a common PNR structural feature, are observed in **B,C.**

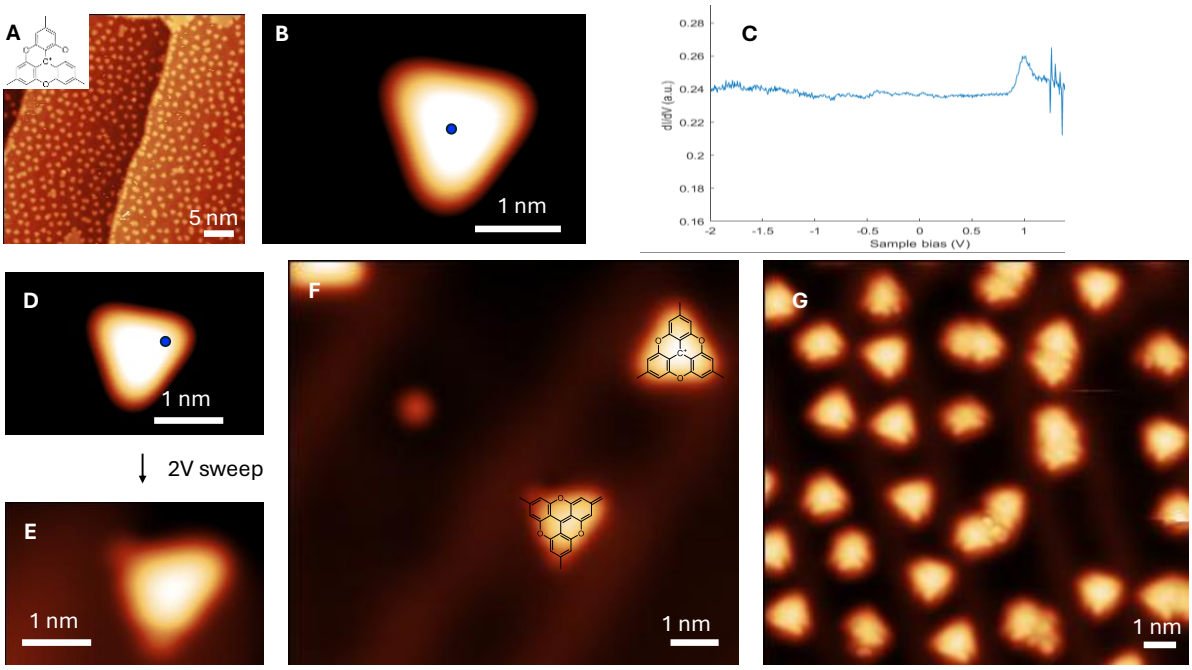

Figure S5. (A) STM topographic image of methyl-TOTA$^+$ thin films as deposited from its salt form with a BF_4^- anion. Inset shows the structure of methyl-TOTA$^+$. **(B)** Close-up STM topographic image of pristine methyl-TOTA$^+$. The blue dot marks the location where STS spectrum shown in **C** was acquired. **(C)** d*I*/d*V* spectrum collected at the center of a pristine methyl-TOTA$^+$ molecule. A peak associated with the LUMO is observed at V_s = 1.1 V. At V_s > 1.1 V a large amount of signal noise is observed. **(D)** Close-up STM topographic image of pristine methyl-TOTA$^+$ before a 2 V sweep was applied at the location marked by the blue dot. **(E)** Close-up STM topographic image of the resultant species after applying a 2V sweep at the corner of methyl-TOTA$^+$. The molecule migrated slightly on the surface and appeared to no longer have D_{3h} symmetry. A dehydrogenation mechanism is proposed where a hydrogen is removed from one of the methyl groups causing rearrangement of the electrons which neutralizes the charge. Two dim spots are observed on two of three corners which we associate with the two remaining methyl groups which point toward the surface following the rearrangement. **(F)** STM topographic image of the same species in **E** with a nearby pristine methyl-TOTA$^+$ for comparison. Structure of methyl-TOTA$^+$ and proposed dehydrogenated structure are overlayed on the image. **(G)** STM topographic image of defective methyl-TOTA$^+$ following high temperature deposition. All STM images were recorded at V_s = 500 mV, I = 20 pA, T = 4.2 K.

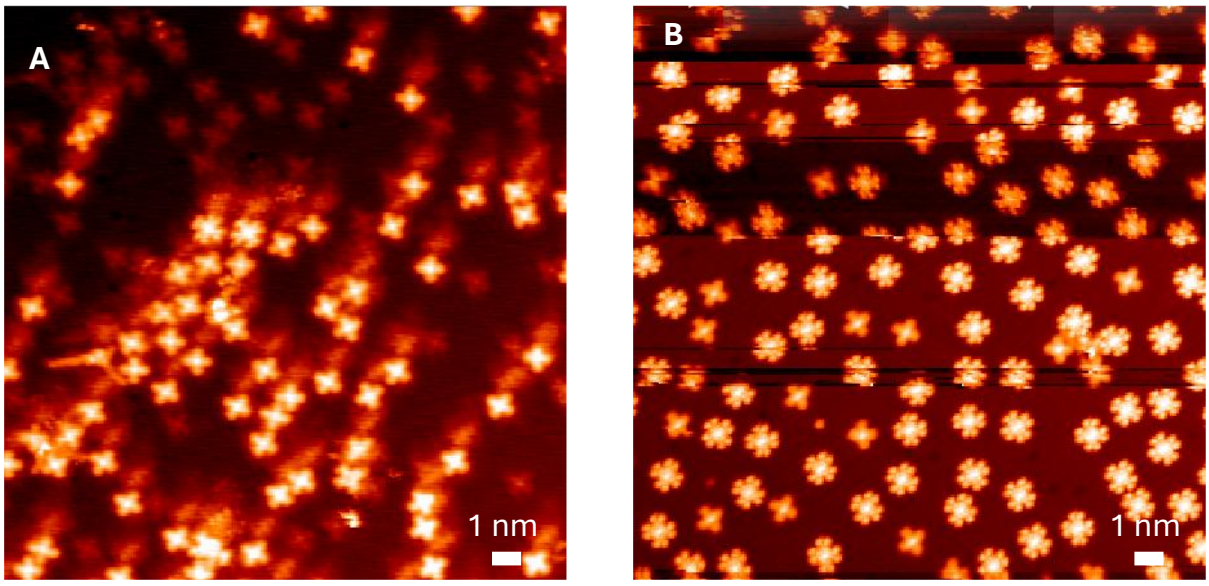

Figure S6. STM topographic images of co-deposited $CuPcF_{16}$ and $VOPcF_8$ on bulk $NbSe_2$. Both species are distinguishable in **B** and no self-assembly is observed. V_s = 500 mV, I = 20 pA, T = 4.2 K.

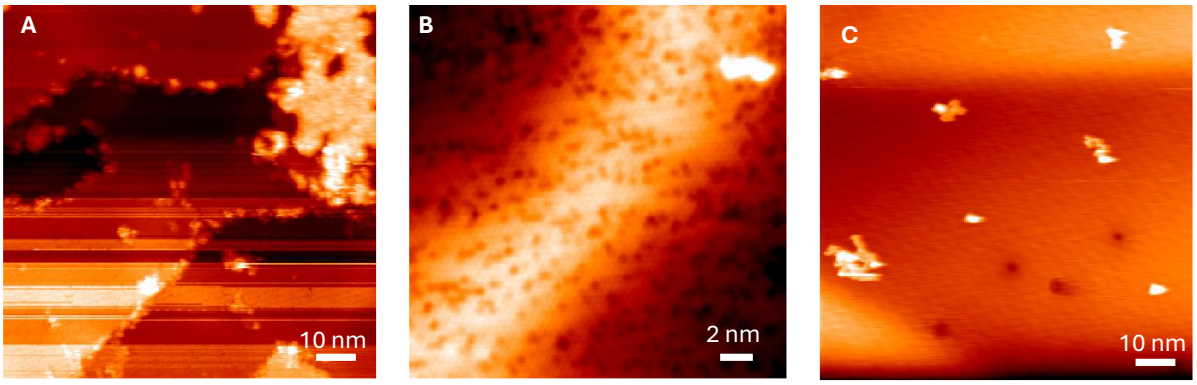

Figure S7. STM topographic images of MoS_2 transferred to Au(111) using conventional exfoliation and transfer methods (**A,B**), and the mica transfer method (**C**). V_s = 1000 mV, I = 20 pA, T = 4.2 K.

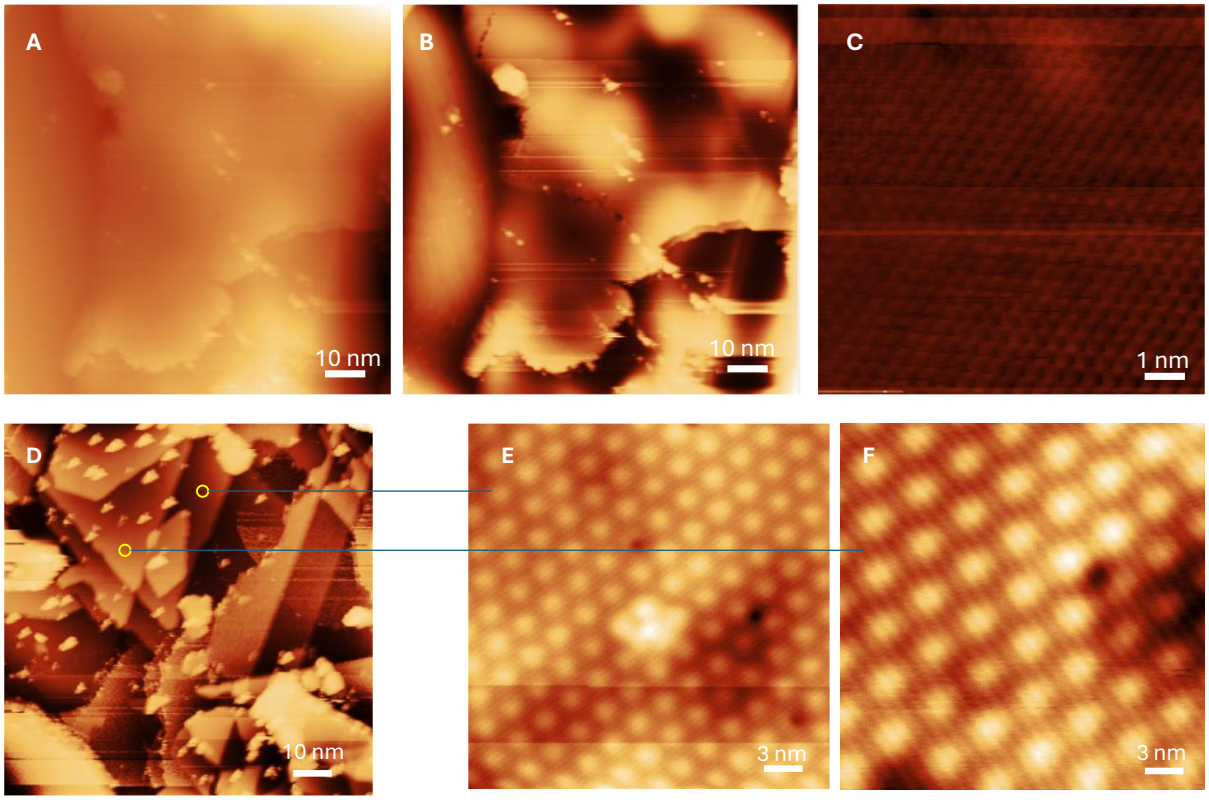

Figure S8. (A) STM topographic image of few layer $NbSe_2$ transferred on Au(111) using the in-vacuum technique, before optimizing process. **(B)** Same image as **A** shown with adaptive nonlinear color mapping to highlight the Au(111) / $NbSe_2$ boundary. **(C)** Close-up STM topographic image of few layer flake shown in **A**. **(D)** Large-scale topographic image of $NbSe_2$ on Au(111). **(E,F)** Close-up STM topographic images of areas marked in **D,** featuring distinct Moiré patterns. V_s = 500 mV, I = 20 pA, T = 4.2 K.

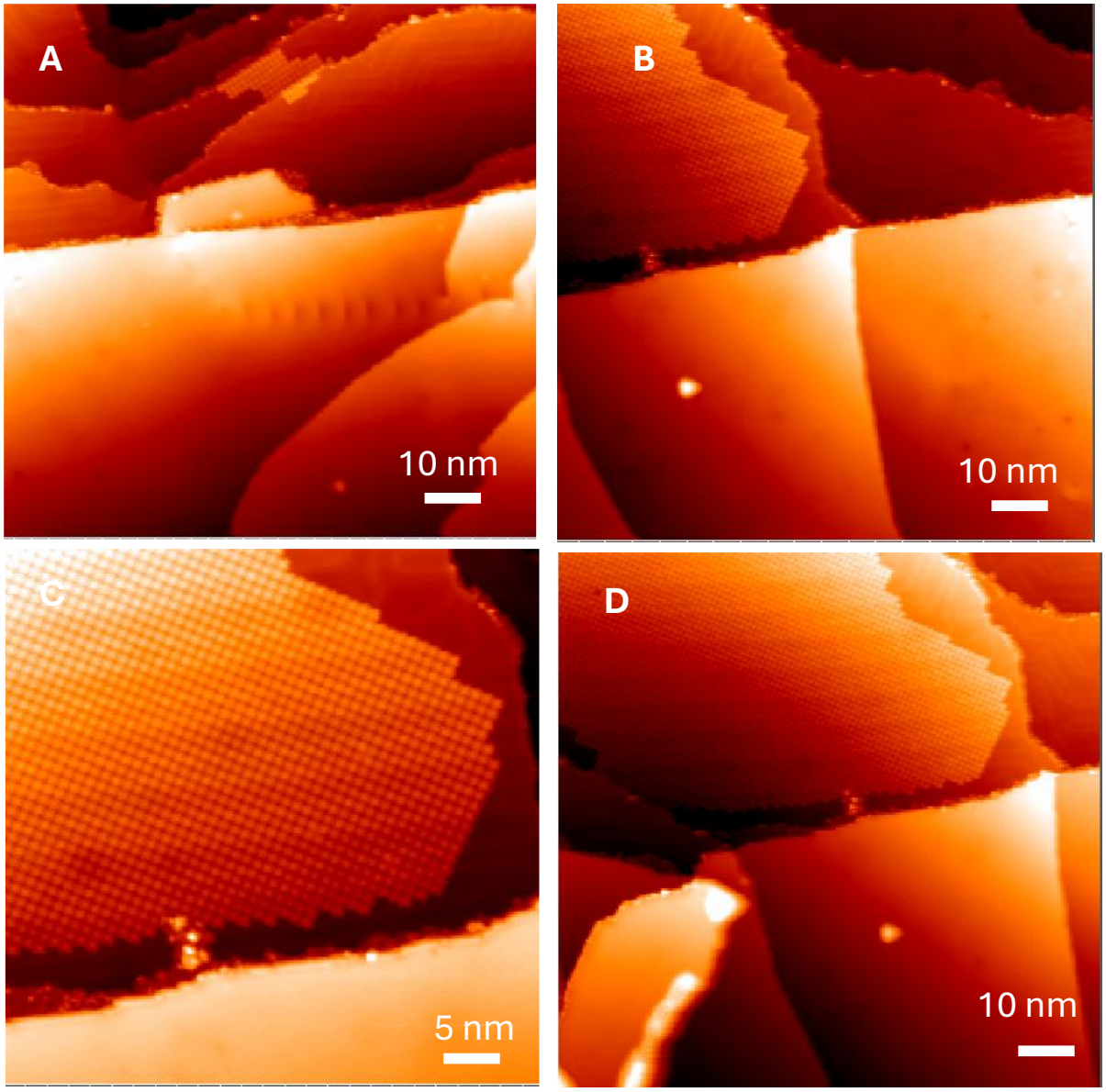

Figure S9. Topographic STM images of monolayer MoS_2 on Au(111) near molecular thin films of $CuPcF_8$. V_s = 1000 mV, I = 20 pA, T = 4.2 K.

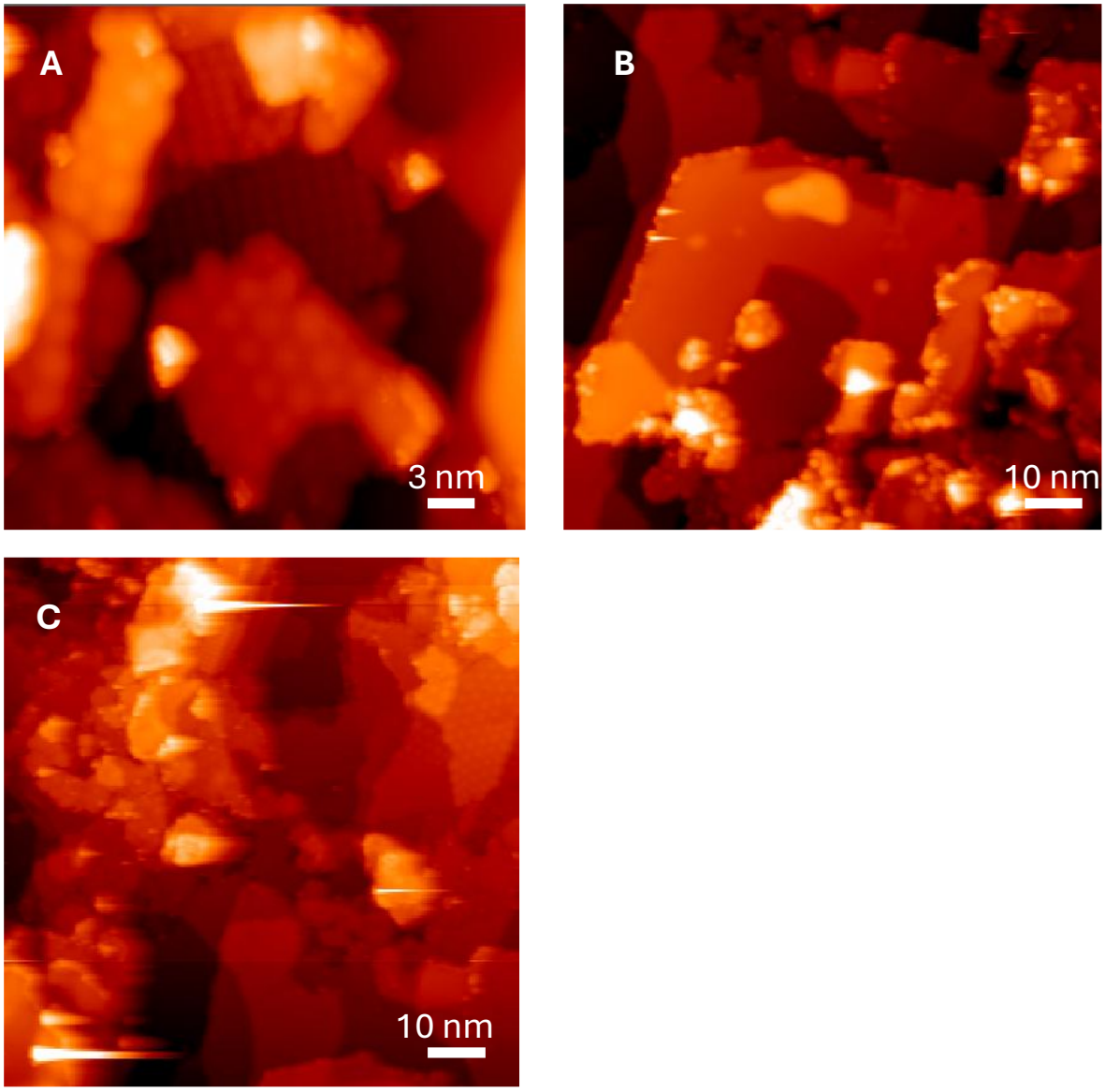

Figure S10. STM topographic images of small monolayer flakes of MoS_2 on Au(111) bordering thin films of $CuPcF_8$. V_s = 1000 mV, I = 20 pA, T = 4.2 K.

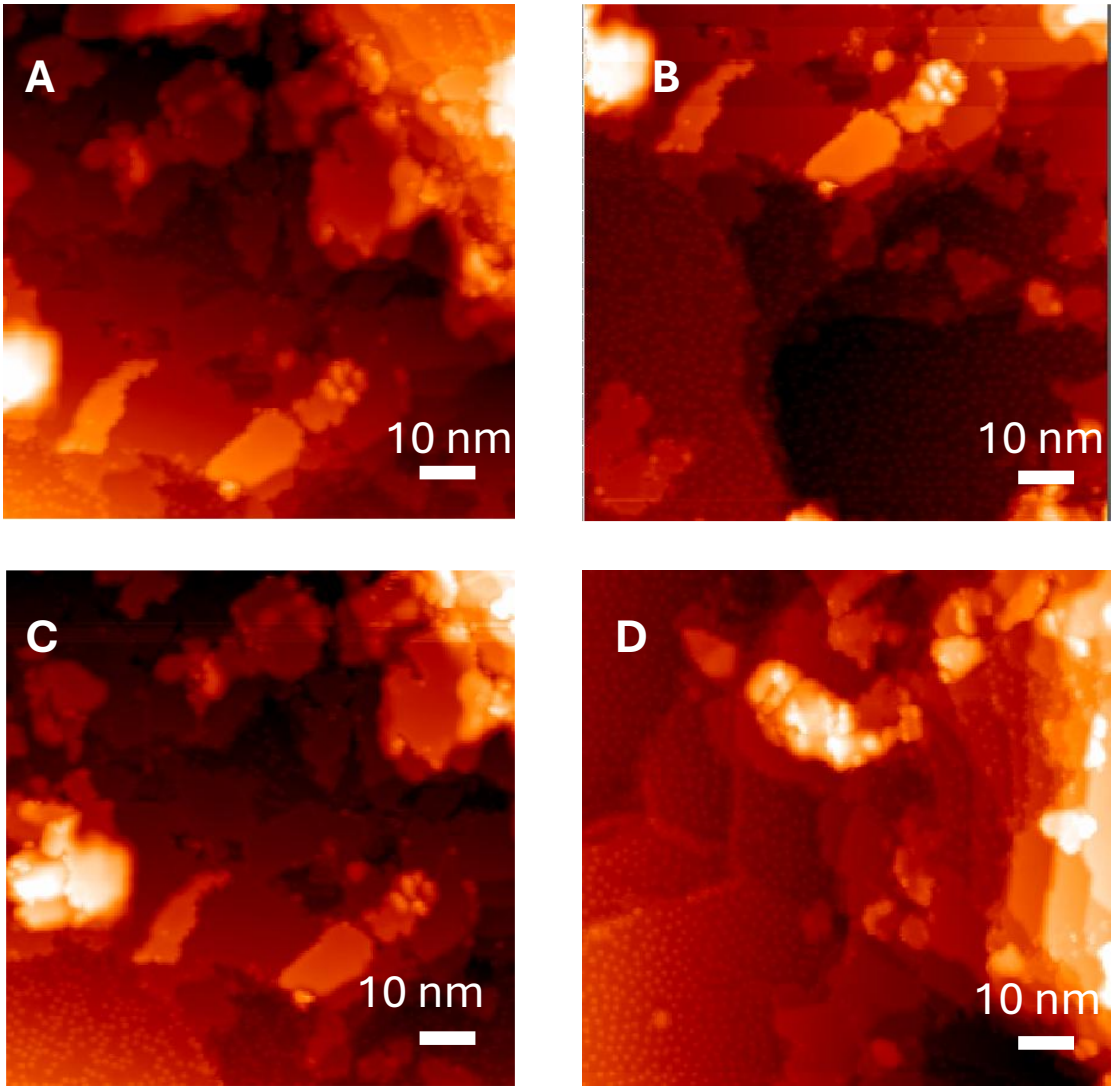

Figure S11. STM topographic images of monolayer flakes of MoS_2 on Au(111) transferred after growing molecular thin films of $TOTA^+$. V_s = 1000 mV, I = 20 pA, T = 4.2 K.